

Catalysis Science & Technology

Accepted Manuscript

This article can be cited before page numbers have been issued, to do this please use: H. Chau, S. Stofik, M. N. Gordon, M. Mueller, R. Fushimi, D. Aidhy, M. Craps, J. Lauterbach and D. D. Rodene, *Catal. Sci. Technol.*, 2026, DOI: 10.1039/D5CY01360G.



This is an Accepted Manuscript, which has been through the Royal Society of Chemistry peer review process and has been accepted for publication.

Accepted Manuscripts are published online shortly after acceptance, before technical editing, formatting and proof reading. Using this free service, authors can make their results available to the community, in citable form, before we publish the edited article. We will replace this Accepted Manuscript with the edited and formatted Advance Article as soon as it is available.

You can find more information about Accepted Manuscripts in the [Information for Authors](#).

Please note that technical editing may introduce minor changes to the text and/or graphics, which may alter content. The journal's standard [Terms & Conditions](#) and the [Ethical guidelines](#) still apply. In no event shall the Royal Society of Chemistry be held responsible for any errors or omissions in this Accepted Manuscript or any consequences arising from the use of any information it contains.

ARTICLE

Advancements in Nitrous Oxide Abatement: A Review of Direct Catalytic Decomposition and Selective Catalytic Reduction

Han Chau,^{a†} Sarah Stofik,^{b†} Matthew N. Gordon,^c Mark Mueller,^d Rebecca Fushimi,^a Dilpuneet S. Aidhy,^d Matthew Craps,^c Jochen Lauterbach,^{b*} and Dylan D. Rodene^{c*}

Received 00th January 20xx,
Accepted 00th January 20xx

DOI: 10.1039/x0xx00000x

Nitrous oxide (N₂O) emissions pose significant environmental and regulatory challenges, which necessitates a need for advancements in catalytic abatement methods. This review evaluates catalytic systems with insights for industrial applications, covering three catalyst types: supported metal catalysts (Rh/CeO₂, Ru/γ-Al₂O₃, Rh/Al₂O₃, and Pd/Al₂O₃), transition metal oxides (Co₃O₄, Mn₂O₃, CuO, and NiO), and ion-exchanged zeolites (Fe-, Co-, and Cu- on ZSM-5, BEA, SSZ-13, FER, and MOR). For direct decomposition reactions, the catalytic performance is influenced by the redox and oxygen desorption properties, as well as by the inclusion of promoters. For SCR applications, iron-based zeolites (e.g., Fe-MFI, Fe-MOR, Fe-BEA, and Fe-SSZ-13) offer high activity, low cost, and low toxicity. Among the reductants, CO and hydrocarbons demonstrate superior efficiency when compared to H₂ and NH₃ for Fe-BEA zeolites. The presence of O₂ and H₂O was shown to inhibit both reaction pathways, while SO₂ can cause irreversible deactivation. For SCR, NO demonstrates competitive adsorption, which inhibits the reaction with CO and hydrocarbon reductants. Additionally, transient kinetic studies and density functional theory were highlighted in how they inform reaction mechanisms. Furthermore, high-throughput experimentation and machine learning can be leveraged to overcome the current and future industrial shortcomings of N₂O abatement processes.

1 Introduction

Nitrous oxide (N₂O) is a detrimental pollutant that accounts for ~6.2% of the anthropogenic greenhouse gas emissions.¹ N₂O has an atmospheric lifetime of ~131 years, which leads to prolonged harmful effects on the environment (i.e., contributing to ozone depletion). Fig. 1 summarizes the natural and anthropogenic sources of N₂O. While natural sources are the primary contributors of N₂O emissions, industrial processes have led to a rapid increase in the emissions (as shown in the inset of Fig. 1).²⁻⁵ Consequently, abatement methodologies should be considered in processes that emit N₂O and treat NO_x emissions, such as adipic acid production and the industrial oxidation of ammonia (NH₃), which accounted for 76% of N₂O emissions from chemical industries in 2020 alone.^{6, 7} Emissions from industrial applications alone warrant the implementation of abatement strategies to address the continuously rising emissions.⁸⁻¹⁶

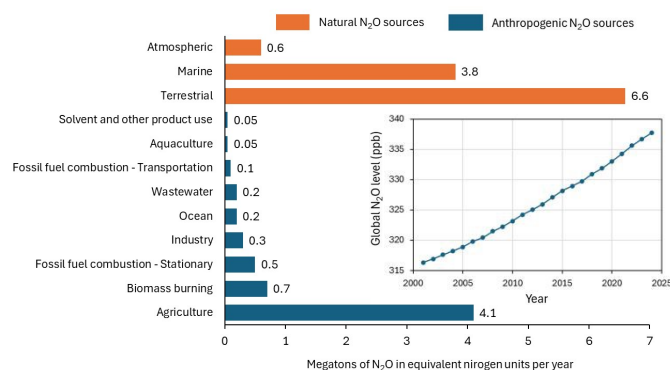


Fig. 1. Quantification of natural and anthropogenic sources of N₂O emissions by category with globally averaged atmospheric abundance over time (inset). Data from Refs. 2, 4

Among the various N₂O abatement approaches, direct catalytic decomposition and selective catalytic reduction (SCR) of N₂O have been extensively studied in the literature, are widely applied in industry, and serve as the primary focus of this review. Although several recent comprehensive reviews have analyzed N₂O abatement strategies, this review uniquely emphasizes the most commonly used catalytic systems for both direct decomposition and SCR of N₂O.⁸⁻¹³

A systematic comparison of T₅₀ values for the direct decomposition and SCR of N₂O, as reported in the literature, was performed based on the feed conditions provided. To enable further comparisons across the systems, gas hourly

^a Catalysis and Transient Kinetics Group, Idaho National Laboratory, Idaho Falls, Idaho 83415, USA.

^b Department of Chemical Engineering, University of South Carolina, Columbia, SC 29208, USA.

^c Advanced Materials & Process Technologies Group, Savannah River National Laboratory, Aiken, SC 29808, USA.

^d Department of Materials Science and Engineering, Clemson University, Clemson SC 29634, USA.

† These authors contributed equally.

* Contact information: lauteraj@cec.sc.edu and Dylan.Rodene@srnl.doe.gov



space velocity (GHSV), weight hourly space velocity (WHSV), and/or weight to volumetric flow (W/F) values were calculated (if not explicitly reported for each reference and the data was available). This standardization allows for the evaluation of catalyst performance under varying reaction conditions. Supported metals, metal oxides, and zeolites form the primary catalyst classes compared in this review, with reported or extracted T_{50} values contextualized based on their respective GHSV, WHSV, and/or W/F values reported herein. Additionally, emerging catalysts, such as single-atom catalysts and high-entropy oxides (HEOs), are discussed. This review also considers the use of both conventional and unconventional reductants, as well as the effects of impurity gases, in N_2O abatement processes. Studies on catalyst durability remain limited, regardless, oxide-based and zeolite-type catalysts stability will be discussed in sections 2.5 and 3.5.

Beyond catalyst performance evaluations, this review delves into key reaction mechanisms and considers insights gained at a molecular level from advanced tools such as Density Functional Theory (DFT) and Temporal Analysis of Products (TAP) studies. Furthermore, this review provides a forward-looking perspective on leveraging machine learning (ML) approaches and high-throughput experimentation (HTE) to accelerate catalyst discovery. These innovative methodologies have the potential to guide the development of novel catalysts, provide fundamental mechanistic insights, and enable rapid catalyst screening, to guide the field toward efficient industrial N_2O abatement.

1.1 Thermo-Catalytic Performance Definitions

For N_2O abatement, a variety of metrics exist to analyze catalytic activity and track reaction performance. Conversion efficiency is used to track the reaction progress over a range of temperatures for a catalytic system and is reported as the fraction of reactants (i.e., N_2O) that were converted to products. Gas chromatography (GC), Fourier-transform infrared spectroscopy (FTIR), and mass spectrometry (MS) are commonly used to quantify conversion efficiency for the gaseous analytes.

The T_{50} number (also known as the light-off temperature) is also commonly reported for N_2O abatement. The T_{50} number is the temperature at which conversion efficiency reaches 50% completion (i.e., the center of an S-curve conversion vs. temperature plot), where a lower T_{50} number represents a more active catalyst system.

Conversion efficiency and T_{50} alone do not account for the intrinsic properties of the catalyst and are easily impacted by temperature, metal loading, and gas flow rate.¹⁷ Therefore, the additional knowledge of the GHSV allows for a better comparison between catalysts by accounting for the volumetric flow rate of reactants to the catalyst bed with respect to the volume of the catalyst utilized. Similarly, the WHSV is also commonly reported and expresses the mass flow rate of reactants to the catalyst bed with respect to the weight of the

catalyst. The ratio of the amount of catalyst to the flow rate (W/F) is also commonly reported. The GHSV, WHSV, and W/F help to provide additional insights when comparing reported catalytic conversion efficiencies and T_{50} values of a system (e.g., larger flowrates with lower masses of catalyst will result in a larger space velocity, resulting in a lower apparent activity).

The T_{50} numbers at specified flow conditions will be the main metric reported to compare N_2O abatement catalysts. Furthermore, turnover frequency is not reported herein, due to difficulties in determining the number of active sites, as well as a lack of reporting in literature.¹⁸

1.2 Overview and Application-Based Considerations

The use of direct decomposition reaction schemes versus the SCR of N_2O presents distinct challenges and considerations. Direct decomposition enables the abatement of N_2O into N_2 and O_2 without additional reactants, whereas SCR adds additional reductants such as CO, hydrocarbons, NH_3 , or H_2 to aid in decomposition. An overview of the performance of various catalyst systems (supported metals, metal oxides, and zeolites) is shown in Fig. 2, highlighting T_{50} values for direct decomposition (Fig. 2B) and SCR of N_2O (Fig. 2C). The figure categorizes the values reported in literature based on whether H_2O and O_2 are included or omitted from the feeds of each system. The SCR values are further classified according to the four most commonly studied reductants: CO, hydrocarbons, NH_3 and H_2 . Due to the inclusion of reductants in the SCR feed, direct decomposition of N_2O generally requires higher operating temperatures (300–600 °C) compared to the SCR of N_2O (150–500 °C), as shown in T_{50} values plotted in Fig. 2.^{12, 13}

Direct N_2O decomposition offers several industrial advantages, especially when N_2O emissions originate from high-temperature processes.¹² For example, N_2O emissions are often associated with the agricultural industry, ammonia combustion, adipic acid production, or fossil fuel combustion.¹⁹ For these systems, direct decomposition may be favorable when emissions are released from high-temperature equipment, such as stoves/furnaces,^{12, 19} or following an ammonia combustion process.²⁰ Additionally, direct decomposition is often preferred in scenarios where introducing additional compounds into the system is undesirable. For instance, the addition of CO or NH_3 may elevate the risk of toxicity exposure hazards, create a stream of unreacted reactants that would require further processing, or result in the generation of additional greenhouse gas emissions.

However, SCR of N_2O may be preferable for applications that require lower operating temperatures or in industrial processes where suitable reductants are co-produced in tandem with N_2O . Moreover, some studies suggest that SCR reactions may be more applicable for treating exhaust from stationary or automotive sources.⁸



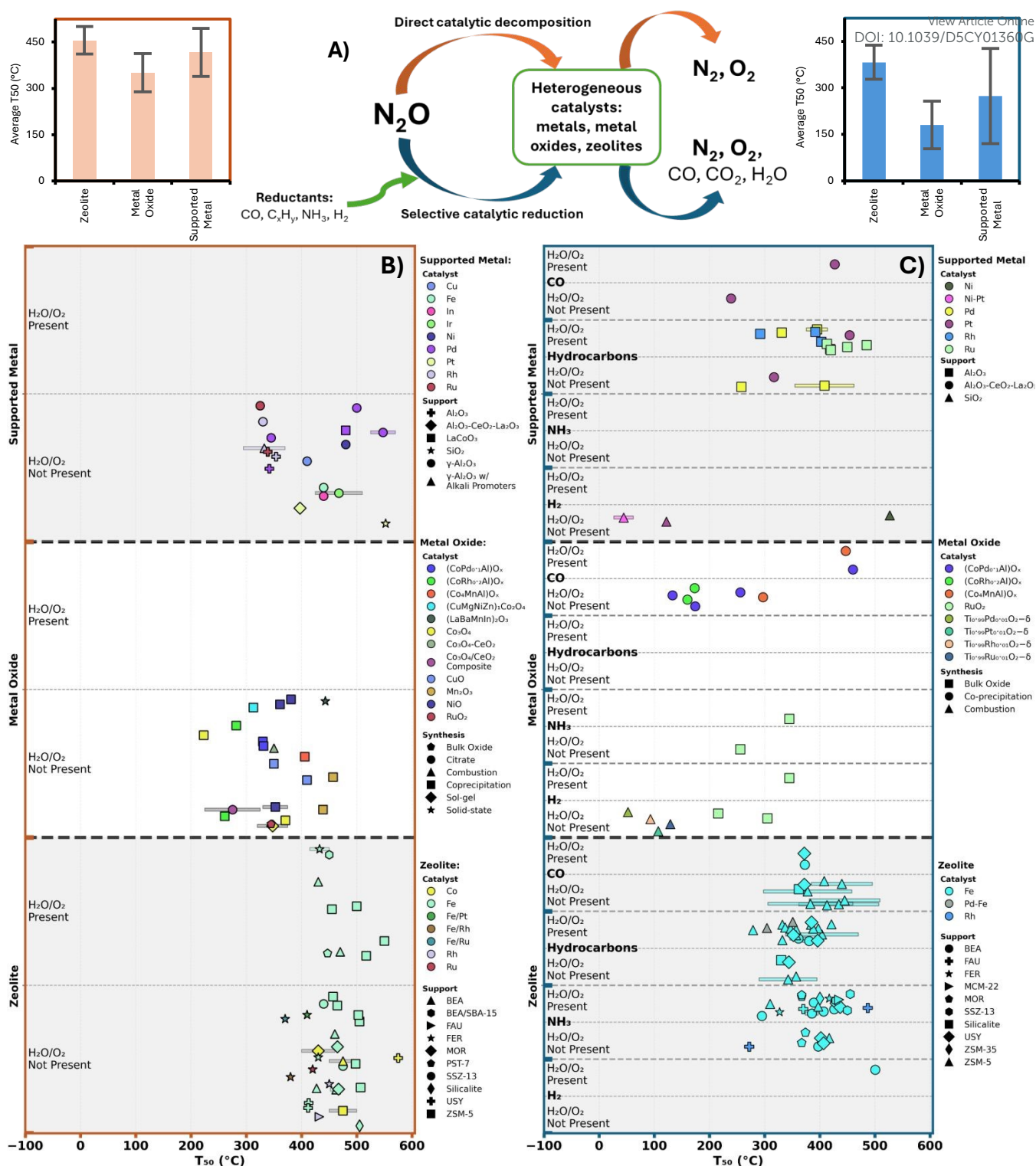


Fig. 2. (A) Reaction schemes for direct catalytic decomposition and SCR. T_{50} values for (B) direct decomposition (orange) and (C) SCR catalysts (blue). Note: three letter codes are given by the International Zeolite Association

The choice of catalyst introduces additional considerations. Noble metal catalysts are known to show high activity, with Rh/CeO₂ being considered as one of the most active catalysts for this reaction.^{21, 22} However, these catalysts are limited by

their high cost, abundance in nature, and global production constraints.²³ Cost-effective alternatives include transition metal oxides or zeolites, which have been shown to achieve low T_{50} values (as shown in Figure 2). Many of the metals used in these catalysts are more abundant than noble metals, making metal oxides and zeolite catalysts attractive.²³ Zeolites offer further advantages, such as hydrothermal stability (in some applications) as well as acidity, which may offer beneficial catalytic properties.²⁴⁻²⁶



ARTICLE

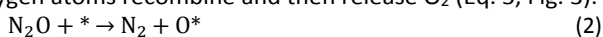
Catalysis Science & Technology

2 Direct Nitrous Oxide Decomposition

Abatement via direct decomposition of N_2O proceeds without a reducing agent to produce N_2 and O_2 (Eq. 1).



N_2O gas-phase catalytic mechanisms generally occur by having N_2O adsorb onto the catalyst active site (*) via the oxygen atom (Eq. 2). The N-O bond is then cleaved, releasing N_2 and leaving oxygen adsorbed on the surface.^{27, 28} The adsorbed oxygen removal process is slow in comparison.²⁹ Subsequently, the Eley-Rideal (E-R) or Langmuir-Hinshelwood (L-H) mechanism proceeds. For the E-R mechanism, an additional N_2O molecule interacts with the adsorbed atomic oxygen to produce O_2 and N_2 (Eqs. 3 and 4, Fig. 3). For the L-H mechanism, two adsorbed oxygen atoms recombine and then release O_2 (Eq. 5, Fig. 3).



The Mars-van Krevelen mechanism is commonly suggested for many redox reactions, but it is not often observed in the direct decomposition of N_2O . By employing in situ XPS and DFT methods, Sun et al. demonstrated that the direct N_2O decomposition over single-atom Ru on CeO_2 nanorods proceeds via the Mars-van Krevelen mechanism.³⁰ Notably, oxygen desorption and oxygen vacancy formation are facilitated by the recombination of oxygen atoms that dissociate from N_2O with adjacent lattice oxygen. The Mars-van Krevelen mechanism is discussed more in Section 3 and depicted in Figure 7B, where an oxygen vacancy is created by a reductant to facilitate the N_2O reaction.

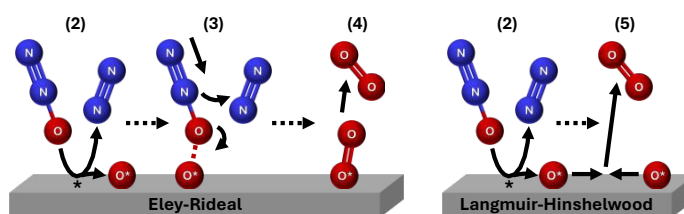


Fig. 3. Schematics of the Eley-Rideal and Langmuir-Hinshelwood mechanisms for N_2O decomposition. ("*" denotes surface site or adsorbed species). The numbers refer to the equations found in the text.

Regardless of the mechanism, the O_2 desorption step is crucial to the catalyst performance for N_2O decomposition due to the inhibitory effects of O_2 . Multiple studies report decreased conversion and reaction rates with excess O_2 present across various catalysts.³¹⁻³³ O_2 often competes for binding sites and is slow to desorb from the catalyst. Therefore, catalyst discovery is necessary to aid in the desorption of oxygen from the surface of the catalyst to obtain increased conversion.

Several different catalyst designs have been utilized and modified in attempts to decompose N_2O and are considered by the following main categories: supported metal, metal oxide, and zeolite catalysts. These three types of catalysts will be

discussed for N_2O decomposition, and a summary of the catalysts with corresponding activities is shown in Table 1 and Fig. 2B.

2.1 Supported Metal Catalysts

Many studies have suggested that Rh/CeO_2 is one of the more active catalysts for the direct decomposition of N_2O .²¹ In one comprehensive study conducted by Li et al., the researchers found that the synthesis of these Rh/CeO_2 catalysts were important to increased activity.²¹ The authors found that the calcination temperature of the supported Rh/CeO_2 catalysts led to an increase in activity (by a decrease in T_{50} value from ~ 355 °C for catalysts calcined at 500 °C to ~ 325 °C for catalysts calcined at 800 °C). They found further enhancement of catalytic activity by first calcining the support (CeO_2) at 800 °C where the T_{50} value was further reduced to ~ 310 °C.²¹ Furthermore, Zhang et al. found that steam treating the catalyst allowed for a more water tolerant Rh/CeO_2 catalyst.²² Though it is generally accepted that Rh is the most active metal for the abatement of N_2O , previous studies have looked at the activity of the different platinum group metals (i.e., Rh, Pt, Pd, Ru, and Ir) and compared them to the activity of transition metals, which may provide cheaper alternatives. Pekridis et al. analyzed the impact of utilizing Pd, Rh, Ru, Cu, Fe, In, and Ni at 2 wt% supported on $\gamma\text{-Al}_2\text{O}_3$ (Fig. 4A).³² It was found that the three noble metals (Pd, Ru, and Rh) exhibited the highest activity with the lowest T_{50} of ~ 325 °C. Of the transition metals, Cu exhibited the highest activity with a T_{50} of ~ 400 °C. Though the Cu-supported catalyst outperformed the other transition metal-supported catalysts, the noble metal catalysts still showed superior activity.³² The authors attributed the difference in activity to the strength of oxygen adsorption on the surface. When testing noble metal catalysts in a reactant feed with excess O_2 , all T_{50} values shifted towards higher temperatures; however, the increase in T_{50} for the noble metals was about 25 °C compared to the shift of 50 °C for the transition metals, which is likely a result of the higher electron density of the noble metals to efficiently facilitate oxygen desorption.³²

Pachatouridou et al. investigated the impact of the weight loading of noble metals on the decomposition of N_2O . The effect of Pt, Pd, and Ir supported on $\gamma\text{-Al}_2\text{O}_3$ at various weight loadings showed that an increased metal loading led to increased N_2O conversion at lower temperatures, thus resulting in lower T_{50} numbers.³³ The Ir metal catalyst was found to have the highest activity in the absence of O_2 . The addition of oxygen raised the T_{50} by ~ 100 °C, for the most active catalyst with 1 wt% Ir. The difference in activity was attributed to the ability of each metal to adsorb oxygen. In catalytic tests in both the presence and absence of O_2 , $\text{Pt}/\text{Al}_2\text{O}_3$ was less active, while Ir- and Pd-based catalysts were less affected. The authors attributed the overall poor Pt performance to site blocking or competitive adsorption of O_2 to the active, metallic Pt surface, and the better Ir and Pd performances to oxide phases that are less susceptible to oxygen poisoning. When comparing the crystallite size from XRD and TEM, larger crystallites of IrO_2 (26.2 nm) were



Table 1: Summary of N₂O direct decomposition catalysts, grouped by catalyst type: supported metal catalysts (top), metal oxide catalysts (middle), and zeolite catalysts (bottom). T₅₀ represents the temperature at which 50% conversion is reached, with flow conditions being defined by the gas hourly space velocity (GHSV), weight hourly space velocity (WHSV), or ratio of catalyst weight to volumetric gas flow rate (W/F). Note: GHSV, WHSV, and W/F were standardized based on feed conditions presented in the literature source for further comparison.

| Metal | Support | Catalyst Synthesis | Reaction Pretreatment | Feed Composition | GHSV (h ⁻¹) | WHSV (h ⁻¹) | W/F (g·s·mL ⁻¹) | T ₅₀ (°C) | Ref. |
|-----------------|--|--|---|--|-------------------------|-------------------------|-----------------------------|----------------------|------|
| Rh (1 wt%) | CeO ₂ | Dry Impregnation followed by steam treatment | | 0.3% N ₂ O/He | | | 0.018 | ~273 | 22 |
| Rh (1 wt%) | CeO ₂ | Dry Impregnation | | 200 ppm N ₂ O/ 5% CO ₂ /N ₂ | 30,000 | | | ~310 | 21 |
| Ru (2 wt%) | γ-Al ₂ O ₃ | Dry Impregnation | He: 600 °C/1 h | 0.12% N ₂ O/He | 35,000 | | | ~325 | 32 |
| Rh (2 wt%) | γ-Al ₂ O ₃ | Dry Impregnation | He: 600 °C/1 h | 0.12% N ₂ O/He | 35,000 | | | ~330 | 32 |
| Pd (2 wt%) | γ-Al ₂ O ₃ | Dry Impregnation | He: 600 °C/1 h | 0.12% N ₂ O/He | 35,000 | | | ~345 | 32 |
| Cu (2 wt%) | γ-Al ₂ O ₃ | Dry Impregnation | He: 600 °C/1 h | 0.12% N ₂ O/He | 35,000 | | | ~410 | 32 |
| Fe (2 wt%) | γ-Al ₂ O ₃ | Dry Impregnation | He: 600 °C/1 h | 0.12% N ₂ O/He | 35,000 | | | ~440 | 32 |
| In (2 wt%) | γ-Al ₂ O ₃ | Dry Impregnation | He: 600 °C/1 h | 0.12% N ₂ O/He | 35,000 | | | ~440 | 32 |
| Ni (2 wt%) | γ-Al ₂ O ₃ | Dry Impregnation | He: 600 °C/1 h | 0.12% N ₂ O/He | 35,000 | | | ~480 | 32 |
| Pt (0.25-1 wt%) | γ-Al ₂ O ₃ | Dry Impregnation | He: 600 °C/1 h | 0.1% N ₂ O/He | 40,000 | | | | 33 |
| Ir (0.25-1 wt%) | γ-Al ₂ O ₃ | Dry Impregnation | He: 600 °C/1 h | 0.1% N ₂ O/He | 40,000 | | | 425-510 | 33 |
| Pd (0.25-1 wt%) | γ-Al ₂ O ₃ | Dry Impregnation | He: 600 °C/1 h | 0.1% N ₂ O/He | 40,000 | | | 525-570 | 33 |
| Rh (0.5 wt%) | CeO ₂ | Dry Impregnation | | 1,000 ppm N ₂ O/He | 10,000 | | | | 27 |
| Rh (0.5 wt%) | γ-Al ₂ O ₃ | Dry Impregnation | | 1,000 ppm N ₂ O/He | 10,000 | | | | 27 |
| Pd (1 wt%) | LaCoO ₃ | Impregnation | | 1,000 ppm N ₂ O/1,000 ppm NO/He | | | 0.168 | ~480 | 34 |
| Pd (1 wt%) | γ-Al ₂ O ₃ | Impregnation | | 1,000 ppm N ₂ O/1,000 ppm NO/He | | | 0.168 | ~500 | 34 |
| Rh (1 wt%) | γ-Al ₂ O ₃ | Dry Impregnation | | 200 ppm N ₂ O/5% O ₂ /N ₂ | 30,000 | | | | 35 |
| Rh (1 wt%) | CeO ₂ | Dry Impregnation | | 200 ppm N ₂ O/5% O ₂ /N ₂ | 30,000 | | | | 35 |
| Rh (0.1 wt%) | γ-Al ₂ O ₃ with alkali promoters | Impregnation | | 1% N ₂ O/N ₂ | 4,000 | | | 295-370 | 36 |
| Rh (2 wt%) | ZrO ₂ with Pd as a promoter | Impregnation | | 1,000 ppm N ₂ O/He | | | 0.02 | 307 | 37 |
| Pt (0.5 wt%) | Al ₂ O ₃ -CeO ₂ -La ₂ O ₃ | Co-precipitation, impregnation | H ₂ /He, 400 °C, 1 h He, 400 °C, 1h | 0.1% N ₂ O, He balance | 10,000 | | | 397 | 38 |

ARTICLE

Catalysis Science & Technology

| Ru (2 wt%) | Al ₂ O ₃ | Dry impregnation | | 500 ppm N ₂ O, He balance | | | 0.12 | 339 | 39 |
|---|--------------------------------------|--|---|---|----------------------------|----------------------------|--------------------------------|-------------------------|------|
| Rh (2 wt%) | Al ₂ O ₃ | Dry impregnation | | 500 ppm N ₂ O, He balance | | | 0.12 | 354 | 39 |
| Pd (2 wt%) | Al ₂ O ₃ | Dry impregnation | He, 100 cm ³ /min, 600 °C, 1 h | 0.12% N ₂ O, He balance | 35,000 | | | 342 | 40 |
| Pt (2 wt%) | SiO ₂ | Incipient wetness impregnation | H ₂ , 400 °C, 1 h | 1,250 ppm N ₂ O, He balance | 25,000 | | | 552 | 41 |
| Oxide | Dopant/ Promoter | Catalyst Synthesis | Reaction Pretreatment | Feed Composition | GHSV (h ⁻¹) | WHSV (h ⁻¹) | W/F (g·s·mL ⁻¹) | T ₅₀ (°C) | Ref. |
| MnO | | | He: 120 °C/45 min then 500 °C/90 min | 0.066 atm N ₂ O/N ₂ | 2,000 | | | | 42 |
| Mn ₃ O ₄ | | | He: 120 °C/45 min then 500 °C/90 min | 0.066 atm N ₂ O/N ₂ | 2,000 | | | | 42 |
| Mn ₂ O ₃ | | | He: 120 °C/45 min then 500 °C/90 min | 0.066 atm N ₂ O/N ₂ | 2,000 | | | | 42 |
| MnO ₂ | | | He: 120 °C/45 min then 500 °C/90 min | 0.066 atm N ₂ O/N ₂ | 2,000 | | | | 42 |
| Co ₃ O ₄ | | | | 5% N ₂ O/Ar | 80,000 | | | <700 | 31 |
| CuO | CeO ₂ (nanorods) | CeO ₂ : hydrothermal CuO/CeO ₂ : precipitation | Ar: 400 °C/1 h | 2,500 ppm N ₂ O/Ar | | | | | 43 |
| Co ₃ O ₄ /CeO ₂ Composite Oxide | Li, Na, K, Rb, Cs, Mg, Ca, Sr, Ba | Citrate method | 20% O ₂ /Ar: 400 °C/30 min | 1,000 ppm N ₂ O/Ar | | | 0.2 | 225-325 | 44 |
| Co ₃ O ₄ | Cs | Coprecipitation | | 1,000 ppm N ₂ O/N ₂ | 30,000 | | | 223 | 45 |
| CuO | Cs | Coprecipitation | | 1,000 ppm N ₂ O/N ₂ | 30,000 | | | 350 | 45 |
| NiO | | Coprecipitation | | 1,000 ppm N ₂ O/N ₂ | 30,000 | | | 361 | 45 |
| Co ₃ O ₄ | | Coprecipitation | | 1,000 ppm N ₂ O/N ₂ | 30,000 | | | 371 | 45 |
| NiO | Cs | Coprecipitation | | 1,000 ppm N ₂ O/N ₂ | 30,000 | | | 381 | 45 |
| CuO | | Coprecipitation | | 1,000 ppm N ₂ O/N ₂ | 30,000 | | | 410 | 45 |
| Mn ₂ O ₃ | | Coprecipitation | | 1,000 ppm N ₂ O/N ₂ | 30,000 | | | 439 | 45 |
| Mn ₂ O ₃ | Cs | Coprecipitation | | 1,000 ppm N ₂ O/N ₂ | 30,000 | | | 457 | 45 |
| Co ₃ O ₄ -CeO ₂ | Rb | Combustion method employing urea | N ₂ : 500 °C/1 h | 500 ppm N ₂ O/N ₂ | | | 0.15 | ~350 | 46 |
| Co ₃ O ₄ | Sm | Sol-gel method with citric acid and urea | | 1,000 ppm N ₂ O/N ₂ | | | 0.06 | ~320-375 | 47 |
| NiO | Pr | Coprecipitation | | 800 ppm N ₂ O/N ₂ | | | 0.06 | ~330-375 | 48 |
| Co ₃ O ₄ | Ce-Pr | Coprecipitation | | 800 ppm N ₂ O/N ₂ | 60,000 | | | 317 | 49 |
| Co ₃ O ₄ | K-Dy | Sol-gel | Ar: 400 °C/30 min | 2000 ppmv N ₂ O/Ar | 20,000 | | | ~225-240 | 50 |
| Co ₃ O ₄ | K-Dy | Co-precipitation and Impregnation | Ar: 500 °C/30 min | 2000 ppmv N ₂ O/Ar | 20,000 | | | ~225 | 51 |



Journal Name

Catalysis Science & Technology

| | | | | | | | | | |
|--|-----------------------------------|---|--------------------------------|---|------------------------------|------------------------------|----------------------------------|----------------------------|-------------|
| Co ₃ O ₄ | Bi | Sol-gel | Ar: 400 °C/30 min | 2000 ppmv/Ar | | | 0.24 | ~250 | 52 |
| Co ₃ O ₄ | F | Co-precipitation | | 1000 ppm/Ar | 10,000 | | | 310 | 53 |
| Co ₃ O ₄ | N | g-C ₃ N ₄ -modified thermal decomposition | | 1000 ppmv N ₂ O/Ar | 10,000 | | | ~260 | 54 |
| Co ₃ O ₄ | NiO-Y ₂ O ₃ | Co-precipitation | | 1000 ppmv N ₂ O/Ar | 10,000 | | | ~275 | 55 |
| RuO ₂ | | Bulk oxide | He, 400 °C, 1 h | N ₂ O (1.5 mbar), He balance | | 5.4 | | 345 | 56 |
| (CuMgNiZn) ₁ Co ₂ O ₄ | | Coprecipitation | | 1,000 ppm N ₂ O/N ₂ | 60,000 | | | 313 | 57 |
| La _{0.7} Ba _{0.3} Mn _{0.8} In _{0.2} O ₃ | | Solid-state | | 10% N ₂ O/He | | | 3.0 | ~443 | 58 |
| (CoRh _{0.2} Al) _x Mixed Oxide | | Co-precipitation of hydrotalcite-type precursors | N ₂ , 500 °C, > 3 h | 12,500 ppm N ₂ O, N ₂ balance | 30,000 | | | 261 | 59 |
| (CoPd _{0.1} Al) _x Mixed Oxide | | Co-precipitation of hydrotalcite-type precursors | N ₂ , 500 °C, > 3 h | 12,500 ppm N ₂ O, N ₂ balance | 30,000 | | | 330 | 59 |
| (Co ₄ MnAl) _x Mixed Oxide | | Co-precipitation of hydrotalcite-type precursors | He, 450 °C, 1 h | 0.1 mol% N ₂ O, He balance | | | 0.06 | 406 | 60 |
| (CoRh _{0.2} Al) _x Mixed Oxide | | Co-precipitation of hydrotalcite-type precursors | | 12,500 ppm N ₂ O, N ₂ balance | 30,000 | | | 274 – 290 | 61 |
| (CoPd _{0.1} Al) _x Mixed Oxide | | Co-precipitation of hydrotalcite-type precursors | | 12,500 ppm N ₂ O, N ₂ balance | 30,000 | | | 328 – 334 | 61 |
| Metal | Zeolite Base | Catalyst Synthesis | Reaction Pretreatment | Feed Composition | GHSV (h⁻¹) | WHSV (h⁻¹) | W/F (g·s·mL⁻¹) | T₅₀ (°C) | Ref. |
| Cu | SSZ-13 | Ion Exchange | Air: 500 °C/30 min | 500 ppm N ₂ O/N ₂ | | | 0.0031 | | 28 |
| Co | SSZ-13 | Ion Exchange | Air: 500 °C/30 min | 500 ppm N ₂ O/N ₂ | | | 0.0031 | | 28 |
| Fe | SSZ-13 | Ion Exchange | Air: 500 °C/30 min | 500 ppm N ₂ O/N ₂ | | | 0.0081 | | 28 |
| Co | MOR | Wet Ion Exchange | He: 600 °C/1h | 5,000 ppm N ₂ O/He | 30,000 | | | ~400-460 | 62 |
| Co | ZSM-5 | Wet Ion Exchange | He: 600 °C/1h | 5,000 ppm N ₂ O/He | 30,000 | | | ~450-500 | 62 |
| Co | BEA | Wet Ion Exchange | He: 600 °C/1h | 5,000 ppm N ₂ O/He | 30,000 | | | ~450-500 | 62 |
| Co | USY | Wet Ion Exchange | He: 600 °C/1h | 5,000 ppm N ₂ O/He | 30,000 | | | ~575 | 62 |
| Fe/Ru | FER | Ion Exchange | | 1,000 ppm N ₂ O/He | 90,000 | | | ~360 | 63 |

ARTICLE

Catalysis Science & Technology

| | | | | | | | | | |
|-------|------------|--|--|--|---------|------|------|-----------|----|
| Fe/Rh | FER | Ion Exchange | | 1,000 ppm N ₂ O/He | 90,000 | | | ~380 | 63 |
| Fe/Pt | FER | Ion Exchange | | 1,000 ppm N ₂ O/He | 90,000 | | | ~410 | 63 |
| Ru | FER | Ion Exchange | | 1,000 ppm N ₂ O/He | 90,000 | | | ~420 | 63 |
| Fe | FER | Ion Exchange | | 1,000 ppm N ₂ O/He | 90,000 | | | ~430 | 63 |
| Rh | FER | Ion Exchange | | 1,000 ppm N ₂ O/He | 90,000 | | | >450 | 63 |
| Fe | FER | Ion Exchange | Air: 550 °C/2 h | 0.2% N ₂ O/3.0% O ₂ /He | 35,000 | | | ~417-437 | 64 |
| Fe | BEA | Ion Exchange | Air: 550 °C/2 h | 0.2% N ₂ O/3.0% O ₂ /He | 35,000 | | | ~467-477 | 64 |
| Fe | ZSM-5 | Ion Exchange | Air: 550 °C/2 h | 0.2% N ₂ O/3.0% O ₂ /He | 35,000 | | | ~497-507 | 64 |
| Fe | SSZ-13 | Ion Exchange | 14% O ₂ /N ₂ : 500 °C/1 h | 540 ppm N ₂ O/N ₂ | 200,000 | | | ~440 | 24 |
| Fe | BEA | Ion Exchange | 14% O ₂ /N ₂ : 500 °C/1 h | 540 ppm N ₂ O/N ₂ | 200,000 | | | ~460 | 24 |
| Fe | PST-7 | Hydrothermal | Air: 550 °C/2 h | 1,000 ppm N ₂ O/4% O ₂ /He | 42,000 | | | 447 | 65 |
| Fe | ZSM-5 | Hydrothermal | Air: 550 °C/2 h | 1,000 ppm N ₂ O/4% O ₂ /He | 42,000 | | | 517 | 65 |
| Fe | SBA-15 | Ion Exchange | He: 550 °C/1 h | 5,000 ppm N ₂ O/45,000 ppm O ₂ /He | | | 0.12 | | 26 |
| Fe | BEA | Ion Exchange | He: 550 °C/1 h | 5,000 ppm N ₂ O/45,000 ppm O ₂ /He | | | 0.12 | ~430 | 26 |
| Fe | BEA/SBA-15 | Ion Exchange | He: 550 °C/1 h | 5,000 ppm N ₂ O/45,000 ppm O ₂ /He | | | 0.12 | ~450 °C | 26 |
| Fe | ZSM-5 | Wet Ion Exchange + Alkaline Treatment of Zeolite | Ar: 500 °C/30 min | 5,000 ppm N ₂ O/5% O ₂ /Ar | 30,000 | | | ~455 | 66 |
| Fe | ZSM-5 | Wet Ion Exchange | Ar: 500 °C/30 min | 5,000 ppm N ₂ O/5% O ₂ /Ar | 30,000 | | | ~550 | 66 |
| Fe | BEA | Ion exchange | 3% H ₂ /Ar, 13 cm ³ /min, ramp from 80 – 700 °C at 10 °C/min | 0.2% N ₂ O, He balance | 35,000 | | | 452 – 473 | 67 |
| Fe | Silicalite | Hydrothermal, ion exchange, steam activation | N ₂ O/He, 450 °C, 1 h | N ₂ O (1.5 mbar), He balance | | 11.3 | | 505 | 68 |
| Fe | ZSM-5 | Hydrothermal, ion exchange, steam activation | N ₂ O/He, 450 °C, 1 h | N ₂ O (1.5 mbar), He balance | | 11.3 | | 505 | 68 |
| Fe | ZSM-5 | Sublimation | N ₂ O/He, 450 °C, 1 h | N ₂ O (1.5 mbar), He balance | | 10.8 | | 465 | 69 |
| Fe | ZSM-5 | Isomorphous substitution, steam activation | N ₂ O/He, 450 °C, 1 h | N ₂ O (1.5 mbar), He balance | | 10.8 | | 498 | 69 |
| Fe | ZSM-5 | Hydrothermal, ion exchange, steam activation | He, 450 °C, 2 h | N ₂ O (1.5 mbar), He balance | 90,000 | | | 507 | 70 |
| Fe | ZSM-5 | Isomorphous substitution, ion | He, 450 °C, 2 h | N ₂ O (1.5 mbar), He balance | 90,000 | | | 503 | 71 |



Journal Name

Catalysis Science & Technology

| | | | | | | | | | |
|----|-------|----------------------------|-----------------|--|--------|--|--|-----|---------------|
| | | exchange, steam activation | | | | | | | |
| Fe | USY | Ion exchange | He, 600 °C, 1 h | 5,000 ppm N ₂ O, He balance | 30,000 | | | 413 | ⁷² |
| Fe | USY | Ion exchange | He, 600 °C, 1 h | 5,000 ppm N ₂ O, He balance | 30,000 | | | 412 | ⁷³ |
| Fe | BEA | Ion exchange | He, 600 °C, 1 h | 5,000 ppm N ₂ O, He balance | 30,000 | | | 427 | ⁷³ |
| Fe | MOR | Ion exchange | He, 600 °C, 1 h | 5,000 ppm N ₂ O, He balance | 30,000 | | | 465 | ⁷³ |
| Fe | ZSM-5 | Ion exchange | He, 600 °C, 1 h | 5,000 ppm N ₂ O, He balance | 30,000 | | | 457 | ⁷³ |
| Fe | MOR | Ion exchange | He, 600 °C, 1 h | 5,000 ppm N ₂ O, He balance | 30,000 | | | 467 | ⁷⁴ |
| Rh | FAU | Impregnation | Air, 500 °C | 0.2% N ₂ O, He balance | 30,000 | | | 432 | ⁷⁵ |



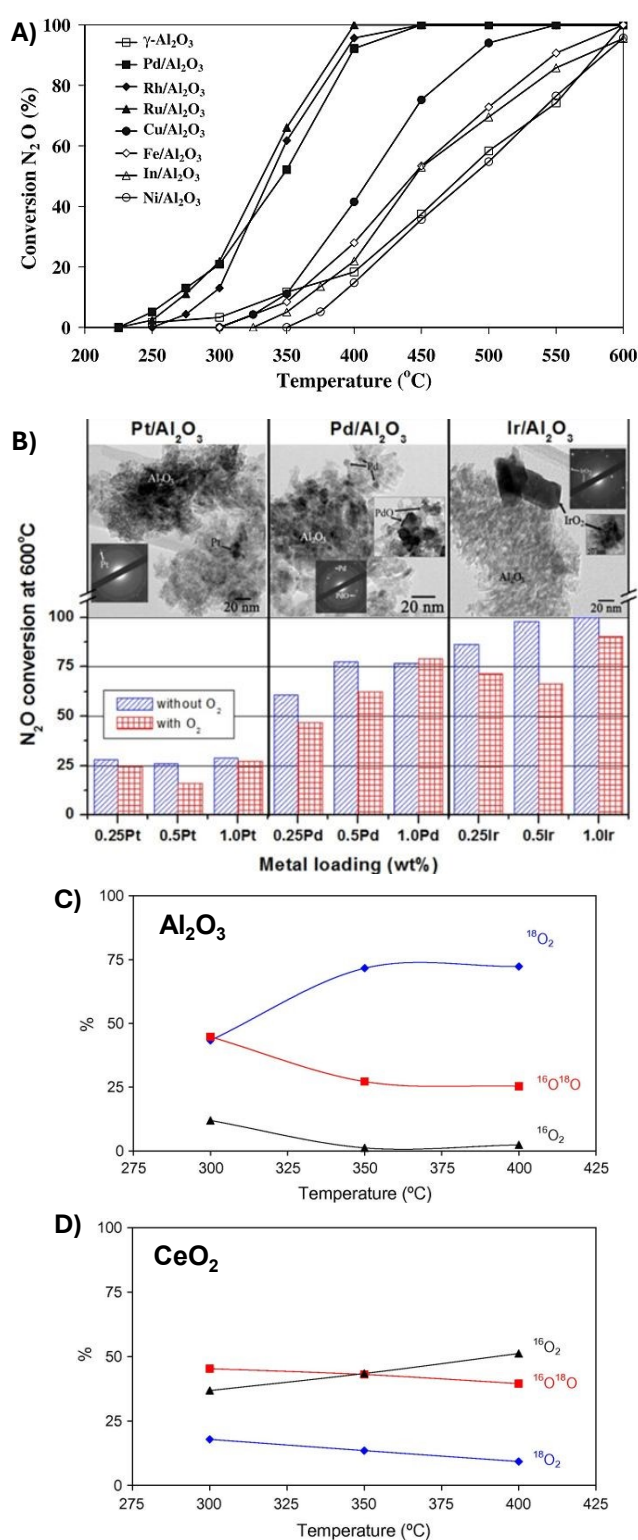


Fig. 4. (A) Comparison of catalytic activity for various Al_2O_3 -supported metal catalysts (2 wt% metal tested at a GHSV = 35,000 h^{-1} with $P_{\text{N}_2\text{O}} = 0.12\%$ and a balance in He). Reprinted from Ref. ³² with permission from Springer Nature. (B) N_2O conversion at 600 °C with and without O_2 for Pt, Pd, and Ir on alumina catalysts with insight to surface morphology. Reprinted from Ref. ³³ with permission from Elsevier. Oxygen content produced from isotopic $^{15}\text{N}_2^{18}\text{O}$ pulse experiment on 0.5 wt% Rh on (C) Al_2O_3 and (D) CeO_2 to show the evolution of oxygen species, highlighting the oxygen donating role of the CeO_2 support. C and D reprinted from Ref. ²⁷ with permission from Elsevier.

observed, as shown in Fig. 4B, which the authors suggested benefit the activity by easing oxygen desorption from defect-free surfaces, reducing oxygen-induced site blocking. Regardless of whether the high performance is from the active metal itself or properties derived from the support, oxygen desorption is essential to increase conversion due to competitive binding to active sites on the metal surface.

Parres-Esclapez et al. analyzed the activity of the Rh/ CeO_2 catalyst on N_2O decomposition and found that CeO_2 had a higher rate of N_2O decomposition than Al_2O_3 catalysts.²⁷ The authors related the difference in rate to different physicochemical properties of the catalysts. They noted that the apparent activation energy for Rh/ CeO_2 was ~25 kJ/mol less than that of the Rh/ Al_2O_3 , possibly indicating different mechanisms for decomposition on CeO_2 versus Al_2O_3 . To elucidate the potential mechanisms over the catalysts, pulse decomposition experiments were conducted with $^{15}\text{N}_2^{18}\text{O}$. The study showed that the $\gamma\text{-Al}_2\text{O}_3$ -supported catalyst produced $^{18}\text{O}_2$ as the primary product, which indicated that the majority of the oxygen produced was a result of oxygen atoms coming from N_2O via the Eley-Rideal mechanism. However, when conducting the same experiment with the Rh/ CeO_2 catalysts at 350 °C, ~50% $^{18}\text{O}^{16}\text{O}$ evolved from the system. This indicated a more substantial participation of the support oxygen in the overall reaction mechanism. Therefore, the group noted the important role that the CeO_2 support plays in exchanging oxygen atoms from the surface of the support to produce molecular oxygen, which was not as prominent for the $\gamma\text{-Al}_2\text{O}_3$ -supported catalysts to as great an extent, as shown in Fig. 4C.²⁷

Zhu et al. performed an in situ diffuse reflectance infrared Fourier transform spectroscopy (DRIFTS) experiment with Rh/ CeO_2 catalysts.³⁵ The DRIFTS measurements showed N_2O adsorption peaks both on the Rh sites and CeO_2 support, indicating that both the metal and support play a role in the reaction mechanism, as also observed by Parres-Esclapez et al.^{27, 35} Prior to N_2O -DRIFTS, the samples were reduced, facilitating the formation of Ce^{3+} sites, or oxygen vacancies. The N_2O -DRIFTS data showed that support can be oxidized under N_2O , from Ce^{3+} to Ce^{4+} , providing insight into the redox abilities and role of supports in the N_2O decomposition mechanism.³⁵ However, the authors noted that Ce^{4+} was not reduced to Ce^{3+} in their experiments at room temperature, indicating O_2 desorption as a rate-limiting step.

The role of supports on N_2O decomposition has been further studied by Yoshida et al., where Pt and Pd catalysts on SiO_2 - Al_2O_3 , SiO_2 , Al_2O_3 , ZrO_2 , MgO (listed from most acidic to least acidic) supports were investigated.⁷⁶ The study aimed to relate how the acidity of the support impacts the oxidation and reduction properties of the catalysts, which is of concern due to the oxidative nature of the reaction. The researchers found that more acidic supports can suppress oxidation of the metal at lower temperatures, which can promote the desorption of O_2



and increase conversion. This suggests that the support can aid in resisting oxygen site blocking and further enhance the reaction conversion.

Similarly, Dacquin et al. studied a Pd-supported catalyst on γ - Al_2O_3 and LaCoO_3 .³⁴ When comparing the N_2O conversion during a temperature programmed experiment using a mixed stream of dry 1,000 ppm NO and 1,000 ppm N_2O gases, it was found that the conversion increased from 15% on Pd/ Al_2O_3 to 32% on Pd/ LaCoO_3 at 460 °C, and the apparent activation energy decreased from ~93 to ~55 kJ/mol. The authors concluded that the increase in conversion and lower barrier arises from an interaction between the Pd and the reducible LaCoO_3 support that can create anionic oxygen vacancies and supplies labile oxygen species, as seen with the increased intrinsic activity ceria.^{27, 34}

The inclusion of promoters can have an equally impactful role as the support on N_2O decomposition. Haber et al. found that alkali-metal promoters further enhanced the N_2O decomposition reaction by increasing metallic dispersion (prior to reaction).³⁶ The study examined a series of Rh/ γ - Al_2O_3 catalysts with various alkali promoters. The Cs promoted catalyst gave the overall lowest T_{50} number (T_{50} performance based on promoters ranked from lowest to highest: Cs, K, Li, Na). The Li and Na-promoted catalysts experienced a clear optimum weight loading at 0.078 mol% of alkali metal oxide, whereas the Cs and K-promoted catalysts did not exhibit such a sharp optimum. The improved activity for the catalysts with larger alkali metals was attributed to an increased Rh dispersion, resulting from an electron-donating effect from the promoters. X-ray photoelectron spectroscopy (XPS) confirmed that the alkali metals increased the electron-density/charge effect on support oxygen, which may hinder Rh diffusion and suppress particle growth. In addition, Pd has been found to have a promotional effect towards Rh/ ZrO_2 catalysts.³⁷ Zhang et al. found that not only did Pd enhance the catalytic activity and decrease the overall activation energy but also influenced the ability to reduce Rh species to their active state and promote the formation of oxygen vacancies. Though also inhibited by O_2 , CO_2 , and H_2O , Pd promoted Rh catalysts still showed lower T_{50} values than the baseline Rh/ ZrO_2 catalyst.³⁷

Novel catalysts will continue to be researched to drive innovation and progress towards zero-emission processes. Single-atom catalysts (SACs) dispersed on a support have also been explored due to their high atom efficiency and unique electronic properties.⁷⁷ Liu et al. synthesized a Pt SAC on a $\text{MgAl}_{1.2}\text{Fe}_{0.8}\text{O}_4$ spinel. Subsequent testing of the catalysts for N_2O decomposition revealed that the Pt SAC (calcined at 800 °C) had the lowest T_{50} , while the incipient wetness impregnation (IWI) catalyst (calcined at 300 °C) had the highest T_{50} .⁷⁸ Sun et al. developed a single-atom Ru on CeO_2 nanorods catalyst with an ultralow Ru loading of 0.48 wt% for the direct N_2O decomposition.³⁰ Using a combined experimental and computational approach, they found that the Ru/ CeO_2 SAC outperformed the Ru/ CeO_2 nanoparticles due to enhanced O_2

desorption and showed high O_2 resistance. On the contrary, by controlled synthesis and comparing Rh single atoms, nanoclusters (1.1 nm), and nanoparticles (2.1 nm) supported on defect-rich CeO_2 , Bao et al. reported that Rh nanoclusters exhibited a superior activity for direct N_2O decomposition compared to SAC and nanoparticles.⁷⁹ The recombination and desorption of oxygen were facilitated by the adjacent Rh atoms in the Rh cluster and positively charged Rh species. In addition to SACs, metal-organic frameworks (MOFs), which are highly porous three-dimensional crystalline materials composed of metal ions or clusters coordinated to organic ligands, are emerging as versatile and effective catalysts owing to their high surface area, tunable porosity, and customizable chemical functionality.⁸⁰ Palladium-loaded, metal-organic framework (MOF)-derived catalysts were developed with controlled thermal treatment to improve Pd dispersion for synergistic N_2O decomposition and CO oxidation.⁸¹ They found that the (2 %Pd/MIL)-T catalyst is highly active and achieved full N_2O decomposition at 550 °C under a space velocity of 240,000 $\text{ml}\cdot\text{h}^{-1}\cdot\text{g}_{\text{cat}}^{-1}$, which outperformed the commercial Pd/ Cr_2O_3 and previous MOF-based catalysts. Tang et al. utilized ZIF-67 frameworks as precursors for preparing Co/ CoO_x @Carbon catalysts for direct N_2O decomposition and achieved a low T_{50} value of 305 °C.⁸² It was noted that the ZIF67-derived amorphous graphitic carbon frameworks are instrumental in transferring/storing active oxygen and regenerating cobalt active centers. A hollow porous NiO@ CeO_2 octahedron catalyst derived from cerium-based metal-organic frameworks was prepared by Zhao et al. and showed a high activity for the N_2O decomposition.⁸³ By employing various characterization techniques, this remarkable catalytic performance was attributed to the hollow porous structures, uniform Ni dispersion, and large amount of oxygen vacancies in the MOF-derived Ni/ CeO_2 catalyst.

2.2 Metal Oxides

The scarcity and price of precious metals continuously drive research to find alternative catalysts that provide increased conversion at a lower cost. Therefore, improving the desorption of oxygen and regeneration of active sites for transition metal oxides and mixed oxide catalysts, such as Co, Mn, Cu, and Ni oxides, is essential to identify precious metal alternative catalysts for N_2O decomposition.^{31, 42, 43, 45, 48} For metal oxides, the metal sites tend to exhibit various oxidation states, which can influence the complexity of the catalyst and reaction conversions.

Yamashita and Vannice analyzed the different oxidation states of Mn oxide catalysts to determine the most active oxidation state of Mn.⁴² The study analyzed the performance of MnO, Mn_3O_4 , Mn_2O_3 , and MnO_2 and found that Mn_2O_3 had the largest sustained N_2O decomposition rate of $1400 \times 10^{-4} \mu\text{mol}\cdot\text{s}^{-1}\cdot\text{g}_{\text{cat}}^{-1}$, compared to MnO, which had a rate of $6.3 \times 10^{-4} \mu\text{mol}\cdot\text{s}^{-1}\cdot\text{g}_{\text{cat}}^{-1}$. When analyzing the decomposition products, the Mn_2O_3 catalyst produced stoichiometric decomposition products compared to the MnO catalyst, which only produced N_2 as a



ARTICLE

Catalysis Science & Technology

product. The authors indicate that other Mn oxides were being oxidized to Mn_3O_4 , thus hindering the overall catalytic performance.⁴² where it is concluded that the Mn^{3+} oxidation state is the active site for this reaction.

There have been additional studies conducted to elucidate the mechanism for N_2O decomposition. Jing et al. conducted operando XAS studies to better understand the decomposition mechanism on a $\text{RhO}_x/\text{ZrO}_2$ catalyst, which displayed high activity in an N_2O environment as well as with other inhibitors, such as O_2 and H_2O . In their study, the catalysts were first treated with a heating step.⁸⁴ In conducting in situ XANES, the researchers elucidated that the heating step allowed for an initial reduction of Rh, forming defect sites on the catalyst. Following this study, the group introduced 1% N_2O to their sample and analyzed the effluent with a GC while analyzing the catalyst using XANES. When conducting their study, the group found that the XANES spectra shifted to higher energy. Simultaneously, they saw N_2 and O_2 in the effluent from their GC data. The authors suggested that this displayed how the N_2O acted as an oxidizing agent to the Rh. Relating this to the in situ XANES that was conducted, the authors suggested that the defect sites formed during the high temperature treatment facilitated the decomposition of N_2O , further displaying how this reaction proceeded via a redox mechanism. Another operando study conducted by Jing et al. elucidated the impact of adding Ag as a promoter to a $\text{RhO}_x/\text{Al}_2\text{O}_3$ catalyst.⁸⁵ From their study using operando diffuse reflectance UV-vis, they found that the silver promotes the reduction of the Rh species, which is necessary to form defect sites for the reaction to occur as they previously found.^{84, 85}

In addition to identifying catalyst active sites, the influence of common inhibitors is important in understanding the functionality of the catalyst. Wilczkowska et al. analyzed the possible activation and deactivation mechanisms due to the presence of O_2 or H_2O in the feed stream for a Co oxide spinel catalyst.³¹ They found that O_2 inhibited the reaction at lower temperatures (<800°C), but increased activity at higher temperatures compared to experiments when O_2 was not present in the feed. The authors noted that the initial reduced activity at lower temperatures in the presence of O_2 can be attributed to competitive adsorption of O_2 on the active sites, creating a saturated Co species. XRD analysis revealed that the addition of O_2 in the feed stabilized the active Co_3O_4 state at higher temperatures, whereas in an anoxic environment, the catalyst was reduced to CoO. When H_2O was present in the feed, the activity had decreased with XRD revealing the catalyst to be reduced, while H_2O blocked active sites due to competitive adsorption. This result was further confirmed from XPS with an increase in the ratio of $\text{O}_{\text{ads}}/\text{O}_{\text{latt}}$ (where O_{ads} and O_{latt} are the oxygen associated with hydroxyl groups and the lattice, respectively) when H_2O was present in the feed.³¹ This was attributed to the competitive adsorption on the surface of the cobalt oxide catalyst.

Many studies have aimed to identify dopants and promoters that will both enhance the reaction as well as regenerate the active centers. Zabitskiy et al. sought to understand the role of incorporating CuO supported on CeO_2 nanorods.⁴³ Through XPS, the addition of CeO_2 to the catalyst was found to facilitate the increase in anion defect sites (oxygen vacancies). High-angle annular dark-field scanning transmission electron microscopy showed that the surface of the catalysts was enriched with Ce^{3+} while the bulk was enriched with Ce^{4+} . The authors attributed this to the ability of Ce to generate labile oxygens to regenerate the active Cu⁺ sites, which is portrayed in Fig. 5A.⁴³ In addition, an increased activity for CuO on CeO_2 was correlated to Ce^{3+} ions, determined by operando ultraviolet-visible spectroscopy (UV-Vis).⁴³ It was concluded that a $[\text{Cu}-\text{O}-\text{Cu}]^{2+}$ species is formed on the surface with labile oxygens from the CeO_2 support donating species to help promote the formation of the active copper complexes.⁴³

Some studies have also been performed on the role of alkali and alkali earth promoters on metal oxide catalysts. Xue et al. studied the incorporation of alkali and alkali earth metals into a cobalt-cerium composite oxide catalyst.⁴⁴ The study determined that the alkali metal-promoted oxide had lower T_{50} numbers, with Cs showing the best T_{50} of ~225 °C (compared to the unpromoted oxide, T_{50} of ~350 °C), as shown in Fig. 5B. The authors attributed this impact to an electronic effect on Co^{2+} .⁴⁴ This was further evidenced with O_2 -temperature programmed desorption (TPD) and H_2 -TPR. The authors found that larger-element alkali-promoted catalysts facilitated O_2 desorption at lower temperatures due to having a lower overall desorption intensity, while there was an increase in reducibility to regenerate the Co^{2+} site as evidenced with H_2 -TPR. This indicated that the alkali metals donate electrons to facilitate oxygen desorption and increase N_2O conversion to regenerate the active site.⁴⁴

Zhao et al. sought to understand the impact of utilizing Cs as a promoter on common oxides, such as Co_3O_4 , CuO, NiO, and Mn_2O_3 .⁴⁵ The study found that the addition of Cs, as the most basic alkali metal, had a positive impact on the Co_3O_4 and CuO catalysts and an inhibiting impact for NiO and Mn_2O_3 catalysts (an increased T_{50} number). For Co_3O_4 , the T_{50} number decreased by ~150 °C from the unpromoted catalyst and outperformed the worst-performing catalyst (Cs/ Mn_2O_3) by ~235 °C. This change in activity was accompanied by a decrease in activation energy for the Co and Cu catalysts and an increase in activation energy for the Ni and Mn (inhibited) catalysts. For the Cs/ Co_3O_4 catalyst, XPS showed an increase in the Co^{3+} fraction (considered the active center of the catalyst) with increasing Cs concentration. In addition, the authors found that the O 1s peak of the Co was shifted to lower binding energies (529.8 eV to 529.4 eV) when promoted with Cs, indicating a potential electronic effect through the donation of electrons to the active center. Additionally, H_2 -TPR showed that the first metal



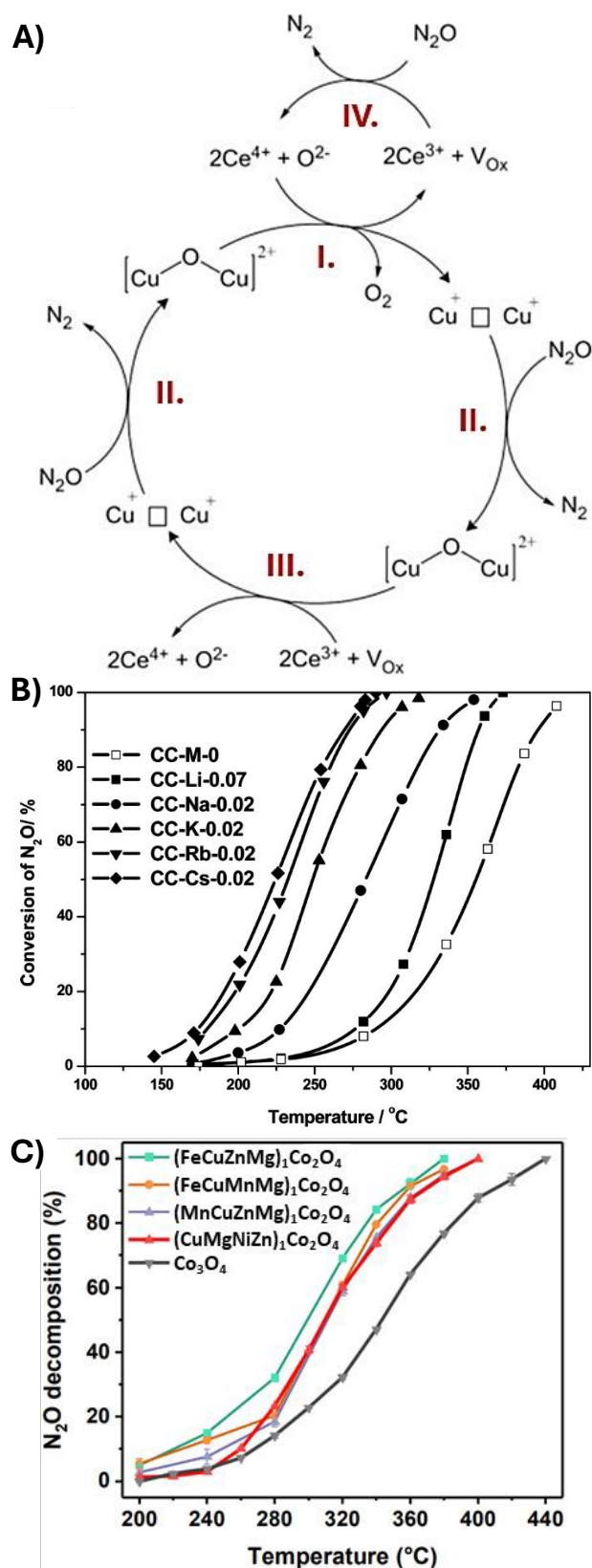


Fig. 5. (A) A proposed N_2O decomposition mechanism for a CuO/CeO_2 oxide catalysts. Adapted from Ref. ⁴³ with permission from Elsevier. (B) Light-off curve plots of alkali metal promoted cobalt-cerium composite oxides. Reprinted from Ref. ⁴⁴ with permission from the American Chemical Society. (C) Light-off curve plots for spinel Co_3O_4 -based HEOs. Adapted from Ref. ⁵⁷ with permission from the American Chemical Society.

reduction peak of Cs promoted Co-based catalysts was shifted to lower temperatures. However, the second reduction peak for Co-based catalysts and all of the reduction peaks for the Cu-based catalysts were shifted to higher temperatures, indicating that Cs donated electrons to stabilize the active centers of these catalysts. When compared to Ni and Mn catalysts, which experienced poorer performance when doped with Cs, the TPR reduction peaks shifted slightly, indicating a lesser ability to be reduced, possibly explaining the decreased performance.⁴⁵

Abu-Zied et al. chose to incorporate Rb into a Co_3O_4 - CeO_2 mixed oxide catalyst and analyzed the impact of changing the dopant concentration from 0.0125–0.2 ratio of Rb to Co.⁴⁶ Similarly to Zhao et al., they found that the role of Rb was to enhance the ability of Co^{2+} to donate electrons to the N_2O to facilitate decomposition.^{45, 46} This was confirmed through XPS results as well as a decrease in the T_{50} number for the Rb fraction of 0.025 (T_{50} was ~ 350 °C compared to the unpromoted cobalt oxide, which was about 450 °C).⁴⁶

Despite numerous studies analyzing the impact of promoters, there have been few studies that sought to examine more “exotic” promoters, such as lanthanides. Lanthanides are known to have increased redox properties due to having an unfilled 4f orbital.⁴⁷ Liu et al. analyzed the impact of doping Co_3O_4 catalysts with samarium (Sm). Through in situ XPS experiment that exposed the catalyst to 5,000 ppm of N_2O at various temperatures, the authors saw that there was no difference (or shift) in the Co-2p XPS spectrum under reaction conditions, indicating a stable Co active site. However, the Sm-3d spectra shifted to higher binding energies throughout the exposure to N_2O at different temperatures, indicating that the role of the samarium was to transfer electrons to cobalt to stabilize/regenerate the active site.⁴⁷ Similarly, Zhang et al. looked at the impact of doping NiO with praseodymium and found that praseodymium increased the overall surface area of the catalyst and improved the conversion to reach 100% at ~ 400 °C (which is roughly the T_{50} of unpromoted NiO).⁴⁸ In addition, they found that with the addition of Pr, there were little differences in activity when placed in a feed with oxygen, which is typically an inhibiting gas. From XPS, these researchers observed that praseodymium helped weaken the nickel-oxygen bond, increasing the number of surface oxygens and promoting oxygen vacancies, as well as enhancing the reducibility of nickel. These factors are crucial for regenerating the active sites of the catalysts.⁴⁸ Other studies have found similar results when promoting Co_3O_4 catalysts with other lanthanides. Sun et al. promoted a Co_3O_4 catalyst with Ce and Pr.⁴⁹ They found that the Ce was imperative to aid in the formation of oxygen vacancies but overall restricted the formation of crystalline Co_3O_4 . When Pr was doped into the catalyst, it added an electronic effect to further enhance the redox properties of the catalyst.⁴⁹ Dy has also been investigated as a promoter to Co_3O_4 catalysts.^{50, 51} As previously described, alkali metals, such as K, have been discovered as beneficial towards increasing decomposition activity due to having strong electron donating properties.



ARTICLE

However, studies have noted that in the presence of inhibiting gases, such as NO_x and CO₂, the role of K becomes inhibited. To further aid in decreasing the Co-O bond and strengthen the redox capabilities of the active species, Dy has been found to be an effective promoter.^{50, 51}

In addition, there have been various studies discussing further elements that can improve the activity of Co₃O₄ catalysts.⁵²⁻⁵⁵ In short, Bi has been noted to create more active Co₃O₄ catalysts by increasing surface area and exposing more active crystal planes.⁵² Other non-metal atoms, such as F and N have also been used as dopants to Co₃O₄ catalysts and are noted to promote the reaction by enhancing the surface basicity of the catalyst while creating more oxygen vacancies for the reactions to occur.^{53, 54}

High entropy oxides (HEOs) have been shown to exhibit unique properties beyond the sum of their constituent components and often outperform their mono- or bi- component counterparts. Recently, Li et al. explored a HEO spinel structure based on Co₃O₄ for N₂O decomposition.⁵⁷ The (CuMgNiZn)₁Co₂O₄ HEO outperformed Co₃O₄, as well as each bimetallic MCo₂O₄ (M = Cu, Mg, Ni, Zn). The HEO had a lower T₅₀ (313 °C) and activation energy (89.6 kJ/mol) than the base Co₃O₄ (343 °C and 119.9 kJ/mol, respectively) and demonstrated a higher thermal stability over 12 h (Fig. 5C). The enhanced performance was attributed to the abundance of surface oxygen vacancies, caused by the lattice distortion due to multiple cation sizes. N₂O decomposition was also studied on a La_{0.7}Ba_{0.3}Mn_{0.8}In_{0.2}O₃ by Ishihara et al.⁵⁸ The base LaMnO₃ perovskite structure was modified by partial replacement of La and Mn with Ba and In, respectively, leading to a lower T₅₀ value of 443 °C. While not a true HEO by definition, this complex oxide material highlights property enhancement based on cation substitution.

2.3 Zeolites

Zeolites have been extensively studied for their role in the decomposition reaction of N₂O. Specifically, zeolites can boost N₂O decomposition due to various characteristics, such as the increased surface area and structure giving rise to shape selectivity and control.²⁶ In addition, zeolites can support reactions due to their acidity.^{25, 26} Likewise, BEA and SSZ-13 have shown an additional benefit of hydrothermal stability, which is important for some processes that produce N₂O and contain water in the feed.²⁴ (Note: three-letter codes for zeolite structures are assigned by the International Zeolite Association.⁸⁶) Common zeolite structures for N₂O decomposition reactions are shown in Fig. 6A-D with labeled pore sizes.

Fe, Cu, and Co have been studied extensively for N₂O decomposition when exchanged into zeolites. Lin et al. analyzed Fe, Cu, and Co over a SSZ-13 zeolite and determined that the Fe-SSZ-13 catalyst had the largest decomposition rate when compared to the Co- and Cu-exchanged catalysts.²⁸ H₂-TPR and

FTIR showed that the Fe-exchanged catalysts were found to have active dimeric [Fe-O-Fe] sites for decomposition, as well as Cu-exchanged catalysts having many dimeric Cu²⁺ sites to aid in the recombination of oxygen for the reaction mechanism.²⁸ The results indicate a dual site mechanism for both the Fe and Cu-based zeolites, compared to Co-exchanged zeolites, which displayed single Co²⁺ sites.²⁸ The authors related the apparent activity towards the trends in the activation energy, where the Fe-exchanged zeolites showed the lowest activation energy, corresponding to the highest reaction rate.

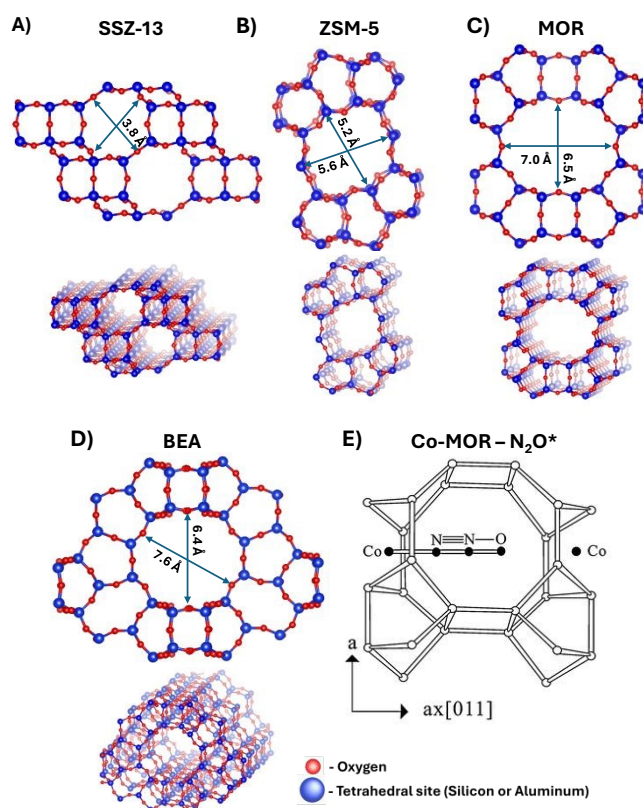


Fig. 6. (A–D) Structures for SSZ-13, ZSM-5, MOR, and BEA with associated pore sizes of commonly utilized zeolites for N₂O abatement reactions. Structural data from Refs. ⁸⁷⁻⁹⁰, respectively. (E) Graphical representation of the interaction between N₂O and a β-type Co site of a Co-MOR zeolite. Reprinted from Ref. ⁶² with permission from the Royal Society of Chemistry.

The formation of active sites depends on the interaction of metal ions with the zeolite framework. Zhang et al. analyzed how the structure of zeolites impacted the generation of Co active sites for N₂O decomposition.⁶² The study analyzed Co, exchanged into ZSM-5, BEA, MOR, and USY zeolites and found that the activity (based on lowest T₅₀ value to highest T₅₀ value) followed: MOR>BEA≈ZSM-5>USY, with a difference in T₅₀ values of ~100 °C between the best and worst performing catalyst. The catalysts exhibited similar, yet slightly different, results when comparing activity in terms of turnover frequency (ZSM-5>BEA>MOR>USY) but yielded a different result when comparing with Co loading (MOR> USY>BEA>ZSM-5). Not only could the differences be attributed to the type of zeolite, but



the types of active sites as well as coordination to the framework were also found to be impactful. NO-FTIR (with NO used as a probe molecule), H₂-TPR, and UV-Vis DRS (diffuse reflectance spectra) revealed that the more active catalysts (Co-ZSM-5, Co-MOR, and Co-BEA) had larger amounts of Co²⁺ sites compared to Co-USY, which had an increased amount of cobalt oxide.⁶² It was found that an increase in Co concentration decreased the population of α -type Co²⁺ ions (Co²⁺ coordinated to four framework oxygens in the straight channel) and increased the β -type Co²⁺ ions (coordinated to more oxygens in the framework/cavity). This trend was evidenced more prominently in Co-BEA and Co-MOR when compared to Co-ZSM-5. The authors noted that the α -type sites for the ZSM-5 catalysts enable an increased interaction between the reactants and ions, with a decreased interaction between the ion and the framework, which attributed towards increased interactions with the reactants to facilitate decomposition. Similarly, they found that weaker bonds were formed between the Co²⁺ ion and the framework oxygens of the BEA zeolite in a β -type site, allowing the ions to coordinate with N₂O for the reaction despite having more diffusional hinderances due to zeolite structure. On the other hand, the Co ions exchanged into MOR in a β -type site exhibited increased bonding of the ion to the framework, which decreased the affinity of the bonds to N₂O. Though less accessible to bonding to the reactants, the authors noted that the structure within the MOR cavity locates Co²⁺ ions in close proximity with one another leading to the formation of ion pairs that can facilitate N₂O decomposition (Fig. 6E).⁶²

Not only does the zeolite structure impact the reaction, but the ion exchange ratio and Si/Al ratio can impact the kinetics and mechanism of the reaction. Fanson et al. studied the Cu-ZSM-5 zeolite while analyzing the impact of the Si/Al ratio and Cu-exchange level on the kinetic rate oscillations for N₂O decomposition to understand surface reaction intermediates.⁹¹ They found that higher Si/Al ratios resulted in kinetic rate oscillations. The authors attributed these oscillations to the formation and coverage of a nitrate species intermediate that formed due to the interaction of N₂O with the extra lattice oxygen in the zeolite. They concluded that the mechanism involves the conversion of N₂O to NO, which was shown to be rate determining step of this reaction on zeolites with a higher Si/Al ratio.⁹¹

Aside from the transition-metal exchanged zeolites, Sobalik et al. analyzed the impact of incorporating noble metals (Pt, Rh, and Ru) into Fe-FER zeolites.⁶³ It was found that when Fe and the noble metals were incorporated into the zeolite together, the T₅₀ number decreased from ~420–450 °C for monometallic-FER zeolites to ~360–410 °C for bimetallic zeolites. In conducting isotopic experiments, the authors attributed this increased activity towards the ability of the noble metals to enhance recombination of the oxygen species that were bound to the surface and decreased the role of the oxygens from the framework of the zeolite.⁶³

The role of the zeolite is also important in addition to the properties of the metals that allow for the reaction to occur. Guzmán-Vargas et al. synthesized Fe-exchange zeolites with BEA, FER, and ZSM-5 type zeolites.⁶⁴ Guzmán-Vargas et al. found the Fe-FER zeolite to be the most active with the lowest T₅₀ (~417–437 °C) compared to the least active, which was the Fe-ZSM-5 (T₅₀: ~497–507 °C). The authors related this difference in activity towards the ability of the host zeolite to yield “oxo-species,” where there is a cation in the species. They found through H₂-TPR that the Fe-FER catalysts were able to generate these species, which is indicative of the active iron complex for the reaction.⁶⁴ Wang et al. also analyzed how the influence of the host zeolite impacted the formation of the active centers and related it to the apparent N₂O decomposition activity.²⁴ In their study, they exchanged iron into both BEA and SSZ-13 zeolites. Based on UV-Vis experiments, the authors found that the Fe-BEA zeolites had larger proportions of dimers and oligomeric iron-oxides as well as Fe₂O₃ particles, which are inactive. This aligns with their catalytic activity tests.²⁴

The porosity of the zeolite can also impact the reaction. Lim et al. looked at a variety of Fe-exchanged small pore zeolites, and they found that the smaller pore zeolites, such as the H-Fe-PST-7, outperformed the medium-pore zeolites, such as the Fe-ZSM-5.⁶⁵ Similarly, Rutkowska et al. sought to increase the surface area by decreasing the micropore volume of zeolites by incorporating BEA to SBA-15.²⁶ When analyzing N₂ adsorption-desorption tests, they found that they were able to increase the mesoporosity of the zeolite while decreasing the micropore volume. When exchanging Fe into the catalysts, they found that there was an increase in Fe³⁺ centers when compared to the Fe-BEA catalysts, which had more Fe₂O₃ structures in the extra framework. Though there was an increase in iron-oxides in the Fe-BEA, these catalysts still had similar activity to the micro/mesoporous structures. The authors did note, however, that these micro/mesoporous zeolites had a lower iron loading, as found through UV-Vis, thus indicating that the introduction of mesoporosity can boost activity.²⁶ Wu et al. also examined the value of adding mesopores to zeolites through alkaline treatment.⁶⁶ They found that with the alkaline treatment, the overall ion-exchange percentage increased between the parent zeolite and the modified zeolite, which correlated to a decrease in T₅₀ (of between 50–100 °C) for all alkaline and parent zeolites.⁶⁶

Furthermore, various operando studies have been conducted to elucidate the reaction mechanisms on Fe-zeolites. Cano-Blanco et al. performed a series of operando investigations on Fe-zeolites and discovered through operando diffuse reflectance UV-vis (DRUV) spectroscopy that N₂O decomposition on these materials is controlled by the reduction process in the redox mechanism, which was rate-limiting.⁹² By coupling these findings with a series of other operando techniques, such as DRIFTS and electron paramagnetic resonance (EPR) spectroscopy, the researchers concluded that the Fe ions in the 6-membered rings playing a crucial role in the reaction mechanism. These Fe ions can complete the redox cycle



necessary to regenerate active sites. Operando EPR studies further identified the Fe²⁺ species in the 6-membered ring of the zeolite as the active component for N₂O decomposition.⁹²

2.4 Impact of Inhibiting Gases

The above three subsections focus on the direct decomposition activity of three main catalyst types in more “idealized” gas feeds, which may not be the actual operating conditions these catalysts may face in industrial applications. Many industrial processes, such as denitrification,⁸ treatment of byproducts from ammonia combustion,⁹ adipic acid production and nitric acid production,¹² as well as byproducts from three-way catalytic converters produce other byproducts, such as NO_x, O₂, H₂O, and SO₂.¹¹ Many studies on direct decomposition catalysts show an inhibiting effect of NO, O₂, H₂O,²¹ and SO₂.^{43, 46, 93} Specifically, it has been noted in literature that NO, O₂, and H₂O have reversible inhibitory effects, indicating competitive adsorption/site blocking of the catalytic active sites.^{31, 94} Some literature has also suggested that NO decreases catalytic activity in that it has a competitive reaction pathway with labile oxygen in a CuO/CeO₂ catalyst.²¹ SO₂ has also been found to negatively impact N₂O decomposition.^{40, 93} One study conducted a step change experiment in which various concentrations of SO₂ were added or removed while running the experiment for 8 h. It was found that SO₂ negatively impacted the performance with some irreversible deactivation in that the performance did not fully return to the initial activity once removing SO₂.⁹³ Studies suggest that the SO₂ is responsible for creating Brønsted acid sites on Pd/Al₂O₃ catalysts, which alters the oxidation state of the active material causing the irreversible deactivation.⁴⁰ For further catalytic improvement for such compounds, adding promoters or dopants can help facilitate the desorption and/or weaker binding of these inhibiting compounds, which creates a more robust catalyst under industrial conditions.^{37, 45, 49-55} Yu et al. found that doping a Co₃O₄ catalyst with K and Dy improved the catalyst's performance and stability in environments containing NO, O₂ and H₂O.⁵¹ In addition, the choice of support or oxide is important as it could reduce the negative impacts water and O₂ have on the N₂O decomposition.^{93, 95, 96}

2.5 Direct Decomposition Catalyst Durability

In addition to catalytic activity, catalyst durability is a critical property for the industrial application of direct decomposition and SCR of N₂O processes, especially under actual plant operating conditions.

The catalyst durability in the direct decomposition of N₂O has been investigated in literature, with some studies using industry-relevant feed stream and reaction conditions. Porous Fe₂O₃-ZrO₂ and NiO-ZrO₂ nanocomposites were tested for direct N₂O decomposition and showed a stable N₂O conversion at 500 °C for 120 hours.⁹⁷ In this case, the robust catalytic performance was attributed to the presence of reducible M-O-Zr (M = metal) interactive species and crystalline tetragonal ZrO₂ phase. Sádovská et al. studied the catalyst durability of Fe-FER, which is one of the highly active zeolite-based catalysts for N₂O decomposition.⁹⁸ The Fe-FER catalyst was exposed to a gas

stream produced by NH₃ oxidation over Pt wire at 800 °C, which is the real conditions in the secondary stage of N₂O abatement during HNO₃ production, for 12 days. They found that the FER zeolite structure remained stable and the catalytic activity associated with Fe(II) cations for the N₂O decomposition was preserved after the catalyst aging under real process conditions. The excellent catalyst durability of Fe-FER compared to Fe-MFI under real conditions of nitric acid production plants was also discussed in other studies.^{99, 100} Melián-Cabrera et al. reported a stable N₂O conversion (~ 80%) for 50 hours at 427 °C with the presence of H₂O and O₂ in the feed stream, which was attributed to the stabilization of iron species in the FER matrix.¹⁰⁰ Giecko et al. studied the N₂O decomposition on Fe₂O₃/Al₂O₃ catalysts, which showed insignificant activity loss after 180h time-on-stream in the pilot plant and 3300h time-on-stream in the real nitric acid production plant.¹⁰¹ In another study on the N₂O decomposition from adipic acid plant, Alini et al. found that CaMn_{0.6}Cu_{0.4}O₃ perovskite catalyst has good stability when tested under real industrial conditions at the temperature of 700 – 750 °C for 1400 hours using off-gas stream that contains H₂O, O₂, CO₂, and N₂O.¹⁰² Wang et al. also tested a Co₃O₄ catalyst co-doped with Ni and Y and found it remained stable for 40h with performance being attributed towards the promoters' role in enhancing O₂ desorption, increasing electron donation abilities of the active ions, increasing the basicity of the catalyst, as well as promoting the reduction of Co³⁺ to Co²⁺.⁵⁵

3 Selective Catalytic Reduction of Nitrous Oxide

In addition to the direct catalytic decomposition of N₂O, the SCR of N₂O has gained significant attention from the scientific community and industry alike.¹⁰³ The presence of reductants benefits the conversion of N₂O over different heterogenous catalysts, as it lowers the reaction temperature required for reducing N₂O into inert nitrogen molecules. There are four main reductants that have been studied extensively in the literature for the SCR of N₂O processes and will be discussed in the following sections: CO, hydrocarbons, NH₃, and H₂. The catalytic performance of SCR catalysts, indicated by T₅₀ values, under various reaction conditions are summarized in Table 2 and Fig. 2C. In general, it shows that iron-zeolites are the most studied catalysts for the SCR of N₂O, especially when NH₃ is used as the reductant. The reaction mechanisms and the influence of common industry-relevant impurity gases, such as NO, O₂, H₂O, and SO₂, on the SCR of N₂O are discussed in this section.

3.1 Carbon Monoxide (CO-SCR)

CO has been considered an efficient and selective reductant for the conversion of N₂O. In general, CO can react with adsorbed oxygen and remove these atoms from the catalyst surface (also known as a scavenging effect), leading to a considerably decreased reaction temperature compared to the direct catalytic decomposition of N₂O.^{69, 70} There are two main reaction mechanisms of N₂O reduction by CO proposed in



Table 2: Summary of N₂O SCR catalysts, grouped by reductant from top to bottom: CO, hydrocarbons, NH₃, and H₂. T₅₀ represents the temperature at which 50% conversion is reached, with flow conditions being defined by the gas hourly space velocity (GHSV), weight hourly space velocity (WHSV), or ratio of catalyst weight to volumetric gas flow rate (W/F). Note: GHSV, WHSV, and W/F were standardized based on feed conditions presented in the literature source for further comparison.

| Reductants | Other reactants* | Inhibitors† | Catalyst | Catalyst synthesis | Catalyst pretreatment | GHSV (h ⁻¹) | WHSV (h ⁻¹) | W/F (g·s·mL ⁻¹) | Feed composition | T ₅₀ (°C) | Ref. |
|------------|------------------|----------------|---|--|--|-------------------------|-------------------------|-----------------------------|--|----------------------|------|
| CO | | | Pt/Al ₂ O ₃ -CeO ₂ -La ₂ O ₃ | Co-precipitation, impregnation | H ₂ /He, 400 °C, 1 h followed by He, 400 °C, 1h | 10,000 | | | 0.1% N ₂ O, 0.1% CO, He balance | 239 | 38 |
| CO | | O ₂ | Pt/Al ₂ O ₃ -CeO ₂ -La ₂ O ₃ | Co-precipitation, impregnation | H ₂ /He, 400 °C, 1 h followed by He, 400 °C, 1h | 10,000 | | | 0.1% N ₂ O, 0.1% CO, 2% O ₂ , He balance | 427 | 38 |
| CO | | | Al-Pd-Co-O Mixed Oxide | Co-precipitation of hydrotalcite-type precursors | | 30,000 | | | 12,500 ppm N ₂ O, 17,500 ppm CO, N ₂ balance | 133 | 61 |
| CO | | | Al-Rh-Co-O Mixed Oxide | Co-precipitation of hydrotalcite-type precursors | | 30,000 | | | 12,500 ppm N ₂ O, 17,500 ppm CO, N ₂ balance | 160 | 61 |
| CO | | | Co-Rh-Al-O Mixed Oxide | Co-precipitation of hydrotalcite-type precursors | N ₂ , 500 °C, > 3 h | 30,000 | | | 12,500 ppm N ₂ O, 17,500 ppm CO, N ₂ balance | 173 | 59 |
| CO | | | Co-Pd-Al-O Mixed Oxide | Co-precipitation of hydrotalcite-type precursors | N ₂ , 500 °C, > 3 h | 30,000 | | | 12,500 ppm N ₂ O, 17,500 ppm CO, N ₂ balance | 174 | 59 |
| CO | | NO | Al-Pd-Co-O Mixed Oxide | Co-precipitation of hydrotalcite-type precursors | | 30,000 | | | 12,500 ppm N ₂ O, 17,500 ppm CO, 100 ppm NO, N ₂ balance | 256 | 61 |
| CO | | | Co-Mn-Al-O Mixed Oxide | Co-precipitation of hydrotalcite-type precursors | He, 450 °C, 1 h | | 10.9 | | 0.1 mol% N ₂ O, 0.15 mol% CO, He balance | 297 | 60 |
| CO | | O ₂ | Co-Mn-Al-O Mixed Oxide | Co-precipitation of hydrotalcite-type precursors | He, 450 °C, 1 h | | 10.9 | | 0.1 mol% N ₂ O, 0.15 mol% CO, 20 mol% O ₂ , He balance | 447 | 60 |
| CO | | O ₂ | Co-Pd-Al-O Mixed Oxide | Co-precipitation of hydrotalcite-type precursors | N ₂ , 500 °C, > 3 h | 30,000 | | | 12,500 ppm N ₂ O, 17,500 ppm CO, 10,500 ppm O ₂ , N ₂ balance | 460 | 59 |



ARTICLE

Catalysis Science & Technology

| | | | | | | | | | | | |
|-------------------------------|----------------|--|-----------------------------------|--|---|--------|------|------|--|-----------|-----|
| CO | | | Fe/ZSM-5 | Sublimation | N ₂ O/He, 450 °C, 1 h | | 10.9 | | N ₂ O (1.5 mbar) and CO (0.3 – 1.5 mbar), He balance | 298 – 458 | 69 |
| CO | | | Fe-ZSM-5 | Ion exchange | O ₂ , 500 °C, 1 h | | 9.9 | | 1,000 ppm N ₂ O, 1,000 ppm CO, He balance | 306 – 460 | 104 |
| CO | | | Fe/silicalite | Isomorphous substitution, ion exchange, steam activation | N ₂ O/CO/He, 450 °C, 1 h | | 11.3 | | N ₂ O (1.5 mbar), CO (1 mbar), He balance | 362 | 68 |
| CO | | | Fe/ZSM-5 | Isomorphous substitution, ion exchange, steam activation | He, 450 °C, 2 h | 90,000 | | | N ₂ O (1.5 mbar), CO (0.2 – 3.0 mbar), He balance | 362 – 507 | 70 |
| CO | O ₂ | | Fe-BEA | Ion exchange | 3% H ₂ /Ar, 13 mL·min ⁻¹ , ramp from 80 – 700 °C at 10 °C·min ⁻¹ | 35,000 | | | 0.2% N ₂ O, 0.2% CO, 3% O ₂ , He balance | 369 – 377 | 67 |
| CO | | | Fe-USY | Ion exchange | He, 600 °C, 1 h | 30,000 | | | 5,000 ppm N ₂ O, 5,000 ppm CO, He balance | 372 | 72 |
| CO | O ₂ | | Fe-USY | Ion exchange | He, 600 °C, 1 h | 30,000 | | | 5,000 ppm N ₂ O, 5,000 ppm CO, 50,000 ppm O ₂ , He balance | 372 | 72 |
| CO | | | Fe/ZSM-5 | Isomorphous substitution, ion exchange, steam activation | He, 450 °C, 2 h | 90,000 | | | N ₂ O (1.5 mbar), CO (0.2 – 1.5 mbar), He balance | 381 – 509 | 71 |
| CO | | | Fe/ZSM-5 | Isomorphous substitution, steam activation | N ₂ O/He, 450 °C, 1 h | | 10.9 | | N ₂ O (1.5 mbar) and CO (0.3 – 1.5 mbar), He balance | 385 – 495 | 69 |
| CO | | | Fe/ZSM-5 | Isomorphous substitution, ion exchange, steam activation | N ₂ O/CO/He, 450 °C, 1 h | | 11.3 | | N ₂ O (1.5 mbar), CO (1 mbar), He balance | 408 | 68 |
| CO | NO | | Fe/ZSM-5 | Isomorphous substitution, ion exchange, steam activation | He, 450 °C, 2 h | 90,000 | | | N ₂ O (1.5 mbar), CO (1.5 mbar), NO (1.5 mbar), He balance | 413 | 70 |
| CH ₄ | | | Pd/Al ₂ O ₃ | Dry impregnation | He, 100 mL·min ⁻¹ , 600 °C, 1 h | 35,000 | | | 0.12% N ₂ O, 0.5% CH ₄ , He balance | 258 | 40 |
| C ₃ H ₆ | | | Rh/Al ₂ O ₃ | Dry impregnation | | | | 0.12 | 500 ppm N ₂ O, 1,000 ppm C ₃ H ₆ , He balance | 292 | 39 |



Journal Name

Catalysis Science & Technology

| | | | | | | | | | | | |
|-------------------------------|----------------|-----------------------------------|---|--|--|--------|--|------|---|-----------|-----|
| C ₃ H ₆ | | | Pt/Al ₂ O ₃ -CeO ₂ -La ₂ O ₃ | Co-precipitation, impregnation | H ₂ /He, 400 °C, 1 h followed by He, 400 °C, 1h | 10,000 | | | 0.1% N ₂ O, 0.1% C ₃ H ₆ , He balance | 317 | 38 |
| CH ₄ | | O ₂ | Pd/Al ₂ O ₃ | Dry impregnation | He, 100 mL·min ⁻¹ , 600 °C, 1 h | 35,000 | | | 0.12% N ₂ O, 0.5% CH ₄ , 5% O ₂ , He balance | 331 | 40 |
| CH ₄ | | SO ₂ | Pd/Al ₂ O ₃ | Dry impregnation | He, 100 mL·min ⁻¹ , 600 °C, 1 h | 35,000 | | | 0.12% N ₂ O, 0.5% CH ₄ , 300 ppm SO ₂ , He balance | 355 – 462 | 40 |
| CH ₄ | | H ₂ O | Pd/Al ₂ O ₃ | Dry impregnation | He, 100 mL·min ⁻¹ , 600 °C, 1 h | 35,000 | | | 0.12% N ₂ O, 0.5% CH ₄ , 3% H ₂ O, He balance | 376 – 414 | 40 |
| C ₃ H ₆ | O ₂ | | Rh/Al ₂ O ₃ | Dry impregnation | | | | 0.12 | 500 ppm N ₂ O, 1,000 ppm C ₃ H ₆ , 5% O ₂ , He balance | 392 | 39 |
| C ₃ H ₆ | O ₂ | SO ₂ | Rh/Al ₂ O ₃ | Dry impregnation | | | | 0.12 | 500 ppm N ₂ O, 1,000 ppm C ₃ H ₆ , 5% O ₂ , 50 ppm SO ₂ , He balance | 403 | 39 |
| C ₃ H ₆ | O ₂ | | Ru/Al ₂ O ₃ | Dry impregnation | | | | 0.12 | 500 ppm N ₂ O, 1,000 ppm C ₃ H ₆ , 5% O ₂ , He balance | 413 | 39 |
| C ₃ H ₆ | O ₂ | H ₂ O | Rh/Al ₂ O ₃ | Dry impregnation | | | | 0.12 | 500 ppm N ₂ O, 1,000 ppm C ₃ H ₆ , 5% O ₂ , 10% H ₂ O, He balance | 419 | 39 |
| C ₃ H ₆ | O ₂ | SO ₂ | Ru/Al ₂ O ₃ | Dry impregnation | | | | 0.12 | 500 ppm N ₂ O, 1,000 ppm C ₃ H ₆ , 5% O ₂ , 50 ppm SO ₂ , He balance | 420 | 39 |
| C ₃ H ₆ | O ₂ | H ₂ O | Ru/Al ₂ O ₃ | Dry impregnation | | | | 0.12 | 500 ppm N ₂ O, 1,000 ppm C ₃ H ₆ , 5% O ₂ , 10% H ₂ O, He balance | 450 | 39 |
| C ₃ H ₆ | | O ₂ | Pt/Al ₂ O ₃ -CeO ₂ -La ₂ O ₃ | Co-precipitation, impregnation | H ₂ /He, 400 °C, 1 h followed by He, 400 °C, 1h | 10,000 | | | 0.1% N ₂ O, 0.1% C ₃ H ₆ , 2% O ₂ , He balance | 454 | 38 |
| C ₃ H ₆ | | | Ru/Al ₂ O ₃ | Dry impregnation | | | | 0.12 | 500 ppm N ₂ O, 1,000 ppm C ₃ H ₆ , He balance | 485 | 39 |
| C ₃ H ₈ | O ₂ | | Fe/ZSM-5 | Solid state ion exchange | He, 500 °C | 7,500 | | | 1,000 ppm N ₂ O, 1,000 ppm C ₃ H ₈ , 4% O ₂ , He balance | 279 | 105 |
| CH ₄ | | | Fe-ZSM-5 | Ion exchange | O ₂ , 500 °C, 1 h | | | 9.9 | 950 ppm N ₂ O, 500 ppm CH ₄ , He balance | 290 – 395 | 104 |
| C ₃ H ₈ | | O ₂ , H ₂ O | Pd-Fe/ZSM-5 | Ion exchange, incipient wetness impregnation | N ₂ , 175 °C, 2 h | 20,000 | | | 1,900 ppm C ₃ H ₈ , 1,500 ppm N ₂ O, 100 ppm NO, 100 ppm NO ₂ , 0.5 % H ₂ O, 2.5 % O ₂ , N ₂ balance | 304 | 106 |



ARTICLE

Catalysis Science & Technology

| | | | | | | | | | | |
|-----------------------------------|----------------|-----------------------------------|---------------|--|---|--------|--|---|-----------|-----|
| C ₃ H ₈ | O ₂ | | Fe/silicalite | Isomorphous substitution, ion exchange, steam activation | N ₂ O/C ₃ H ₈ /O ₂ /He, 450 °C, 1 h | 11.3 | | N ₂ O (1.5 mbar), C ₃ H ₈ (1.5 mbar), He balance | 330 | 68 |
| C ₂ H ₆ | O ₂ | | Fe/ZSM-5 | Isomorphous substitution, ion exchange, steam activation | O ₂ /He, 450 °C, 1 h | 60,000 | | N ₂ O (1.5 mbar), C ₂ H ₆ (0.44 mbar), O ₂ (20 mbar), He balance | 332 | 107 |
| C ₃ H ₈ | O ₂ | H ₂ O | Fe/ZSM-5 | Solid state ion exchange | He, 500 °C | 7,500 | | 1,000 ppm N ₂ O, 1,000 ppm C ₃ H ₈ , 7% H ₂ O, 4% O ₂ , He balance | 332 | 105 |
| CH ₄ | O ₂ | | Fe/ZSM-5 | Isomorphous substitution, ion exchange, steam activation | O ₂ /He, 450 °C, 1 h | 60,000 | | N ₂ O (1.5 mbar), CH ₄ (0.93 mbar), O ₂ (20 mbar), He balance | 337 | 107 |
| CH ₄ | O ₂ | | Fe-ZSM-5 | Ion exchange | O ₂ , 500 °C, 1 h | 9.9 | | 950 ppm N ₂ O, 500 ppm CH ₄ , 10% O ₂ , He balance | 338 – 470 | 104 |
| CH ₄ | | | Fe-USY | Ion exchange | He, 600 °C, 1 h | 30,000 | | 5,000 ppm N ₂ O, 2,000 ppm CH ₄ , He balance | 344 | 72 |
| n-C ₁₀ H ₂₂ | O ₂ | | Fe-BEA | Ion exchange | 3% H ₂ /Ar, 13 mL·min ⁻¹ , ramp from 80 – 700 °C at 10 °C·min ⁻¹ | 35,000 | | 0.2% N ₂ O, 0.03% n-C ₁₀ H ₂₂ , 3% O ₂ , He balance | 346 – 377 | 67 |
| C ₂ H ₆ | O ₂ | NO | Fe/ZSM-5 | Isomorphous substitution, ion exchange, steam activation | O ₂ /He, 450 °C, 1 h | 60,000 | | N ₂ O (1.5 mbar), C ₂ H ₆ (0.44 mbar), NO (0.13 mbar), O ₂ (20 mbar), He balance | 347 | 107 |
| CH ₄ | | O ₂ , H ₂ O | Pd-Fe/ZSM-5 | Ion exchange, incipient wetness impregnation | N ₂ , 175 °C, 2 h | 20,000 | | 4,500 ppm CH ₄ , 1,500 ppm N ₂ O, 100 ppm NO, 100 ppm NO ₂ , 0.5 % H ₂ O, 2.5 % O ₂ , N ₂ balance | 351 | 106 |
| CH ₄ | | O ₂ | Fe-USY | Ion exchange | He, 600 °C, 1 h | 30,000 | | 5,000 ppm N ₂ O, 2,000 ppm CH ₄ , 50,000 ppm O ₂ , He balance | 352 | 72 |
| C ₃ H ₈ | O ₂ | | Fe/ZSM-5 | Isomorphous substitution, ion exchange, steam activation | N ₂ O/C ₃ H ₈ /O ₂ /He, 450 °C, 1 h | 11.3 | | N ₂ O (1.5 mbar), C ₃ H ₈ (1.5 mbar), He balance | 357 | 68 |
| C ₃ H ₈ | O ₂ | NO | Fe/ZSM-5 | Solid state ion exchange | He, 500 °C | 7,500 | | 1,000 ppm N ₂ O, 1,000 ppm C ₃ H ₈ , 1,000 ppm NO, 4% O ₂ , He balance | 357 | 105 |



Journal Name

Catalysis Science & Technology

| | | | | | | | | | | | |
|-------------------------------|----------------|------------------|------------------|--|--|--------|-----|--|--|-----------|-----|
| C ₃ H ₈ | O ₂ | | Fe/ZSM-5 | Isomorphous substitution, ion exchange, steam activation | N ₂ O/C ₃ H ₈ /O ₂ /He, 450 °C, 1 h | 60,000 | | | N ₂ O (1.5 mbar), O ₂ (50 mbar), C ₃ H ₈ (1.5 mbar), He balance | 357 | 108 |
| C ₃ H ₆ | O ₂ | | Fe-BEA | Ion exchange | 3% H ₂ /Ar, 13 mL·min ⁻¹ , ramp from 80 – 700 °C at 10 °C | 35,000 | | | 0.2% N ₂ O, 0.1% C ₃ H ₆ , 3% O ₂ , He balance | 369 – 392 | 67 |
| C ₃ H ₈ | O ₂ | NO | Fe/ZSM-5 | Isomorphous substitution, ion exchange, steam activation | N ₂ O/C ₃ H ₈ /O ₂ /NO/He, 450 °C, 1 h | 60,000 | | | N ₂ O (1.5 mbar), O ₂ (50 mbar), C ₃ H ₈ (1.5 mbar), NO (4.5 mbar), He balance | 384 | 108 |
| CH ₄ | | H ₂ O | Fe-USY | Ion exchange | He, 600 °C, 1 h | 30,000 | | | GHSV = 30,000 h ⁻¹ , 5,000 ppm N ₂ O, 2,000 ppm CH ₄ , 2% H ₂ O, He balance | 385 | 72 |
| C ₂ H ₆ | O ₂ | NH ₃ | Fe/ZSM-5 | Isomorphous substitution, ion exchange, steam activation | O ₂ /He, 450 °C, 1 h | 60,000 | | | N ₂ O (1.5 mbar), C ₂ H ₆ (0.44 mbar), NH ₃ (1.1 mbar of NH ₃), O ₂ (20 mbar), He balance | 388 | 107 |
| CH ₄ | | NO | Fe-USY | Ion exchange | He, 600 °C, 1 h | 30,000 | | | 5,000 ppm N ₂ O, 2,000 ppm CH ₄ , 700 ppm NO, He balance | 396 | 72 |
| CH ₄ | O ₂ | NH ₃ | Fe/ZSM-5 | Isomorphous substitution, ion exchange, steam activation | O ₂ /He, 450 °C, 1 h | 60,000 | | | N ₂ O (1.5 mbar), CH ₄ (0.93 mbar), NH ₃ (1.1 mbar of NH ₃), O ₂ (20 mbar), He balance | 397 | 107 |
| CH ₄ | O ₂ | NO | Fe/ZSM-5 | Isomorphous substitution, ion exchange, steam activation | O ₂ /He, 450 °C, 1 h | 60,000 | | | N ₂ O (1.5 mbar), CH ₄ (0.93 mbar), NO (0.13 mbar), O ₂ (20 mbar), He balance | 421 | 107 |
| NH ₃ | | | RuO ₂ | Bulk oxide | He, 400 °C, 1 h | | 5.5 | | N ₂ O (1.5 mbar), NH ₃ (1.5 mbar), He balance | 256 | 56 |
| NH ₃ | O ₂ | | RuO ₂ | Bulk oxide | He, 400 °C, 1 h | | 5.5 | | N ₂ O (1.5 mbar), NH ₃ (1.5 mbar), O ₂ (1.5 mbar), He balance | 345 | 56 |
| NH ₃ | | | Rh-FAU | Wet impregnation | Air, 500 °C | 30,000 | | | 0.2% N ₂ O, 0.2% NH ₃ , He balance | 272 | 75 |
| NH ₃ | O ₂ | | Fe-BEA | Ion exchange | | 50,000 | | | 1,000 ppm N ₂ O, 1,500 ppm NH ₃ , 8% O ₂ , Ar balance | 295 | 109 |
| NH ₃ | O ₂ | | Fe-ZSM-5 | Ion exchange | | 50,000 | | | 1,000 ppm N ₂ O, 1,500 ppm NH ₃ , 8% O ₂ , Ar balance | 310 | 109 |

ARTICLE

Catalysis Science & Technology

| | | | | | | | | | | | |
|-----------------|---------------------|--|-----------|--------------|---|---------|--|--|---|-----------|-----|
| NH ₃ | O ₂ , NO | | Fe-FER | Ion exchange | Air, 50 mL·min ⁻¹ , 550 °C, 2 h | 200,000 | | | N ₂ O/NO/O ₂ /NH ₃ /He = 0.1/0.15/3.0/0.25/96.5 | 327 | 64 |
| NH ₃ | | | Fe-MOR | Ion exchange | He, 600 °C, 1 h | 30,000 | | | 5,000 ppm N ₂ O, 4,000 ppm NH ₃ , He balance | 367 | 73 |
| NH ₃ | O ₂ | | Fe-MOR | Ion exchange | He, 600 °C, 1 h | 30,000 | | | 5,000 ppm N ₂ O, 4,000 ppm NH ₃ , 50,000 ppm O ₂ , He balance | 367 | 73 |
| NH ₃ | O ₂ | | Fe-MOR | Ion exchange | He, 600 °C, 1 h | 30,000 | | | 5,000 ppm N ₂ O, 4,000 ppm NH ₃ , 50,000 ppm O ₂ , He balance | 367 | 74 |
| NH ₃ | O ₂ | | Fe-FAU | Ion exchange | | 50,000 | | | 1,000 ppm N ₂ O, 1,500 ppm NH ₃ , 8% O ₂ , Ar balance | 370 | 109 |
| NH ₃ | | | Fe-MOR | Ion exchange | He, 600 °C, 1 h | 30,000 | | | 5,000 ppm N ₂ O, 4,000 ppm NH ₃ , He balance | 374 | 74 |
| NH ₃ | O ₂ | | Fe-BEA | Ion exchange | 3% H ₂ /Ar, 13 mL·min ⁻¹ , ramp from 80 – 700 °C at 10 °C·min ⁻¹ | 35,000 | | | 0.2% N ₂ O, 0.2% NH ₃ , 3% O ₂ | 374 – 397 | 67 |
| NH ₃ | H ₂ O | | Fe-BEA | Ion exchange | O ₂ /N ₂ , 500 °C, 1 h | 200,000 | | | 540 ppm N ₂ O, 360 ppm NH ₃ , 2.5% H ₂ O, N ₂ balance | 389 | 24 |
| NH ₃ | | | Fe-BEA | Ion exchange | He, 600 °C, 1 h | 30,000 | | | 5,000 ppm N ₂ O, 4,000 ppm NH ₃ , He balance | 397 | 73 |
| NH ₃ | O ₂ | | Fe-ZSM-5 | Ion exchange | He, 600 °C, 1 h | 30,000 | | | 5,000 ppm N ₂ O, 4,000 ppm NH ₃ , 50,000 ppm O ₂ , He balance | 397 | 73 |
| NH ₃ | O ₂ | | Fe-ZSM-35 | Ion exchange | | 50,000 | | | 1,000 ppm N ₂ O, 1,500 ppm NH ₃ , 8% O ₂ , Ar balance | 400 | 109 |
| NH ₃ | | | Fe-USY | Ion exchange | He, 600 °C, 1 h | 30,000 | | | 5,000 ppm N ₂ O, 4,000 ppm NH ₃ , He balance | 402 | 72 |
| NH ₃ | | | Fe-USY | Ion exchange | He, 600 °C, 1 h | 30,000 | | | 5,000 ppm N ₂ O, 4,000 ppm NH ₃ , He balance | 407 | 73 |
| NH ₃ | O ₂ | | Fe-BEA | Ion exchange | He, 600 °C, 1 h | 30,000 | | | 5,000 ppm N ₂ O, 4,000 ppm NH ₃ , 50,000 ppm O ₂ , He balance | 407 | 73 |
| NH ₃ | | | Fe-ZSM-5 | Ion exchange | He, 600 °C, 1 h | 30,000 | | | 5,000 ppm N ₂ O, 4,000 ppm NH ₃ , He balance | 417 | 73 |



Journal Name

Catalysis Science & Technology

| | | | | | | | | | | | |
|-----------------|------------------|----------------|--|--------------------------------|--|---------|-----|--|--|---------|-----|
| NH ₃ | O ₂ | | Fe-FER | Ion exchange | Air, 50 mL·min ⁻¹ , 550 °C, 2 h | 35,000 | | | N ₂ O/O ₂ /NH ₃ /He = 0.2/3.0/0.2/96.6 | 417 | 64 |
| NH ₃ | H ₂ O | O ₂ | Fe-BEA | Ion exchange | O ₂ /N ₂ , 500 °C, 1 h | 200,000 | | | 540 ppm N ₂ O, 360 ppm NH ₃ , 2.5% H ₂ O, 14% O ₂ , N ₂ balance | 426 | 24 |
| NH ₃ | H ₂ O | | Fe-SSZ-13 | Ion exchange | O ₂ /N ₂ , 500 °C, 1 h | 200,000 | | | 540 ppm N ₂ O, 360 ppm NH ₃ , 2.5% H ₂ O, N ₂ balance | 429 | 24 |
| NH ₃ | | O ₂ | Fe-USY | Ion exchange | He, 600 °C, 1 h | 30,000 | | | 5,000 ppm N ₂ O, 4,000 ppm NH ₃ , 50,000 ppm O ₂ , He balance | 430 | 72 |
| NH ₃ | O ₂ | | Fe-MCM-22 | Ion exchange | | 50,000 | | | 1,000 ppm N ₂ O, 1,500 ppm NH ₃ , 8% O ₂ , Ar balance | 435 | 109 |
| NH ₃ | O ₂ | | Fe-USY | Ion exchange | He, 600 °C, 1 h | 30,000 | | | 5,000 ppm N ₂ O, 4,000 ppm NH ₃ , 50,000 ppm O ₂ , He balance | 437 | 73 |
| NH ₃ | O ₂ | | Fe-SSZ-13 | Ion exchange | | 50,000 | | | 1,000 ppm N ₂ O, 1,500 ppm NH ₃ , 8% O ₂ , Ar balance | 450 | 109 |
| NH ₃ | H ₂ O | O ₂ | Fe-SSZ-13 | Ion exchange | O ₂ /N ₂ , 500 °C, 1 h | 200,000 | | | 540 ppm N ₂ O, 360 ppm NH ₃ , 2.5% H ₂ O, 14% O ₂ , N ₂ balance | 455 | 24 |
| NH ₃ | | O ₂ | Rh-FAU | Wet impregnation | Air, 500 °C | 30,000 | | | 0.2% N ₂ O, 0.2% NH ₃ , 3% O ₂ , He balance | 487 | 75 |
| H ₂ | | | Ni-Pt/SiO ₂ | Incipient wetness impregnation | H ₂ , 400 °C, 1 h | 25,000 | | | 1,250 ppm N ₂ O, 1,250 ppm H ₂ , He balance | 27 – 62 | 41 |
| H ₂ | | | Pt/SiO ₂ | Incipient wetness impregnation | H ₂ , 400 °C, 1 h | 25,000 | | | 1,250 ppm N ₂ O, 1,250 ppm H ₂ , He balance | 122 | 41 |
| H ₂ | | | Ni/SiO ₂ | Incipient wetness impregnation | H ₂ , 400 °C, 1 h | 25,000 | | | 1,250 ppm N ₂ O, 1,250 ppm H ₂ , He balance | 527 | 41 |
| H ₂ | | | Ti _{0.99} Pd _{0.01} O _{2-δ} | Solution combustion | | 43,000 | | | N ₂ O:H ₂ = 1:3 vol%, He balance | 52 | 110 |
| H ₂ | | | Ti _{0.99} Rh _{0.01} O _{2-δ} | Solution combustion | | 43,000 | | | N ₂ O:H ₂ = 1:3 vol%, He balance | 93 | 110 |
| H ₂ | | | Ti _{0.99} Pt _{0.01} O _{2-δ} | Solution combustion | | 43,000 | | | N ₂ O:H ₂ = 1:3 vol%, He balance | 107 | 110 |
| H ₂ | | | Ti _{0.99} Ru _{0.01} O _{2-δ} | Solution combustion | | 43,000 | | | N ₂ O:H ₂ = 1:3 vol%, He balance | 129 | 110 |
| H ₂ | | | RuO ₂ | Bulk oxide | He, 400 °C, 1 h | | 5.5 | | N ₂ O (1.5 mbar), H ₂ (1.5 mbar), He balance | 216 | 56 |



ARTICLE

Catalysis Science & Technology

| | | | | | | | | | | | |
|----------------|----------------|--|------------------|--------------|---|--------|-----|--|---|-----------|----|
| H ₂ | | | RuO ₂ | Bulk oxide | H ₂ /He, 400 °C, 1 h | | 5.5 | | N ₂ O (1.5 mbar), H ₂ (1.5 mbar), He balance | 305 | 56 |
| H ₂ | O ₂ | | RuO ₂ | Bulk oxide | He, 400 °C, 1 h | | 5.5 | | N ₂ O (1.5 mbar), H ₂ (1.5 mbar), O ₂ (1.5 mbar), He balance | 345 | 56 |
| H ₂ | O ₂ | | Fe-BEA | Ion exchange | 3% H ₂ /Ar, 13 mL·min ⁻¹ , ramp from 80 – 700 °C at 10 °C·min ⁻¹ | 35,000 | | | 0.2% N ₂ O, 0.2% H ₂ , 3% O ₂ | 497 – 504 | 67 |

* Other reactants – present in the feed but do not inhibit N₂O conversion

† Inhibitors – present in the feed and inhibit N₂O conversion



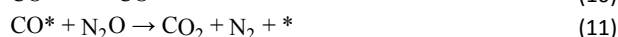
literature (i.e. the redox or associative routes) depending on the catalyst system.⁶⁰

In the redox mechanism, N₂O first adsorbs to the surface, releasing reduced N₂, and leaving O adsorbed (Eq. 6). This is then followed by either the Langmuir-Hinshelwood mechanism (Eqs. 7–8) or the Eley-Rideal mechanism (Eq. 9) to oxidize CO to CO₂. In the associative mechanism, simultaneous oxidation and reduction occurs by adsorbed CO (Eq. 10) reacting with either gaseous N₂O (Eq. 11) or adsorbed N₂O (Eqs. 12–13):

Redox Mechanism:



Associative Mechanism:



Delahay et al. studied a variety of reductants for the SCR of N₂O over two Fe-BEA catalysts in the presence of oxygen.⁶⁷ It was found that CO is an effective reductant with an onset temperature of ~200 °C for N₂O reduction, which is lower than other reductants like propene and ammonia. Based on the superimposed curves of N₂O reduction by CO and N₂O decomposition on the reduced Fe-BEA at below 330 °C, the reoxidation of Fe²⁺ to Fe³⁺ species by N₂O was suggested to be the rate limiting step in the CO-SCR of N₂O in the low temperature region. In a study of CO-SCR of N₂O over Fe-ZSM-5 and Fe-silicalite, Pérez-Ramírez et al. reported that the reaction rate has a linear correlation with the CO/N₂O feed ratio (up to 1:1) and depends strongly on the catalyst preparation method.⁶⁹ They found the preparation method affects the distribution of iron species on the catalyst surface as well as the interaction of CO with iron sites which in turn accelerate N₂O removal. A site-dependent reaction mechanism was proposed by using in situ UV/Vis and electron paramagnetic resonance (EPR) spectroscopy analyses. The authors concluded that while the reduction of N₂O by coordinated CO on Fe³⁺ ions can occur without changing oxidation states over isolated iron species, a redox Fe³⁺/Fe²⁺ cycle with the formation of intermediate oxygen anion-radicals (O•) happens over oligo-nuclear iron clusters. Wu et al. applied a multifaceted approach of experimental testing, catalyst characterization, and Density Functional Theory (DFT)/ab-initio molecular dynamics (AIMD) modeling to identify the catalytic role and transformation of different relevant iron species (mononuclear, binuclear, clusters, and Fe₂O₃ particles, see Fig. 7A) in Fe-ZSM-5 catalysts upon exposure to CO in the SCR of N₂O.¹¹¹ It was concluded that N₂O is activated on isolated iron sites to generate adsorbed oxygen species that then react with CO following the Eley-Rideal mechanism, while CO interacts with Fe₂O₃ particles to form

oxygen vacancies that dissociate N₂O following the Mars-van Krevelen mechanism (Fig. 7B). It is worth noting that the Mars-van Krevelen mechanism was also proposed in CO-SCR of N₂O on phosphotungstic acid supported single-atom catalysts.¹¹² In this case, CO reductant is oxidized by the oxygen atom from the support to form an oxygen vacancy, which is replenished by N₂O to release N₂ into gas phase. Recently, advanced in-situ/operando spectroscopy approach was utilized to study the reduction and oxidation half cycles of CO-SCR of N₂O over Fe-zeolites.^{113, 114} Qian et al. investigated the redox cycle of Fe-BEA catalyst during the CO-SCR of N₂O in an excess oxygen environment by operando/in situ diffuse reflectance ultraviolet-visible (UV-Vis) spectroscopy and in situ Fe K-edge X-ray absorption (XAS) spectroscopy.¹¹³ Based on the operando UV-Vis and XAS results, the redox cycle of Fe active sites was proposed in two steps: (i) Fe^{III}-α-O species are reduced by CO to generate Fe^{II} species and CO₂; (ii) Fe^{II} active sites reduce N₂O to form N₂ and regenerate Fe^{III}-α-O species. Quantitative spectrokinetic analysis revealed a higher reactivity of Fe^{II} sites with N₂O compared to O₂, enabling a selective CO+N₂O reaction under excess O₂ conditions. Fischer et al. examined the redox kinetics in the CO-SCR of N₂O over Fe-FER by combining modulation excitation with operando electron paramagnetic resonance (EPR) spectroscopy.¹¹⁴ They found that isolated Fe^{II} species in β-cationic positions are the only active sites during the reaction by enabling reversible Fe^{II}/Fe^{III} cycles, while isolated Fe^{II} sites in γ-cationic positions and oligomeric Fe species are spectator species.

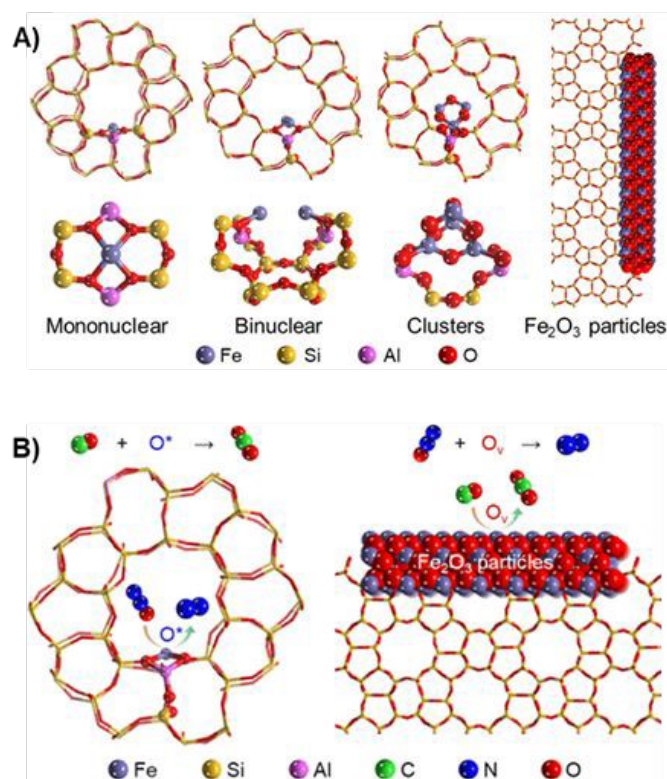


Fig. 7. (A) Schematic illustration of the different iron species in Fe-ZSM-5. (B) Proposed mechanisms of the SCR of N₂O by CO on isolated iron sites and Fe₂O₃



ARTICLE

particles. Reprinted from Ref. ¹¹¹ with permission from the American Chemical Society.

Single atom catalysts have attracted increasing attention in recent years due to their superior catalytic performance and efficient atomic utilization. Khan et al. examined the reduction of N₂O in the presence of CO over metal-free Si-coordinated phthalocyanine catalyst by DFT calculations.¹¹⁵ They found that the Si atom is energetically stabilized on the phthalocyanine support and can act as the active site for the N₂O dissociation. In another study, Ragab et al. employed DFT method to investigate aluminum-decorated C₂₄N₂₄ fullerene catalyst for the N₂O reduction in the presence of CO and O₂.¹¹⁶ This single-atom catalyst exhibited a relatively low energy barrier and strong N₂O binding, minimizing the potential inhibition by CO and O₂ due to the competitive adsorption.

The presence of other gas molecules in the feed such as NO, oxygen, and water, which are commonly found in the nitric acid production tail gas, can affect the CO-SCR of N₂O over Fe-zeolites. This is clearly shown by the shift of T₅₀ values with adding impurity gases to the feed stream on the same catalyst system (Table 2). N₂O decomposition can be assisted by addition of NO to facilitate oxygen desorption via adsorbed NO₂⁻ intermediates over oligo-nuclear iron species, however, CO-SCR of N₂O was inhibited by strong adsorption of NO on isolated iron sites in Fe-ZSM-5, especially at the low temperature regime.⁷⁰ This inhibitory effect of NO on CO-SCR of N₂O becomes less significant at high temperatures due to weaker adsorption of NO on iron active sites. Conversely, Wu et al. found that the addition of oxygen in the reactant feed showed an inhibitory effect on CO-SCR of N₂O over Fe-ZSM-5, which is attributed to the reaction between CO and O₂.¹¹¹ The presence of water exhibited a more negative effect than oxygen for this system.

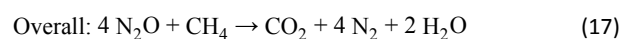
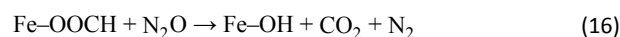
While iron supported on zeolites are the most common catalysts for CO-SCR of N₂O, a few studies were conducted on noble metals (i.e., Pt/Al₂O₃, Pd/Al₂O₃, or Rh/Al₂O₃) and mixed oxides (i.e., Co-Rh-Al-O, Co-Pd-Al-O, or Co-Pd-Ce-Al-O).^{60, 61, 117-119} Konsolakis et al. investigated rare earth oxide-modified Pt/Al₂O₃-CeO₂ and Pt/Al₂O₃-CeO₂-La₂O₃ structured catalysts (i.e. coated on ceramic honeycomb monoliths) in the absence and presence of excess oxygen and water.¹¹⁷ Like the Fe-zeolites, reducing agents such as CO significantly improve N₂O conversion by aiding in the removal of strongly adsorbed oxygen species. In addition, oxygen and water have a detrimental effect on N₂O conversion, which were attributed to competitive adsorption and irreversible changes in platinum oxidation state. In another study on the role of rare-earth oxides promoters, Holles et al. found that ceria improves CO-SCR of N₂O on Pd/Al₂O₃ and Rh/Al₂O₃ due to additional storage sites for dissociated oxygen atoms and high reducibility, while La₂O₃ hinders the reaction due to lower metal dispersion.¹¹⁹ The positive effect of adding CO as a reductant on the conversion of N₂O was reported for reactions over metal oxides (Co-Rh-Al, Co-Pd-Al, Co-Pd-Ce-Al) prepared by co-precipitation of

Catalysis Science & Technology

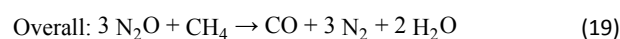
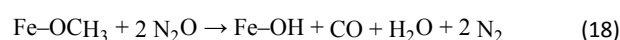
hydrocalcite-type precursors.⁵⁹⁻⁶¹ They found that the presence of oxygen inhibits N₂O conversion over metal oxides, and NO showed an insignificant influence.

3.2 Hydrocarbons (HC-SCR)

The presence of hydrocarbons in the SCR of N₂O over iron zeolites has been studied extensively in literature and applied in commercial NO_x-N₂O abatement processes.¹⁰⁷ Hydrocarbons are selective reductants and effective for the reduction of N₂O over Fe-BEA catalysts.⁶⁷ The reaction mechanism of N₂O reduction by C₃H₆ over noble metals supported on alumina and by C₃H₈ over Fe-zeolites was proposed to be related to the removal of adsorbed atomic oxygen species by these hydrocarbons to form CO and CO₂.^{39, 108} Deeper investigations on CH₄-SCR reaction mechanism combining infrared spectroscopy and catalytic reaction tests over Fe-ZSM-5 and Fe-BEA indicated an interaction of methane and N₂O molecules on iron hydroxyl groups with the sequential oxidation to methoxy and formate intermediate species (Eq. 14–17):^{72, 120, 121}



A minor amount of CO detected in product streams may indicate the presence of an additional pathway with incomplete oxidation of CH₄ (Eq. 14, 18–19):^{72, 120, 121}



Hevia et al. studied light hydrocarbons (C₁-C₃) with different degrees of unsaturation and proposed a set of criteria to optimally select hydrocarbons for SCR of N₂O over Fe-ZSM-5 zeolites, including N₂O reduction activity and operation temperature, hydrocarbon utilization or the selectivity to react with N₂O in O₂ excess, CO and CO₂ formation, sensitivity to NO and NH₃, and cost.¹⁰⁷ It was found that ethane and methane are the most effective reductants, while alkenes and alkynes require a higher temperature to consume O* and are less effective due to undesired non-selective reaction with oxygen. Nobukawa et al. similarly investigated the SCR of N₂O on Fe-ZSM-5 and found that methane is a more efficient reductant compared to higher alkanes (ethane and propane), hydrogen, and CO.¹⁰⁴ H₂-TPR and extended X-ray absorption fine structure analyses were performed to show that the high N₂O reduction activity at high Fe/Al ratio in Fe-ZSM-5 catalysts is likely due to the presence of binuclear iron species. In addition, the redox cycle of these active iron sites is promoted by the formation of methoxy species, which originated from the interaction of methane with N₂O-derived adsorbed oxygen. Conversely, Van den Brink et al. reported that propane is more active than methane in the SCR of N₂O over palladium-promoted Fe-ZSM-5 in the same temperature range of 200–500 °C.¹⁰⁶ The presence of water in the feed stream was found to be detrimental to the



catalytic performance of N₂O reduction by propane over Fe-ZSM-5 catalysts.^{105, 106} A more significant inhibitory effect of NO on the reduction of N₂O by hydrocarbons was observed over different iron zeolite frameworks (Fe-ZSM-5, Fe-BEA, Fe-USY), which was ascribed to the competitive adsorption for iron active sites.^{72, 105, 108} In addition to water and NO, oxygen also exhibited an adverse effect on the HC-SCR of N₂O, which was mainly attributed to competitive adsorption and non-selective oxidation of hydrocarbon intermediates to form CO.⁷² As a result, they proposed that N₂O conversion in a mixed N₂O, CH₄, NO stream can be a combination of three pathways: CH₄-SCR, CO-SCR, and NO-assisted direct decomposition.

Regarding the catalytic iron species, Pérez-Ramírez et al. proposed that isolated extra-framework iron sites play an important role in the reduction of N₂O by propane,¹⁰⁸ which was further verified by comparing steam-activated samples of Fe-silicalite and Fe-ZSM-5.⁶⁸ By employing UV-Vis diffuse reflectance spectroscopy (DRS), it was revealed that isolated iron species dominate, steam-activated Fe/silicalite gave higher activity over the steam-activated Fe/ZSM-5 containing iron clustered species. However, the presence of iron clusters may be beneficial for the direct N₂O decomposition, as oxygen recombination is the rate limiting step. In addition, this comparison of Fe-silicalite and Fe-ZSM-5 implies a minor role of acid sites in the hydrocarbon-assisted reduction of N₂O. Another study by Debbagh et al. reported that the reduction of N₂O by methane and CO over Fe-ZSM-5 follows different reaction mechanisms over different iron sites.⁷¹ Specifically, while CO is active over isolated iron species, the reduction of N₂O by hydrocarbons such as CH₄ and C₃H₈ happens more favorably over oligo-nuclear iron-oxo clusters.

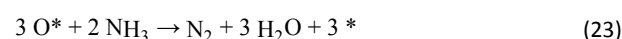
Recently, in situ characterization and operando studies have provided insights into the active sites and reaction mechanism of the CH₄-SCR of N₂O over zeolite-based catalysts.¹²²⁻¹²⁵ Campa et al. investigated N₂O reduction with CH₄ on metal-free H-NaMOR catalysts in the absence and presence of oxygen using in situ and operando FTIR methods.¹²² It was suggested that N₂O and CH₄ are synergistically activated on dehydrated Si-OH-Al pairs as main active sites. In addition, formaldehyde-like species are possible reaction intermediates during the CH₄-SCR of N₂O. This observation is consistent with the other studies on Fe-MOR, Fe-FER, Co-MOR, and Ni-MOR catalysts that employed in situ UV-Vis DRS and operando FTIR experiments.^{123, 125} The catalytic performance of Fe-MOR and Fe-FER catalysts were attributed to the stabilization of Fe^{II} species and bifunctional active sites, which consist of Fe^{III}-oxo species and nearby reactive OH species, in these zeolite frameworks.¹²³ In another study on CH₄-SCR of N₂O on Fe-BEA with operando IR and in situ XAFS-DRIFTS, Liu et al. found that both NO and NH₃ inhibit the reduction of N₂O due to their strong adsorption on Fe^{II} active sites and rapid reaction with Fe^{III}-OH and α-oxygen.¹²⁴

In addition to Fe-zeolites, Rh/Al₂O₃, Ru/Al₂O₃, and Pd/Al₂O₃ have been studied for the HC-SCR of N₂O.^{39, 40} Christoforou et al. investigated Rh, Ru, Pd, Co, Cu, Fe, and In with various

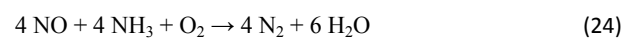
catalyst supports (Al₂O₃, SiO₂, TiO₂, ZrO₂, calcined hydrotalcite MgAl₂(OH)₈·H₂O) and found that Rh/Al₂O₃ and Ru/Al₂O₃ are the most active catalysts for HC-SCR of N₂O in the presence of excess O₂.³⁹ However, propene was found to facilitate N₂O reduction over Rh/Al₂O₃ by scavenging N₂O-derived O, helping maintain catalytically available Rh sites. Propene was found to potentially alter the redox state of active metal sites, lowering and inhibiting catalytic performance on Ru/Al₂O₃ as it reduces Ru³⁺/Ru⁴⁺ sites that are active for N₂O decomposition. The presence of oxygen in the feed stream also hinders N₂O reduction over Rh/Al₂O₃ but alleviates the inhibition of propene over Ru/Al₂O₃, as O₂ oxidizes propene into CO and CO₂. Water was suggested to inhibit C₃H₆-SCR of N₂O in the presence of O₂ by competitive adsorption with N₂O and potentially the formation of Ru oxyhydroxides that alter electronic structure of active RuO₂ active sites. On the contrary, the presence of SO₂ impedes N₂O reduction by the formation of sulfate species, consistent with the findings of Konsolakis et al. for CH₄-SCR of N₂O over Pd/Al₂O₃.⁴⁰ It was noted that water effects were reversible, whereas SO₂ deactivation was irreversible.

3.3 Ammonia (NH₃-SCR)

Ammonia is another potential reductant for the SCR of N₂O over different catalysts such as metal-zeolites and metal oxides.^{56, 67, 126-128} Mauvezin et al. evaluated the decomposition and reduction of N₂O by ammonia over several metals supported on FAU zeolite, including Rh, Ru, Pd, Co, Cu, Ni, and Fe.⁷⁵ It appeared that Fe-FAU was the most efficient catalyst for NH₃-SCR of N₂O in the presence of oxygen. In terms of reaction mechanism of NH₃-SCR of N₂O over Fe-zeolites, it was suggested that the addition of ammonia assists the decomposition of N₂O by removing the surface oxygen species (Eq. 23 of Eq. 20–23).⁶⁴



Zhang et al. proposed a more detailed reaction pathway and mechanism of NH₃-SCR of N₂O over Fe-MOR and Fe-BEA catalysts related to the redox cycle of Fe³⁺-OH/Fe²⁺-OH sites through -NH₂ and NO intermediates.⁷⁴ Multiple temperature programmed experimental techniques and FT-IR of N₂O/NH₃ interaction were employed. It was found that the rate-limiting step over Fe-MOR is reduction of Fe³⁺-OH by ammonia into Fe²⁺-OH and N≡N bond breaking was the main N₂O splitting mechanism. Similarly, N₂O oxidation of Fe²⁺-OH was the rate-determining step for Fe-BEA with N-O bond breaking being the main N₂O splitting mechanism. The next reaction steps of nitric oxide in the presence of oxygen follow the typical SCR mechanism to form nitrogen and water (Eq. 24).



The high activity of Fe-MOR was ascribed to the pore structure of MOR zeolites and the high iron loading, which enable the



ARTICLE

genesis of proximal Fe³⁺ ions or Fe^{3+...Fe³⁺} pairs as the active sites for the N≡NO splitting.

The zeolite structure strongly influences the distribution of iron species, which plays an important role in catalytic activity of Fe-zeolites for the N₂O decomposition and reduction by ammonia.⁶⁴ Wang et al. studied the nature of iron species by UV-vis, Mössbauer, and EPR spectroscopies, as well as H₂-TPR, and kinetic measurements.²⁴ It was found that isolated and binuclear Fe sites are present in Fe/SSZ-13, whereas Fe/BEA contains mostly oligomeric Fe_xO_y species and exhibited a higher NH₃-SCR activity compared to Fe/SSZ-13. This indicates that larger site ensembles, such as oligo-nuclear iron-oxo clusters, are the main active sites of the NH₃-SCR of N₂O instead of isolated iron species. A similar finding about the catalytic effect of zeolite structure on Fe-zeolites has been reported by Du et al.¹⁰⁹ The NH₃-SCR of N₂O activity followed the order: Fe-BEA > Fe-ZSM-5 > Fe-FAU > Fe-ZSM-35 > Fe-MCM-22 > Fe-SSZ-13. UV-Vis DRS, XPS, and H₂-TPR analyses verified that Fe³⁺ sites are more favorably located inside straight-channel zeolite pores compared to cage-type zeolites, leading to the high activity observed in Fe-BEA and Fe-ZSM-5. In addition, Fe-zeolites with larger pore sizes facilitate the internal diffusion of N₂O inside zeolite channels, thereby improving the catalytic reduction of N₂O by ammonia. Zhang et al. performed H₂-TPR, UV-Vis DRS, and NH₃/O₂-TPD to analyze the nature and distribution of iron species, including isolated Fe³⁺, oligo-nuclear Fe^{3+_xO_y} clusters, and Fe₂O₃ nanoparticles on external surface.⁷³ It was also determined that larger zeolite channels contain more exchanged Fe ions, which explains higher Fe loadings in Fe-MOR and Fe-USY compared to Fe-BEA and Fe-ZSM-5. Interestingly, it was suggested that isolated Fe³⁺ ions are active species for the reduction of N₂O, while the Fe^{3+_xO_y} clusters are less active due to strong ammonia adsorption on Brønsted acid sites formed on the bridge oxide ions in binuclear iron species. On the other hand, operando electron paramagnetic resonance measurements were performed by Fischer et al. to elucidate the active sites and kinetically relevant reaction steps during N₂O decomposition and reduction over Fe-SSZ-13 with different reductants, including CH₄, NH₃, and H₂.¹²⁹ They found that isolated Fe²⁺ species in axial coordination are the main active sites for direct N₂O decomposition, while Fe_xO_y clusters and Fe²⁺ sites in distorted geometries are responsible for N₂O reduction in the presence of reductants.

Regarding the effect of other gases in the feed, it was reported that oxygen showed an inhibitory effect on NH₃-SCR of N₂O over Fe-MFI, Fe-FAU, Fe-BEA, and Fe-SSZ-13, likely due to the non-selective oxidation of ammonia.^{24, 75, 127} However, the presence of oxygen had no significant influence on N₂O conversion over Fe-MOR whereas NH₃-SCR of N₂O outperformed ammonia oxidation.^{73, 74} While the influence of NO on N₂O reduction by NH₃ over Fe-MOR was negligible,⁷³ the reduction of N₂O by NH₃ over Fe-FER and Fe-BEA was promoted by NO, due to the fast surface reaction between adsorbed O* and NO* species.⁶⁴ On the contrary, Zhuang et al. found that a small fraction of NO (100 ppm) in the feed stream can inhibit the NH₃-SCR of N₂O

over Pd/Al₂O₃ catalyst.¹³⁰ Interestingly, by modifying the Al₂O₃ support to create oxygen vacancies containing free electrons, the Pd-based catalyst exhibited superior performance in the low temperature regime below 300 °C, along with desirable NO inhibition resistance. Baek et al. studied the effect of water on the NH₃-SCR of N₂O over Fe-BEA using DRIFTS and self-consistent-charge density-functional-tight-binding calculations.¹³¹ It was found that the presence of water vapor increases hydroxyl groups on the Fe-BEA surface. Instead of the conventional explanation, where the presence of water vapor leads to competitive adsorption, the authors attributed decreased N₂O conversion to surface hydroxyl groups that induce stronger adsorption of N₂O.

3.4 Hydrogen (H₂-SCR)

The research on N₂O reduction by hydrogen is limited (mainly reported with noble metal catalysts).^{41, 110} Hydrogen is not a selective reductant in the SCR of N₂O over Fe-BEA and RuO₂ catalysts, as it favorably reacts with oxygen present in the reactant feed.^{56, 67} Santiago et al. employed a combination of steady-state reaction tests at ambient pressure, transient reaction studies in the Temporal Analysis of Products (TAP) reactor (see section 4.1), and DFT simulations to unravel the mechanism of decomposition and reduction of N₂O by hydrogen or ammonia on RuO₂.⁵⁶ It was found that hydrogen facilitates the reduction of the catalyst surface to form highly active oxygen vacancies, and it appears to be a more effective reductant compared to ammonia in this catalytic system, as ammonia-derived intermediates strongly adsorb on RuO₂ surface and block active sites for N₂O conversion. Arenas-Alatorre et al. studied N₂O decomposition and reduction by H₂ over Pt/SiO₂, Ni/SiO₂, and NiPt/SiO₂ catalysts, which showed much lower T₅₀ values compared to other catalyst systems (Table 2).⁴¹ It was found that the addition of H₂ improves N₂O conversion over studied monometallic and bimetallic catalysts. Bimetallic (6–8 nm NiPt) catalysts exhibited a higher activity compared to Pt/SiO₂ and Ni/SiO₂ catalysts in the H₂-SCR of N₂O, which was ascribed to the geometric and electronic effects of alloying. Another study of N₂O reduction by H₂ on noble metal substituted TiO₂ catalysts (Ti_{0.99}M_{0.01}O_{2-δ}, where M=Ru, Rh, Pd, Pt) also reported significantly low T₅₀ values (Table 2), notably for Pd-substituted TiO₂. The authors attributed the high activity to a bi-functional pathway: N₂O dissociation at oxide-ion vacancies and rapid H₂ activation on substituted metal ions that scavenge O* to produce H₂O; this mechanism was supported by H₂-TPR/uptake trends and kinetic modeling.¹¹⁰ The reduction of N₂O by H₂ was also studied on various polyoxometalate-supported single-atom catalysts M₁/PTA (M = Fe, Co, Mn, Ru, Rh, Os, Ir, and Pt; PTA = [PW₁₂O₄₀]³⁻) by DFT.¹³² Os₁/PTA SAC exhibited high activity with a low rate-limiting energy barrier, which was attributed to a strong charge-transfer cooperative effect of metal and support along the favorable reaction pathways. The Os atom and PTA support acts as electron reservoirs, effectively modulating the adsorption/desorption and bond-breaking steps.



The comparison of different reductants for the SCR of N_2O is summarized in Table 3. The usage of CO and NH_3 can be cost-effective when available as a byproduct gas in industrial plants or when coupled with existing SCR systems. Methane is a low-value hydrocarbon and the major component of the natural gas stream, enabling economical use in the SCR of N_2O . On the other hand, the industrial application of hydrogen is still limited due to the high costs associated with hydrogen production, transportation, and storage.

Table 3: Comparison of different reductants for the SCR of N_2O

| Reductants | Common catalysts | Estimated cost (catalyst, reductant) | By-products | Potential application |
|------------|------------------|--------------------------------------|---------------------|---------------------------------|
| CO | Fe-zeolites | Low | CO_2 | power plant flue gas |
| CH_4 | Fe-zeolites | Low | CO, CO_2 , H_2O | nitric acid production tail gas |
| NH_3 | Fe-zeolites | Low | NO, N_2 , H_2O | ammonia-fueled engine exhaust |
| H_2 | Noble metals | High | H_2O | low-temperature constraints |

3.5 Catalyst Durability and Exotic Reductants for SCR

The research on the catalyst durability in the selective catalytic reduction of N_2O remains limited. Zhang et al. reported that the catalytic activity of Fe-MOR for NH_3 -SCR of N_2O remains almost unchanged for more than 100 hours under simulated nitric acid plant conditions at 427 °C with the presence of oxygen and water vapor in the feed stream.¹³³ It is worth noting that Fe-zeolites, which are the most common catalyst for the SCR of nitrous oxide, have also been studied extensively for the NH_3 -SCR of nitric oxide, particularly in relation to treatment processes of exhaust gases from diesel engines, coal-fired plants, and industrial boilers.¹³⁴ The catalyst durability of Fe-zeolites in the NH_3 -SCR of NO is significantly affected by sulfur and phosphorus poisoning, as well as their hydrothermal stability at elevated temperatures, which constrains their practical applications.¹³⁵

In SCR reactors, other more exotic reductants may also play a key role in future N_2O abatement technologies. In addition to the CO, hydrocarbons, NH_3 , and H_2 methods discussed previously, other reducing agents can be considered and new technologies envisioned. Expanding on carbonaceous reductants like CO and hydrocarbons, solid carbon species like coke, charcoal, and biochar could also be used. Wang et al. investigated the reduction of N_2O by biomass char with the presence of CO and O_2 in a fixed bed reactor system.¹³⁶ While biomass char and CO facilitated the reduction of N_2O by lowering both the onset temperature and the apparent activation energy, an inhibitory effect was observed with O_2 . The solid carbon materials could also play a role as a catalytic surface as was observed by Wei et al., who studied activated

coke catalysts for SCR of NO.¹³⁷ Similarly, Wang et al. looked at the effect of cost effective and high surface area activated carbon at 200–300 °C in a 1000 ppm NO in N_2 gas stream.¹³⁸ They saw detection of CO and reduced NO after the reactor, indicating the carbon had reduced NO to N_2 . As noted previously, the produced CO can further reduce other NO_x species. While neither group tested N_2O abatement, their results suggest a need for further study.

While ammonia is the most common reductant for SCR, other nitrogen species could also serve as reductants for N_2O . Urea is used in diesel exhaust fluid to mitigate NO_x , which thermally decomposes releasing ammonia for the standard NH_3 -SCR mechanism.¹³⁹ While nitrogen in the –3 oxidation state (e.g. ammonia and urea) has the most electrons to contribute to N_2O reduction, nitrogen species in the –2 (e.g. hydrazine) and –1 oxidation states (e.g. hydroxylamine) could also be used. In one instance, Zheng et al. developed a kinetic model for NO removal by hydrazine, that could be similarly applied to N_2O .¹⁴⁰

SO_x and NO_x are often emitted together from industrial processes but are typically removed individually using flue gas desulfurization followed by SCR.¹⁴¹ Merging these processes has been explored through simultaneous catalytic desulfurization and denitrification (SCDD). Hydrogen sulfide has been used as a reductant in SCDD. Developing this technology, Lü et al. were able to achieve conversion rates of 75% for SO_2 and 90% for NO in the same reactor at 280 °C.¹⁴² Separately, Yang et al. found that a sulfide-driven autotrophic denitrification step reduced N_2O emissions during a wastewater treatment system known as sulfate reduction-autotrophic denitrification-nitrification integrated process.¹⁴³ This process combined elements of the sulfur- and nitrogen-cycles, reducing nitrate ions in solution to nitrogen gas while oxidizing sulfide ions to sulfate/sulfite ions and elemental sulfur. The N_2O reduction rate scaled linearly with sulfide concentration at pH 7. While quite dissimilar to gas phase SCR, it highlights the principles of incorporating sulfide as a reductant for N_2O abatement.

4 Mechanistic Investigation of Nitrous Oxide Abatement

4.1 Temporal Analysis of Products (TAP) Experiments

Fundamental understanding of reaction mechanisms and the nature of active sites are important to advance catalyst development for efficient chemical processing. Most of the experimental approaches on studying direct decomposition and SCR of N_2O are based on light-off curve measurements (i.e. tracking reactant conversion as a function of temperature). Transient kinetic studies of heterogeneous-catalyzed gas phase reactions in TAP reactors can be effectively utilized to obtain kinetic parameters (e.g., rate constants of simple reaction steps, lifetime of reactive surface species, etc.) based on the time-dependent interactions between gas molecules and the catalyst surface, and offer deeper mechanistic insights into simple



reaction steps (Fig. 8A). A more detailed description of the TAP reactor and experiments were reported elsewhere.¹⁴⁴⁻¹⁴⁷

reactions with Fe-based catalysts.^{71, 147} Kondratenko and Pérez-Ramírez studied direct decomposition of N_2O in a TAP reactor and found that the direct decomposition of N_2O over steam-activated Fe-silicalite occurs on free, isolated iron species and iron sites associated with adsorbed mono-atomic oxygen species ($*-O$) at 500–575 °C.¹⁴⁹ They found that O_2 forms via decomposition of a bi-atomic oxygen species ($*-O_2$) adsorbed over the iron site. This species is derived from $O-*O$, which is formed via interaction of N_2O with the iron site associated with ($*-O$). The recombination of $*-O$ species or direct formation N_2O and $*-O$ (Eley-Rideal) mechanisms were excluded. This N_2O decomposition pathway over Fe-silicalite was also applicable to Fe-ZSM-5, which has markedly different iron speciation including both isolated and oligomeric iron-oxo species, as well as small Fe_2O_3 nanoparticles, indicating the generality of the reaction mechanism.¹⁵⁰ In addition, the kinetic parameters of N_2O decomposition, such as turnover frequency of N_2 formation, rate constant and activation energy of elementary steps, were calculated from a TAP-derived kinetic model for the comparison between Fe-ZSM-5 and Fe-silicalite. The relative activities of these catalysts in the TAP experiment were found to be consistent with the steady-state performance. On the other hand, it was suggested that the oxygen is formed directly via the reaction of gas-phase N_2O with adsorbed mono-atomic oxygen species originating from the decomposition of adsorbed N_2O on Rh-ZSM-5 catalyst.¹⁵¹ The higher catalytic activity of Rh-ZSM-5 compared to Fe-ZSM-5 was attributed to the stronger N_2O adsorption and faster oxygen formation to regenerate free active sites over rhodium sites.

The N_2O decomposition reaction mechanism at high temperature regime (550–700 °C) over $BaFeAl_{11}O_{19}$ hexaaluminate was investigated in the TAP reactor and compared with lower temperature regime (400–500 °C) over Fe-ZSM-5 zeolites.^{56, 152} Regardless of the catalyst support (hexaaluminate or ZSM-5), it was indicated that N_2O decomposition activity is more favorable over clustered iron species ($Fe-O_x$) than isolated iron sites. Large iron oxide particles were detrimental to activity, thus there is an optimum in clustering of iron species. Regardless of the catalyst support optimum in clustering. The NO-promoted N_2O decomposition over Fe-zeolites was investigated by multitrack experiments in a TAP-reactor-like high-vacuum reactor system.¹⁵³ The addition of nitric oxide benefits N_2O decomposition by removal of adsorbed oxygen atoms and facilitating migration and recombination of these atomic oxygen species on catalyst surface. Mechanistic studies of N_2O decomposition by transient kinetic methods were also performed over other materials such as Na-doped CaO, Pt gauze, and Pt-Rh gauze.¹⁵⁴⁻¹⁵⁶ It is noted that the formation of gas-phase oxygen by recombination of two adsorbed oxygen atoms on surface Pt sites was less favorable under transient vacuum conditions as compared to ambient pressure steady-state conditions, which was ascribed to a low surface coverage of these atomic oxygen species in high-vacuum TAP reactor.¹⁵⁷ This observation further underscores the impact of surface coverage under relevant reaction conditions on the underlying mechanisms, which is of

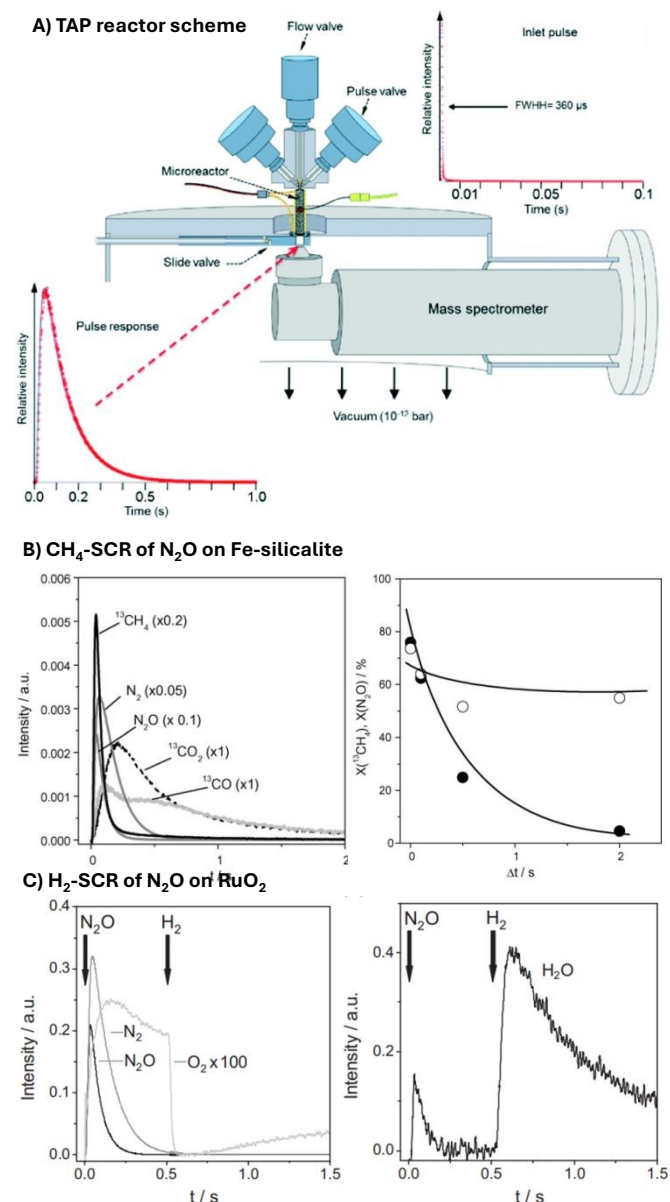


Fig. 8. (A) Schematic of a TAP reactor. Reprinted from Ref. ¹⁴⁷ under CC BY 3.0 license. (B) Transient responses of N_2O , $^{13}CH_4$, N_2 , ^{13}CO , and $^{13}CO_2$ upon simultaneous pulsing of N_2O and $^{13}CH_4$ and conversion of $^{13}CH_4$ (●) and N_2O (○) as a function of the time delay (Δt) between the pulses of N_2O and $^{13}CH_4$ over Fe-silicalite at 450 °C (723 K). Reprinted from Ref. ¹⁴⁸ with permission from Elsevier. (C) Transient responses of N_2O , N_2 , O_2 , and H_2O in pump-probe experiments of $N_2O:Ar = 1:1$ and $H_2:Xe = 1:1$ at 250 °C (523 K) with a time delay of 0.5 s between the pulsed mixtures. Reprinted from Ref. ⁵⁶ with permission from Elsevier.

As mentioned in Section 2 and 3, the reaction mechanism of direct decomposition and SCR of N_2O depend on the nature and distribution of active sites, leading to distinct catalyst performance. These correlations have been investigated on common N_2O abatement catalyst systems, including noble metals, metal oxides, and zeolites, in TAP reactors. Several studies have performed pulse response experiments to understand the mechanism and kinetics of N_2O abatement



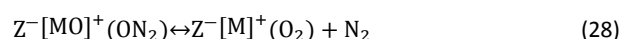
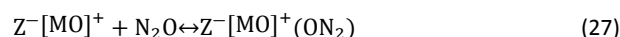
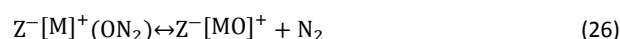
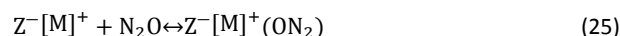
critical importance when extrapolating TAP-derived models to steady-state experiments. The reduction of N₂O over Fe-zeolites using CO, methane, and propane as reductants, was investigated by pump/probe pulse response experiments the TAP reactor (Fig. 8B).^{56, 148, 156, 158, 159} Varying the time delay, Δt, between the N₂O and hydrocarbon pulse on Fe-silicalite shows that the reactive oxygen generated from N₂O on extra-framework Fe sites has a short lifetime, as evidenced by the decline in hydrocarbon conversion with increasing time delay.¹⁵⁶ The finding on the short lifetime of highly reactive oxygen species formed upon interaction of N₂O on extra-framework iron sites was consistent for both methane and propane, with the latter being a more effective reductant for N₂O reduction under both high vacuum TAP conditions and ambient pressure flow experiments.^{148, 159} Santiago *et al.* also used the pump/probe format pulsing N₂O followed by ammonia and hydrogen reductants over a RuO₂ catalyst. The time delay was fixed at 0.5 s, and as shown in Fig. 8C, the H₂ pulse suppresses the O₂ response from N₂O and increases yield of H₂O, indicating that N₂O-derived surface oxygen remains reactive over the 0.5 s window and is readily scavenged by H₂.⁵⁶ In addition, the promotion effect of H₂ and NH₃ on the N₂O reduction is diminished in the presence of oxygen due to non-selective oxidation reactions of these reductants.

4.2 Density Functional Theory (DFT) Modeling

DFT enables atomic-level insight into catalytic mechanisms and electronic structure information, enabling it to be used both as an explanatory tool for the performance of a catalyst, and as a screening tool for catalyst discovery. The energy at each elementary reaction step, the activation energy between steps, and the energies of proposed catalytic intermediaries can be directly calculated. From these energetics, the active site(s), rate limiting step, and energetically favorable pathway can be determined. Additionally, DFT provides electronic structure information, notably the d-band center, Bader (partial) charge, charge density, and electronic density of states to rationalize catalytic performance. A more extensive treatment of DFT for catalysis and the background of methods can be found in literature.¹⁶⁰⁻¹⁶² It has been utilized for studies of supported metal, mixed oxide, and zeolite catalysts in both the direct decomposition and the SCR of N₂O

Mechanistic studies with DFT for direct decomposition of N₂O have helped determine active sites, activation barriers, the role of promoters, and provided an electronic structure explanation. Kim *et al.* computationally studied the decomposition of N₂O on Pd_xCu_y compositions.¹⁶³ It was found that Pd adsorbs N₂O onto the metal surface stronger than Cu, while Cu more easily dissociates N₂O than Pd. Intermediate Pd_xCu_y compositions were found to have a balance of these traits leading to improved activity. The PdCu catalyst had only a slight reduction in N₂O adsorption strength vs. pure Pd (−38.58 vs. −42.45 kJ/mol), and a lower N₂O dissociation activation energy (8.70 vs. 24.14 kJ/mol). Electronic structure analysis found that the PdCu alloy had a higher d-band center position (−1.64 eV) vs. pure Pd

(−1.67 eV) or Cu (−2.29 eV), which may enable higher catalytic activity. The Pd₃Cu alloy had the weakest O adsorption and highest predicted decomposition activity, which matches the experimental observations reported in literature.³² Sun *et al.* conducted DFT calculations for alkaline-earth-modified metal oxide catalysts (A_{0.5}Co_{2.5}O₄ with A = Mg, Ca, Sr, Ba) in tandem with experiments for direct N₂O decomposition.¹⁶⁴ Ba was found to significantly lower the oxygen vacancy formation energy vs. the unmodified Co₃O₄ oxide (261.46 vs. 172.71 kJ/mol) for the near O site. The lower oxygen vacancy formation energy of Ba_{0.5}Co_{2.5}O₄ was attributed to the lower valency of Ba compared to Co. The oxygen vacancies in the oxide allowed the catalyst to chemisorb more O, which enables the reduction of N₂O, resulting in a 73 °C reduction in the T₉₀ temperature for Ba_{0.5}Co_{2.5}O₄ vs. Co₃O₄. Wang *et al.* utilized DFT to investigate both the oxygen vacancy formation energy and the N₂O decomposition activation energy over oxygen vacancies and metal sites in CeO₂ and Co-doped CeO₂.¹⁶⁵ The doping of Co at a Co/Ce ratio of 1 was found to reduce the oxygen vacancy formation energy from 219.99 to −29.91 kJ/mol. Additionally, the activation energy over both the metal sites (224.81 versus 311.65 kJ/mol) and oxygen vacancies (111.92 versus 284.63 kJ/mol) were lower for the Co-doped CeO₂, indicating the oxygen vacancies serve as active sites for the direct decomposition of N₂O. Heyden *et al.* performed a comprehensive DFT study of the energetics and kinetics of direct N₂O decomposition on the hydrated and dehydrated mononuclear Fe sites in a Fe-ZSM-5 zeolite catalysts to determine the active sites, method of low concentration H₂O deactivation, and rate constants.¹⁶⁶ The decomposition was modeled following the E-R-like mechanism shown in Eq. 25–29 (M = Fe mononuclear site, Z = zeolite site):



The Z-[Fe]⁺ and Z-[FeO]⁺ had exothermic enthalpies of adsorption for N₂O; however, the oxidation of bare Z-[Fe]⁺ by N₂O is very exothermic (−259.5 kJ/mol or −2.69 eV), making the reverse reaction unlikely to occur during N₂O decomposition, making Z-[FeO]⁺ the active site. After determining Z-[FeO]⁺ was the active site, H₂O adsorption and potential catalyst deactivation were evaluated. H₂O adsorbs without barriers to Z-[FeO]⁺, forming Z-[Fe(OH)₂]⁺, which has a higher activation energy for N₂O decomposition. The formation of Z-[Fe(OH)₂]⁺ sites resulted in a more than doubling of the activation energy from (106.7–229.3 kJ/mol) as water content increased from 0 to 100 ppb.

SCR of N₂O with a variety of reductant agents has also been studied using DFT.^{111, 167} The reaction pathways on isolated iron sites and Fe₂O₃ particles on a Fe/ZSM-5 catalyst for CO-SCR previously discussed in section 3.1 and superior performance of



the CO-SCR versus direct decomposition were supported by DFT calculations.¹¹¹ DFT simulations showed the pristine Fe₂O₃ is unable to adsorb N₂O initially and required an oxygen vacancy for N₂O adsorption to occur. With the oxygen vacancy being formed by CO oxidation the CO-SCR follows the MvK mechanism. On the isolated iron sites CO was unable to adsorb, causing initial N₂O adsorption and release of N₂, followed by CO bonding with O* forming CO₂ for subsequent desorption, thus following the E-R reaction mechanism. For both the isolated Fe site and the on Fe₂O₃ the desorption of CO₂, a product of CO-SCR, had a far lower activation energy than that of O₂, a product of direct N₂O decomposition, explaining the improved low temperature regime (300 – 250 °C) conversion efficiency of CO-SCR. When NO is used as a reductant, it can activate the catalytically inactive Z-[Fe(OH)₂]⁺ sites, by absorbing and subsequently forming HNO₂, which is easily desorbed leaving catalytically active Z-[FeOH]⁺ sites, resulting in improved decomposition performance below 427 °C (700 K).¹⁶⁷ Further studies involving more complex alloy compositions may be a critical step in developing next generation catalysts.

5 Outlook

5.1 High-Throughput Experimentation and Machine Learning for Catalyst Discovery

High-throughput (HT) synthesis and screening coupled with computationally guided design are essential as the exploratory compositional space continues to grow for novel catalytic discovery. Limited throughput of single-channel reactors hinders the ability to achieve rapid materials discovery.¹⁶⁸ HT reactor testing is beneficial for rapid materials discovery due to the ability to test multiple catalysts simultaneously, which greatly decreases the time needed to test a large number of catalysts within a compositional design space.¹⁶⁹⁻¹⁷¹ In general, HT experimentation has been implemented to test up to 48 different catalysts at a single time.¹⁷²⁻¹⁷⁴ The ability to collect large amounts of data from HT experimentation allows for the development of machine learning (ML) models to probe the complex design space and determine which features are important for specific reactions.¹⁷⁵

Currently, only a limited number of studies utilize HT experimentation to develop N₂O abatement catalysts. In one study, Li et al. utilized HT experimentation to analyze a variety of N₂O decomposition catalysts under the same reaction conditions. A reactor capable of testing 48 catalysts simultaneously was used. The activity across many catalysts was related back to the characteristics of the catalyst, such as the impact of the support and pretreatment conditions.²¹ Another study by Hendershot et al. investigated the optimization of a NO_x storage and reduction catalyst by using a statistical design of experiments model coupled with HT experimentation.¹⁷⁶ The HT setup quantified the production of N₂O from the catalysts as one of the factors analyzed. This work demonstrates the ability to analyze N₂O in an HT setup, which highlights the potential for further applications in future N₂O abatement technologies.

Recent studies have also applied ML to predict the NO emissions from wastewater treatment and agricultural crop production, two of the largest sources to global N₂O emissions (see Fig. 1).^{177, 178} Additionally, ML has been employed to predict the adsorption of N₂O on activated carbon and carbon molecular sieves.¹⁷⁹ A major development in computational studies that can be leveraged for catalytic N₂O abatement is machine-learned interatomic potentials (MLIPs). MLIPs, such as M3GNet, are trained on large databases of DFT data with neural networks to learn the underlying features to property relationships and use this to form universal interatomic potentials.¹⁸⁰ MLIPs provide DFT level accuracy for the energetics of elementary reaction steps at a fraction of the computational cost (~4–7 orders of magnitude faster). Furthermore, MLIPs enable the inclusion of time and temperature effects to capture the modelling of realistic catalyst dynamics.¹⁸¹ Coupled, these provide a very powerful tool for catalyst discover. However, to date, MLIPs have not been utilized in the literature for catalytic N₂O abatement and have only been used to study ternary oxides for syngas conversion and a NO + CO reaction.^{182, 183} Leveraging MLIPs for N₂O abatement studies would enable both more accurate activity predictions by incorporating the catalyst evolution and would also facilitate the exploration of exponentially larger compositional space of the catalysts.

Coupling experimentation and computational data with ML model development can allow researchers to take advantage of active learning (AL) to predict optimal catalysts while using HT experimentation to test large amounts of data. This approach has been utilized for NH₃ synthesis catalysts. A feature space of descriptors to characterize a promoted Ru catalyst for NH₃ synthesis was subdivided into reaction conditions, metal-support interactions, promoter-support interactions, metal-promoter interactions, catalyst preparation, and catalyst pretreatment, for a total of 536 features, which was reduced to 160 after feature selection. For AL to find the best performing promoters, the feature space was reduced again from 160 to 53 to limit it to only features that vary with the promoter. The AL predicted top performing promoter was synthesized and tested with HT experimentation, and the data added for the subsequent prediction.¹⁷⁰ Another ML approach was developed by Wang et al. that divided the feature space into catalyst composition, preparation conditions, and reaction conditions for the NH₃ for NO_x. The advantage of this feature space is it allows the catalyst composition to be optimized.¹⁸⁴ Though not explicitly studying N₂O abatement catalysts, these previous studies highlight the features and methodologies that have been proven effective and can be applied to these reactions.

Future studies coupling high-throughput experimentation with machine learning are imperative for catalytic discovery and optimization of novel catalysts for N₂O abatement reactions. This methodology will allow for rapid material screening to facilitate novel catalytic discovery at a more rapid pace while elucidating trends with ML.



5.2 Industrial Outlook for Catalytic Design

In many industrial plants, such as nitric acid and adipic acid, N_2O is not a “pure” byproduct but is rather produced in an effluent with other gases that may be inhibiting. With this comes an opportunity to develop novel catalysts that are tailored towards being resistant to other inhibiting gases. Many industrial pollutants, such as water and SO_2 , are emitted in addition to N_2O . As previously discussed in Section 2.4 and 3.5, these other additional gases in the feed stream inhibit catalytic activity and can result in irreversible deactivation of the catalyst. These considerations motivate the need for the discovery of resilient catalysts through the altering of the support or the addition of promoters to influence the binding of reactants and inhibitors. Many studies have begun to analyze catalyst compositions to improve their toxicity resistance. In short, other research groups have found that the addition of CeO_2 to a catalyst can increase water resistance with the synthesis of the catalysts also having an impact on the performance in the presence of catalytic toxins.^{13, 21, 35} In addition, a different review article summarized that the toxicity resistance can be further improved upon through the synthesis of varied structure materials, such as core-shell type catalysts or through doping the catalyst with other elements, such as Ti, Zn, or K as these dopants can further weaken the binding of these catalytic toxins to the active sites.^{13, 185, 186, 187} Though there have been studies first analyzing how to improve the toxicity resistance of abatement catalysts, there is still a drive to further develop catalysts that can be resistant to industrial pollutants while achieving high activity, increased longevity, and decreased cost. In addition, with the development of novel catalysts, it is imperative to assess the longevity of the catalysts in realistic industrial conditions as increasing the catalysts lifetime will help save industrial operating costs. Other considerations for novel catalyst design should include catalyst cost, increasing activity at lower temperatures, as well as minimizing the environmental footprint for the large-scale synthesis and utilization of these catalysts. High performing catalysts, as seen with the direct decomposition section, include noble metals with the incorporation of other elements as promoters or supports, such as rare earth metals. This combination of materials may be active, but it may also come with tradeoffs in terms of cost deeming large-scale implementation challenging. Through larger studies, novel active materials and combinations of metals, supports, and promoters can be found while reducing expensive component weight loadings to decrease costs. With these additional considerations in mind, ML and HT experiments can be utilized to more rapidly achieve industrial N_2O abatement goals.

In conjunction with the opportunities for catalytic design for these industrial applications, there also comes additional challenges with the integration of these systems into large-scale industrial units. One challenge that will be faced involves the reactor design to allow for effective conversion of N_2O . This can be done by designing packed bed reactors with monoliths or

with the use of membrane reactors to further enhance catalytic activity. In addition, new reactor designs come with the consideration of pressure drop through the catalytic bed. With a pressure drop in the system, it will become more costly for operations not only in energy requirements but because it can alter the thermodynamics of the reaction and negatively impact catalytic activity. This problem can be further mitigated by developing pelletized catalysts or through the synthesis of monoliths. In addition, there is further work needed to be done to assess how these catalysts perform in conjunction with other catalytic systems, such as de- NO_x , to ensure selectivity and decomposition of all harmful products. As these new industrial reactor designs are studied, chosen catalytic systems should be subjected to longevity tests to ensure sufficient catalytic activity in the industrial gas streams.

Following catalytic design considerations, further work is also needed in the work of technoeconomic analysis and life cycle analysis. A technoeconomic analysis would be able to help researchers and industry determine if an effective catalytic design is economically viable for large-scale applications. As mentioned, some catalysts may show higher activity but are hindered for further usage due to high cost of materials. However, there may be tradeoffs with choosing cheaper materials that may not have as high of activity but will meet N_2O abatement requirements. In addition, lifecycle analysis should be performed to analyze the environmental impact of the catalysts used from their creation to their disposal. This can aid in helping companies choose materials for their catalytic reactor systems that are less environmentally harmful to better align with industrial goals of reducing their carbon footprint.

6. Conclusions

Various catalytic designs for N_2O abatement were reviewed, with a specific focus on direct decomposition and selective catalytic reduction (SCR) pathways. Mechanistic insights for different catalytic systems, supported by transient kinetic studies and density functional theory calculations were also discussed. The review emphasizes viable operating conditions and mechanisms, highlighting three main catalyst-based designs of supported metal, metal oxide, and zeolite catalysts.

Previous studies have identified Rh as one of the most active metals for direct decomposition, with the choice of support playing a crucial in regenerating catalytic active sites. Metal oxide catalysts, such as Co_3O_4 , Mn_2O_3 , CuO, and NiO, as well as Fe-, Co-, and Cu-exchanged zeolites, have also emerged as promising, cost-effective alternatives to noble metal-based catalysts. Additionally, the incorporation of alkali metals and lanthanides as promoters has been shown to increase the catalytic activity by improving redox properties and promoting oxygen desorption from catalyst surfaces, thereby offering an opportunity to further lower respective T_{50} values.

The addition of reductants for SCR shifts the N_2O conversion towards lower T_{50} values, as shown across various catalyst



systems (e.g., Fe-zeolites, Rh-FAU, RuO₂, and metal oxides). Reductants (i.e., CO, hydrocarbons, NH₃, and H₂) effectively aid in N₂O abatement by promoting the removal of the adsorbed oxygen species and reducing the temperature required for N₂O conversion. H₂ achieves the lowest T₅₀ median temperature (129 °C) for the SCR catalysts, whereas hydrocarbons exhibited the highest at temperature (413 °C for C₃H₆). However, it should be noted that comparing the efficiency of reductants is not trivial, as the performance depends on the catalyst active sites-reductant interaction, as well as reaction conditions.

Fe-zeolites (e.g., Fe-MFI, Fe-MOR, Fe-BEA, and Fe-SSZ-13) are extensively studied for their high N₂O-SCR activity, low cost, and low toxicity, which makes them suitable for industrial applications. Moreover, the SCR catalysts reported a lower median T₅₀ (374 °C) than direct decomposition (432 °C). Among the catalyst classes (supported metals, metal oxides, and zeolites), the metal oxide catalysts achieved the lowest T₅₀ values (350 °C and 216 °C for direct decomposition and SCR, respectively).

Future catalytic design must be tailored to be robust against common impurity gases found in industrial sources, such as O₂, H₂O, NO, and SO₂. The literature suggests that O₂ desorption is a rate-limiting step in the direct decomposition of N₂O and also inhibits the SCR of N₂O. Overall, the presence of O₂ and H₂O typically hinders both abatement processes through competitive adsorption, non-selective oxidation of reductants, and alteration of the surface redox state of the catalyst. Coupling machine learning (ML) with high throughput (HT) experiments offers a promising approach to rapidly screen catalytic materials and gaseous reaction feeds for enhanced catalytic activity while tailoring different considerations towards industrial concerns and applications.

Author contributions

Conceptualization: DDR

Data curation: HC, SS

Funding acquisition: DDR, MC

Investigation: HC, SS, MNG, MM

Project administration: DDR, JL, RF, DA, MC

Supervision: DDR, JL, RF, DA, MC

Visualization: HC, SS, MNG, MM

Writing – original draft: HC, SS, MNG, MM

Writing – review & editing: HC, SS, MNG, MM, DDR

Conflicts of interest

There are no conflicts to declare.

Data availability

No primary research results, software or code have been included, and no new data were generated or analysed as part of this review.

Acknowledgements

View Article Online

DOI: 10.1039/D5CY01360G

The authors acknowledge the following funding sources:

Battelle Savannah River Alliance, LLC under Contract No. 89303321CEM000080 with the U.S. Department of Energy. Publisher acknowledges the U.S. Government license to provide public access under DOE Public Access Plan (<http://energy.gov/downloads/doe-public-access-plan>). (MNG, MC, DDR)

Battelle Energy Alliance, LLC under contract DE-AC07-05ID14517 with the U.S. Department of Energy. (HC, RF).

LAB 23-EM001 Hanford Tank Waste Cleanup R&D Program, U.S. Department of Energy, Environmental Management Office, Laboratory Policy Office. (DDR)

Laboratory Directed Research and Development (LDRD) Program within the Savannah River National Laboratory. (MNG, MC)

References

- O. D. Frutos, G. Quijano, A. Aizpuru and R. Munoz, *Biotechnol. Adv.*, 2018, 36, 1025–1037.
- United Nations Environment Programme (UNEP), Drawing Down N₂O to Protect Climate and the Ozone Layer. A UNEP Synthesis Report, Nairobi, Kenya, 2013.
- J. Pérez-Ramírez, F. Kapteijn, K. Schöffel and J. A. Moulijn, *Appl. Catal., B*, 2003, 44, 117–151.
- X. Lan, K. W. Thoning and E. J. Dlugokencky, 2025, Trends in globally-averaged CH₄, N₂O, and SF₆ determined from NOAA Global Monitoring Laboratory measurements (Version 2025-05), Repository, <https://doi.org/10.15138/P8XG-AA10>.
- G. Zhu, H. Shi, L. Zhong, G. He, B. Wang, J. Shan, P. Han, T. Liu, S. Wang, C. Liu, N. Zhang, L. Jiang, L. Yu, C. Zhan, Z. Tang, T. Wen, B. Ma, X. Su, S. Zhang, J. Zhang, H. Di, L. Hou, A. H. Krichels, M. Trimmer, M. S. M. Jetten, Y. Peng, F. E. Löffler, H. Tian and Y.-G. Zhu, *Nat. Rev. Earth Environ.*, 2025, 6, 574–592.
- W. Jörß, S. Ludig and L. Schneider, Mitigation potentials for emissions of nitrous oxide from chemical industry in industrialised countries world-wide, Öko-Institut e.V., Freiburg, Germany, 2023.
- A. Shimizu, K. Tanaka and M. Fujimori, *Chemosphere*, 2000, 2, 425–434.
- K. Rafiq, M. Sabir, I. Sadia, M. Z. Abid, M. A. Nadeem and E. Hussain, *Mater. Adv.*, 2025, 6, 8239–8276.
- M. Qian, B. Guan, Z. Zhuang, J. Chen, L. Zhu, Z. Ma, X. Hu, C. Zhu, S. Zhao, K. Shu, H. Dang, T. Zhu and Z. Huang, *Catalysis Science & Technology*, 2025, 15, 2061–2103.
- Y. Zhang, Z. Tian, L. Huang, H. Fan, Q. Hou, P. Cui and W. Wang, *Catalysts*, 2023, 13, 943.
- M. Konsolakis, *ACS Catal.*, 2015, 5, 6397–6421.
- X. Wu, J. Du, Y. Gao, H. Wang, C. Zhang, R. Zhang, H. He, G. Lu and Z. Wu, *Chem. Soc. Rev.*, 2024, 53, 8379–8423.
- Z. Zhuang, B. Guan, J. Chen, C. Zheng, J. Zhou, T. Su, Y. Chen, C. Zhu, X. Hu, S. Zhao, J. Guo, H. Dang, Y. Zhang, Y. Yuan, C. Yi, C. Xu, B. Xu, W. Zeng, Y. Li, K. Shi, Y. He, Z. Wei and Z. Huang, *Chem. Eng. J.*, 2024, 486, 150374.



14. L. Xu, B. Guan, L. Zhu, S. Chang, J. Ma, R. Wang, D. Yang, T. Zhu, H. Qu, B. Tan and Z. Huang, *J. Environ. Chem. Eng.*, 2026, 14, 122211.
15. Y. Bai, B. Guan, L. Zhu, S. Chang, J. Ma, R. Wang, D. Yang, T. Zhu, K. Shu, Z. Zhuang, X. Hu, C. Zhu, S. Zhao, J. Chen, J. Gao, H. Dang, L. Zhang, Y. Li, L. Xu, W. Zeng, S. Chen, L. Wang, C. Zhu, J. He, Q. Xian and Z. Huang, *Energy*, 2026, 351, 140790.
16. J. Gao, B. Guan, L. Zhu, S. Chang, J. Ma, R. Wang, D. Yang, T. Zhu, H. Qu, B. Tan and Z. Huang, *Fuel*, 2026, 419, 138780.
17. A. a. D. Bhan, W. N., *J. Catal.*, 2022, 405, 419–429.
18. M. Boudart, *Chem. Rev.*, 1995, 95, 661–666.
19. E. A. Davidson and D. Kanter, *Environ. Res. Lett.*, 2014, 9, 105012.
20. Y. Wu, Y. Zheng and P. Granger, in *Advances in Catalysts Research*, ed. S. J. Ikhmayies, Springer Nature Switzerland, Cham, 2024, https://doi.org/10.1007/978-3-031-49108-5_7, pp. 221–257.
21. Y. Li, A. Sundermann, O. Gerlach, K.-B. Low, C. C. Zhang, X. Zheng, H. Zhu and S. Axnanda, *Catal. Today*, 2020, 355, 608–619.
22. N. Zhang, C. He, Y. Jing, Y. Qian, Y. Qin, H. Lin, M. Obuchi, R. Toyoshima, H. Kondoh and K. Oka, *Angew. Chem.*, 2025, 137, e202517403.
23. K. S. Egorova and V. P. Ananikov, *Angew. Chem. Int. Ed.*, 2016, 55, 12150–12162.
24. A. Wang, Wang, Y., Walter, E. D., Kukkadapu, R. K., Guo, Y., Lu, G., Weber, R. S., Wang, Y., Peden, C. H. F., Gao, F., *J. Catal.*, 2018, 358, 199–210.
25. P. Boroń, Chmielarz, L., Gurgul, J., Łątka, K., Gil, B., Marszałek, B., Dzwigaj, S., *Microporous Mesoporous Mater.*, 2015, 203, 73–85.
26. M. Rutkowska, Chmielarz, L., Macina, D., Piwowarska, Z., Dudek, B., Adamski, A., Witkowski, S., Sojka, Z., Obalová, L., Van Oers, C. J., Cool, P., *Appl. Catal., B*, 2014, 146, 112–122.
27. S. Pares-Esclapez, L. Such-Basanez, M. J. Illan-Gomez, C. Salinas-Martinez de Lecea and A. Bueno-Lopez, *J. Catal.*, 2010, 276, 390–401.
28. F. Lin, T. Andana, Y. Wu, J. Szanyi, Y. Wang and F. Gao, *J. Catal.*, 2021, 401, 70–80.
29. V. A. Kondratenko and M. Baerns, *J. Catal.*, 2004, 225, 37–44.
30. Y. Sun, Y. Wu, H. Wang and Z. Wu, *Environ. Sci. Technol.*, 2025, 59, 24777–24785.
31. E. Wilczkowska, Krawczyk, K., Petryk, J., Sobczak, J., Kaszukur, Z., *Appl. Catal., A*, 2010, 389, 165–172.
32. G. Pekridis, Athanasiou, C., Konsolakis, M., Yentekakis, I. V., Marnellos, G. E., *Top. Catal.*, 2009, 52, 1880–1887.
33. E. Pachatouridou, Papista, E., Iliopoulou, E. F., Delimitis, A., Goula, G., Yentekakis, I. V., Marnellos, G. E., Konsolakis, M., *J. Environ. Chem. Eng.*, 2015, 3, 815–821.
34. J. P. Dacquin, Dujardin, C., Granger, P., *Catal. Today*, 2008, 137, 390–396.
35. H. Zhu, Y. Li and X. Zheng, *Appl. Catal., A*, 2019, 571, 89–95.
36. J. Haber, Nattich, M., Machej, T., *Appl. Catal., B*, 2008, 77, 278–283.
37. N. Zhang, C. He, Y. Jing, Y. Qian, T. Toyao and K.-i. Shimizu, *Surf. Interfaces*, 2024, 46, 104120.
38. M. Konsolakis, C. Drosou and I. V. Yentekakis, *Appl. Catal., B*, 2012, 123–124, 405–413. DOI: 10.1039/D5CY01360G
39. S. C. Christoforou, E. A. Efthimiadis and I. A. Vasalos, *Catal. Lett.*, 2002, 79, 137–147.
40. M. Konsolakis, I. V. Yentekakis, G. Pekridis, N. Kaklidis, A. C. Psarras and G. E. Marnellos, *Appl. Catal., B*, 2013, 138–139, 191–198.
41. J. Arenas-Alatorre, A. Gómez-Cortés, M. Avalos-Borja and G. Díaz, *J. Phys. Chem. B*, 2005, 109, 2371–2376.
42. T. Yamashita, Vannice, A., *J. Catal.*, 1996, 161, 254–262.
43. M. Zabilskiy, Djinojic, P., Tchernychova, E., Pintar, A., *Appl. Catal., B*, 2016, 197, 146–158.
44. L. Xue, He, H., Liu, C., Zhang, C., Zhang, B., *Environ. Sci. Technol.*, 2008, 43, 890–895.
45. F. Zhao, Wang, D., Li, X., Yin, Y., Wang, C., Qiu, L., Yu, J., Chang, H., *Ind. Eng. Chem. Res.*, 2022, 61, 13854–13862.
46. B. M. Abu-Zied, Soliman, S. A., Asiri, A., *Appl. Surf. Sci.*, 2019, 479, 148–157.
47. H. Liu, Chen, J., Wang, Y., Xiong, S., Su, Z., Wang, Y., Yang, W., Chu, X., Yang, W., Peng, Y., Si, W., Li, J., *Chem. Eng. J.*, 2021, 414, 128643.
48. Z. Zhang, Wu, Y., Sun, Y., Wang, H., Wu, Z., Wu, X., *ACS ES&T Eng.*, 2024, 4, 2542–2552.
49. Y. Sun, Y. Wu, Z. Zhang, X. Wu, H. Wang and Z. Wu, *ChemCatChem*, 2025, 17, e202401060.
50. H. Yu, Y. Li, Y. Du, Y. Pan, L. Yang, R. Han, W. Shan and Y. Xiong, *Sep. Purif. Technol.*, 2026, 382, 136112.
51. H. Yu, Y. Li, Y. Pan, Y. Du, X. Feng, J. Cui, Z. Lou, W. Shan and Y. Xiong, *Chem. Eng. J.*, 2025, 504, 159032.
52. K. Wang, Y. Du, Y. Li, X. Qi, W. Shan, H. Yu and Y. Xiong, *Mol. Catal.*, 2024, 569, 114604.
53. R. Wu, Q. Wang, R. Wang, X. Lin, H. Dang, L. Li, S. Hu, M. Yang, K. Zheng, L. Zhang, Y. Wang and Y. Zhao, *ChemCatChem*, 2025, 17, e202401659.
54. X. Hu, J. Meng, L. Feng, Y. Gao, Y. Wang and Y. Zhao, *Catal. Lett.*, 2024, 154, 4367–4377.
55. Q. Wang, W. Yang, H. Dang, L. Li, R. Wu, Y. Wang and Y. Zhao, *J. Environ. Chem. Eng.*, 2024, 12, 112463.
56. M. Santiago, V. A. Kondratenko, E. V. Kondratenko, N. López and J. Pérez-Ramírez, *Appl. Catal., B*, 2011, 110, 33–39.
57. B. Li, X. Duan, T. Zhao, B. Niu, G. Li, Z. Zhao, Z. Yang, D. Liu, F. Zhang, J. Cheng and Z. Hao, *Environ. Sci. Technol.*, 2024, 58, 2153–2161.
58. T. Ishihara, M. Ando, K. Sada, K. Takiishi, K. Yamada, H. Nishiguchi and Y. Takita, *J. Catal.*, 2003, 220, 104–114.
59. K. S. Chang, H.-J. Lee, Y.-S. Park and J.-W. Woo, *Appl. Catal., A*, 2006, 309, 129–138.
60. K. Pacultová, L. Obalová, F. Kovanda and K. Jiráťová, *Catal. Today*, 2008, 137, 385–389.
61. K. S. Chang and X. Peng, *J. Ind. Eng. Chem.*, 2010, 16, 455–460.
62. X. Zhang, Shen, Q., He, C., Ma, C., Cheng, J., Liu, Z., Hao, Z., *Catal. Sci. Technol.*, 2012, 2, 1249–1258.
63. Z. Sobalík, Jiřa, K., Kaucký, D., Vondrová, A., Tvarůžková, Z., Nováková, J., *Catal. Lett.*, 2007, 113, 124–129.
64. A. Guzmán-Vargas, Delahay, G., Coq, B., *Appl. Catal., B*, 2003, 42, 369–379.
65. J. B. Lim, Cha, S. H., Hong, S. B., *Appl. Catal., B*, 2019, 243, 750–759.



ARTICLE

Catalysis Science & Technology

66. M. Wu, Chen, X., Zhong, L., Wang, H., Zhang, X., Shen, Q., Wei, W., Sun, Y., Greenhouse Gases: Sci. Technol., 2016, 6, 710–723.
67. G. Delahay, M. Mauvezin, A. Guzmán-Vargas and B. Coq, Catal. Commun., 2002, 3, 385–389.
68. J. Pérez-Ramírez, F. Kapteijn and A. Brückner, J. Catal., 2003, 218, 234–238.
69. J. Pérez-Ramírez, M. S. Kumar and A. Brückner, J. Catal., 2004, 223, 13–27.
70. M. D. Boutarouch, J. G. Cortés, M. S. El Begrani, C. S. M. de Lecea and J. Perez-Ramirez, Appl. Catal., B, 2004, 54, 115–123.
71. M. N. Debbagh, C. S. M. d. Lecea and J. Pérez-Ramírez, Appl. Catal., B, 2007, 70, 335–341.
72. Q. Shen, L. Li, C. He, H. Tian, Z. Hao and Z. P. Xu, Appl. Catal., B, 2009, 91, 262–268.
73. X. Zhang, Q. Shen, C. He, C. Ma, J. Cheng and Z. Hao, Catal. Commun., 2012, 18, 151–155.
74. X. Zhang, Q. Shen, C. He, C. Ma, J. Cheng, L. Li and Z. Hao, ACS Catal., 2012, 2, 512–520.
75. M. Mauvezin, G. Delahay, B. Coq and S. Kieger, Appl. Catal., B, 1999, 23, L79–L82.
76. H. Yoshida, Tsuruta, T., Yazawa, Y., Hattori, T., Appl. Catal., A, 2007, 325, 50–56.
77. A. Wang, J. Li and T. Zhang, Nat. Rev. Chem., 2018, 2, 65–81.
78. K. Liu, Y. Tang, Z. Yu, B. Ge, G. Ren, Y. Ren, Y. Su, J. Zhang, X. Sun, Z. Chen, X. Liu, B. Qiao, W.-Z. Li, A. Wang and J. Li, Sci. China Mater., 2020, 63, 949–958.
79. S. Bao, X. Lu, L. Yu, Y. Song, H. Fu, X. Qu, J. Y. Park and S. Zheng, Appl. Catal., A, 2025, 693, 120122.
80. Q. Wang and D. Astruc, Chem. Rev., 2019, 120, 1438–1511.
81. F. Abbasi and C. Ghotbi, J. Environ. Chem. Eng., 2025, 13, 118757.
82. H. Tang, Y. He, P. Liu, J. Shao, F. Lin and Z. Wang, Energy & Fuels, 2021, 35, 18664–18679.
83. P. Zhao, F. Qin, Z. Huang, C. Sun, W. Shen and H. Xu, Chem. Eng. J., 2018, 349, 72–81.
84. Y. Jing, K. Taketoshi, N. Zhang, C. He, T. Toyao, Z. Maeno, T. Otori, N. Ishikawa and K.-i. Shimizu, ACS Catal., 2022, 12, 6325–6333.
85. Y. Jing, C. He, N. Zhang, Y. Murano, R. Toyoshima, H. Kondoh, Y. Kageyama, H. Inomata, T. Toyao and K.-i. Shimizu, ACS Catal., 2023, 13, 12983–12993.
86. Structure Commission of the International Zeolite Association, *Atlas of Zeolite Framework Types*, Elsevier Science B.V., 2007.
87. L. S. Dent and J. V. Smith, Nature, 1958, 181, 1794–1796.
88. G. T. Kokotailo, S. L. Lawton, D. H. Olson and W. M. Meier, Nature, 1978, 272, 437–438.
89. P. Simoncic and T. Armbruster, Am. Mineral., 2004, 89, 421–431.
90. J. B. Higgins, R. B. LaPierre, J. L. Schlenker, A. C. Rohrman, J. D. Wood, G. T. Kerr and W. J. Rohrbaugh, Zeolites, 1988, 8, 446–452.
91. P. T. Fanson, Stradt, M. W., Lauterbach, J. L., Delgass, W. N., Appl. Catal., B, 2002, 38, 331–347.
92. D. C. Cano-Blanco, J. W. A. Fischer, F. Buttignol, I. Alxneit, G. Jeschke, O. Kröcher and D. Ferri, ACS Catal., 2025, 15, 15579–15595.
93. G. E. Marnellos, E. A. Efthimiadis and I. A. Vasalos, Appl. Catal., B, 2003, 46, 523–539. DOI: 10.1039/D5CY01360G
94. L. Xue, C. Zhang, H. He and Y. Teraoka, Appl. Catal., B, 2007, 75, 167–174.
95. M. Konsolakis, I. V. Yentekakis, G. Pekridis, N. Kaklidis, A. C. Psarras and G. E. Marnellos, Applied Catalysis B: Environmental, 2013, 138–139, 191–198.
96. A. Serrano-Lotina, S. Pérez-Ferreras, C. Álvarez-Galván, R. E. Rojas-Hernandez, J. F. Fernández, P. Ávila, M. A. Bañares and F. Rubio-Marcos, Chem. Eng. J., 2025, 524, 169338.
97. S. N. Basahel, M. Mokhtar, T. T. Ali and K. Narasimharao, Catal. Today, 2020, 348, 166–176.
98. G. Sádovská, E. Tabor, P. Sazama, M. Lhotka, M. Bernauer and Z. Sobalík, Catal. Commun., 2017, 89, 133–137.
99. F. Buttignol, D. Rentsch, I. Alxneit, A. Garbujo, P. Biasi, O. Kröcher and D. Ferri, Catalysis Science & Technology, 2022, 12, 7308–7321.
100. I. Melián-Cabrera, C. Mentrui, J. A. Z. Pieterse, R. W. van den Brink, G. Mul, F. Kapteijn and J. A. Moulijn, Catal. Commun., 2005, 6, 301–305.
101. G. Giecko, T. Borowiecki, W. Gac and J. Kruk, Catal. Today, 2008, 137, 403–409.
102. S. Alini, F. Basile, S. Blasioli, C. Rinaldi and A. Vaccari, Appl. Catal., B, 2007, 70, 323–329.
103. X. Wu, J. Du, Y. Gao, H. Wang, C. Zhang, R. Zhang, H. He, G. Lu and Z. Wu, Chem. Soc. Rev., 2024, 53, 8379–8423.
104. T. Nobukawa, M. Yoshida, K. Okumura, K. Tomishige and K. Kunimori, J. Catal., 2005, 229, 374–388.
105. M. Kögel, R. Mönig, W. Schwieger, A. Tissler and T. Turek, J. Catal., 1999, 182, 470–478.
106. R. W. van den Brink, S. Booneveld, J. R. Pels, D. F. Bakker and M. J. F. M. Verhaak, Appl. Catal., B, 2001, 32, 73–81.
107. M. A. G. Hevia and J. Pérez-Ramírez, Environ. Sci. Technol., 2008, 42, 8896–8900.
108. J. Pérez-Ramírez and F. Kapteijn, Appl. Catal., B, 2004, 47, 177–187.
109. S. Du, B. Kang, X. Guo, Y. Wei, J. Jia and R. Zhang, Catal. Lett., 2024, 154, 3947–3957.
110. S. Roy, M. Hegde, S. Sharma, N. Lalla, A. Marimuthu and G. Madras, Appl. Catal., B, 2008, 84, 341–350.
111. Y. Wu, X. Wu, J. Fan, H. Wang and Z. Wu, Environ. Sci. Technol., 2024, 58, 22583–22593.
112. L.-L. Zhang, X.-M. Chen and C.-G. Liu, Inorganic Chemistry, 2019, 58, 5221–5229.
113. Y. Qian, S. Yasumura, N. Zhang, A. Anzai, T. Toyao and K.-i. Shimizu, Chin. J. Catal., 2025, 69, 185–192.
114. J. W. A. Fischer, F. Buttignol, A. Garbujo, D. Ferri and G. Jeschke, Chem. Sci., 2025, 16, 4884–4891.
115. A. A. Khan, S. A. Alsalthi and A. U. Rahman, Physical Chemistry Chemical Physics, 2024, 26, 17110–17117.
116. A. H. Ragab, L. O. Mallasiy, S. R. Al-Mhyawi and I. Khan, Diamond Relat. Mater., 2026, 161, 113073.
117. M. Konsolakis, C. Drosou and I. V. Yentekakis, Applied Catalysis B: Environmental, 2012, 123–124, 405–413.
118. K. S. Chang, H.-J. Lee, Y.-S. Park and J.-W. Woo, Applied Catalysis A: General, 2006, 309, 129–138.
119. J. H. Holles, M. A. Switzer and R. J. Davis, J. Catal., 2000, 190, 247–260.
120. T. Nobukawa, M. Yoshida, S. Kameoka, S.-i. Ito, K. Tomishige and K. Kunimori, J. Phys. Chem. B, 2004, 108, 4071–4079.



121. B. R. Wood, J. A. Reimer, A. T. Bell, M. T. Janicke and K. C. Ott, *J. Catal.*, 2004, 225, 300–306.
122. M. C. Campa, S. Morpurgo, G. Luccisano, M. Leone and D. Pietrogiacomini, *Microporous Mesoporous Mater.*, 2025, 398, 113818.
123. M. C. Campa, D. Pietrogiacomini, C. Catracchia, S. Morpurgo, J. Olszowka, K. Mlekodaj, M. Lemishka, J. Dedecek, A. Kornas and E. Tabor, *Appl. Catal., B*, 2024, 342, 123360.
124. S. Liu, S. Yasumura, Z. Maeno, T. Ohnishi and M. Ogura, *Appl. Catal. B: Environ.*, 2025, 373, 125365.
125. D. Pietrogiacomini, M. C. Campa, L. R. Carbone and M. Occhiuzzi, *Appl. Catal., B*, 2019, 240, 19–29.
126. T. J. Vulic, A. F. K. Reitzmann and K. Lázár, *Chem. Eng. J.*, 2012, 207–208, 913–922.
127. B. Guan, Z. Zhuang, L. Zhu, L. Xu, S. Chang, J. Ma, R. Wang, D. Yang, T. Zhu, H. Qu, B. Tan and Z. Huang, *Catal. Lett.*, 2026, 156, 72.
128. B. Guan, Z. Zhuang, L. Zhu, X. Hu, C. Zhu, S. Zhao, J. Chen, J. Gao, K. Shu, H. Dang, L. Zhang, T. Zhu, Y. Li, L. Xu, W. Zeng, S. Chen, L. Wang, C. Zhu, J. He, Q. Xian and Z. Huang, *Fuel*, 2026, 406, 136937.
129. J. W. Fischer, D. C. Cano-Blanco, H. Karas, F. Buttignol, O. Kröcher, D. Ferri and G. Jeschke, *ChemCatChem*, 2026, 18, e01575.
130. Z. Zhuang, B. Guan, L. Zhu, X. Hu, C. Zhu, S. Zhao, J. Chen, K. Shu, H. Dang, J. Gao, L. Zhang, T. Zhu, M. Qian, W. Zeng, S. Chen, L. Wang, C. Zhu, J. He, Q. Xian and Z. Huang, *Chem. Eng. J.*, 2025, 522, 167265.
131. J. H. Baek, S. M. Lee, J. H. Park, J. M. Jeong, R. H. Hwang, C. H. Ko, S. G. Jeon, T. H. Choi and K. B. Yi, *J. Ind. Eng. Chem.*, 2017, 48, 194–201.
132. C.-G. Liu, Y.-J. Chu, L.-L. Zhang, C. Sun and J.-Y. Shi, *Environ. Sci. Technol.*, 2019, 53, 12893–12903.
133. X. Zhang, Q. Shen, C. He, C. Ma, J. Cheng and Z. Hao, *Catalysis Communications*, 2012, 18, 151–155.
134. L. Han, S. Cai, M. Gao, J.-y. Hasegawa, P. Wang, J. Zhang, L. Shi and D. Zhang, *Chem. Rev.*, 2019, 119, 10916–10976.
135. Z. Zhang, Z. He, Y. Ye, Y. Wang, C. Liu, Y. Tan, Z. Yin and M. Pan, *Fuel Process. Technol.*, 2026, 284, 108412.
136. X. Wang, Y. Xiong, H. Tan, Y. Liu, Y. Niu and T. Xu, *Energy & fuels*, 2012, 26, 3125–3131.
137. W. Xie, Z. Sun, Y. Xiong, L. Li, T. Wu and D. Liang, *Int. J. Min. Sci. Technol.*, 2014, 24, 471–475.
138. Z. Wang, H. Kuang, J. Zhang, L. Chu and Y. Ji, *Appl. Sci.*, 2019, 9, 1656.
139. Z. Zhang, W. Zhong, C. Mao, Y. Xu, K. Lu, Y. Ye, W. Guan, M. Pan and D. Tan, *Energy*, 2024, 294, 130899.
140. M. Zheng and X. Zhang, *Prog. React. Kinet. Mech.*, 2025, 50, e003.
141. J. Sun, L. Li, G. Zhou, X. Wang, L. Zhang, Y. Liu, J. Yang, X. Lü and F. Jiang, *Environ. Sci. Technol.*, 2018, 52, 4754–4762.
142. X. Lü, H. Li, X. Du, X. Wang, M. Lan, J. Wu, J. Zhu, J. Sun and F. Jiang, *React. Chem. Eng.*, 2020, 5, 561–569.
143. W. Yang, Q. Zhao, H. Lu, Z. Ding, L. Meng and G.-H. Chen, *Water Res.*, 2016, 90, 176–184.
144. J. T. Gleaves, G. Yablonsky, X. Zheng, R. Fushimi and P. L. Mills, *J. Mol. Catal. A: Chem.*, 2010, 315, 108–134.
145. R. Fushimi and J. Gleaves, *Curr. Opin. Chem. Eng.*, 2018, 21, 10–21.
146. R. Fushimi, in *Springer Handbook of Advanced Catalyst Characterization*, eds. I. E. Wachs and M. A. Bañares, Springer International Publishing, Cham, 2023, https://doi.org/10.1007/978-3-031-07125-6_40, pp. 899–934.
147. K. Morgan, N. Maguire, R. Fushimi, J. T. Gleaves, A. Goguet, M. P. Harold, E. V. Kondratenko, U. Menon, Y. Schuurman and G. S. Yablonsky, *Catal. Sci. Technol.*, 2017, 7, 2416–2439.
148. E. V. Kondratenko and J. Pérez-Ramírez, *Catal. Today*, 2007, 119, 243–246.
149. E. V. Kondratenko and J. Pérez-Ramírez, *Catal. Today*, 2007, 121, 197–203.
150. E. V. Kondratenko and J. Pérez-Ramírez, *J. Phys. Chem. B*, 2006, 110, 22586–22595.
151. E. V. Kondratenko, V. A. Kondratenko, M. Santiago and J. Pérez-Ramírez, *J. Catal.*, 2008, 256, 248–258.
152. E. V. Kondratenko, V. A. Kondratenko, M. Santiago and J. Pérez-Ramírez, *Appl. Catal., B*, 2010, 99, 66–73.
153. J. Pérez-Ramírez, F. Kapteijn, G. Mul and J. A. Moulijn, *J. Catal.*, 2002, 208, 211–223.
154. V. Gölden, S. Sokolov, V. A. Kondratenko and E. V. Kondratenko, *Appl. Catal., B*, 2010, 101, 130–136.
155. E. V. Kondratenko and J. Pérez-Ramírez, *Catal. Lett.*, 2003, 91, 211–216.
156. E. V. Kondratenko and J. Pérez-Ramírez, *Appl. Catal., A*, 2004, 267, 181–189.
157. V. A. Kondratenko and M. Baerns, *Journal of Catalysis*, 2004, 225, 37–44.
158. J. Pérez-Ramírez, E. V. Kondratenko and M. N. Debbagh, *J. Catal.*, 2005, 233, 442–452.
159. E. V. Kondratenko and J. Pérez-Ramírez, *Appl. Catal., B*, 2006, 64, 35–41.
160. V. Butera, *Physical Chemistry Chemical Physics*, 2024, 26, 7950–7970.
161. G. Henkelman, A. Arnaldsson and H. Jónsson, *Computational Materials Science*, 2006, 36, 354–360.
162. B. Hammer and J. K. Nørskov, *Nature*, 1995, 376, 238–240.
163. K. Kim, S. Baek, J. J. Kim and J. W. Han, *Appl. Surf. Sci.*, 2020, 510, 145349.
164. J. Sun, L. Wang, L. Zhang, Y. Zhao, Y. Chi, H. Wang, C. Li, J. Liu and J. Liu, *ACS Appl. Energy Mater.*, 2021, 4, 8496–8505.
165. X. Wang, R. Duan, Z. Li, M. Gao, Y. Fu, Y. Han, G. He and H. He, *Environ. Sci. Technol.*, 2025, 59, 5839–5847.
166. A. Heyden, B. Peters, A. T. Bell and F. J. Keil, *J. Phys. Chem. B*, 2005, 109, 1857–1873.
167. A. Heyden, N. Hansen, A. T. Bell and F. J. Keil, *J. Phys. Chem. B*, 2006, 110, 17096–17114.
168. K. McCullough, Williams, T., Mingle, K., Jamshidi, P., Lauterbach, J., *Phys. Chem. Chem. Phys.*, 2020, 22, 11174–11196.
169. R. J. Hendershot, Snively, C. M., Lauterbach, J., *Chem. - Eur. J.*, 2005, 11, 806–814.
170. R. Jayarathna, Onsee, T., Drummond, S., Naglic, J., Lauterbach, J., *J. Mater. Chem. A*, 2024, 12, 3046–3060.
171. J. Hatrick-Simpers, Wen, C., Lauterbach, J., *Catal. Lett.*, 2015, 145, 290–298.
172. T. N. Nguyen, Nhat, T. T. Phuong, Takimoto, K., Thakur, A., Nishimura, S., Ohyama, J., Miyazato, I., Takahashi, L.,



- Fujima, J., Takahashi, K., Taniike, T., ACS Catal., 2020, 10, 921–932.
173. C. Kiener, Kurtz, M., Wilmer, H., Hoffmann, C., Schmidt, H.-W., Grunwaldt, J.-D., Muhler, M., Schüth, F., J. Catal., 2002, 216, 110–119.
174. R. J. Hendershot, Vijay, R., Snively, C. M., Lauterbach, J., Chem. Eng. Sci., 2006, 61, 3907–3916.
175. B. MacQueen, Jayarathna, R., Lauterbach, J., Curr. Opin. Chem. Eng., 2022, 36, 100781.
176. R. J. Hendershot, W. B. Rogers, C. M. Snively, B. A. Ogunnaike and J. Lauterbach, Catal. Today, 2004, 98, 375–385.
177. J. Lyu, X. Liu, X. Ping, Q. Yang, S. Huang, X. Cao, X. Jia, N. Zhang, C. Huang and B. Wang, J. Water Process Eng., 2025, 71, 107306.
178. P. R. Adler, H. Nguyen, B. M. Rau and C. J. Dell, Environ. Res. Commun., 2024, 6, 091004.
179. H. Mashhadimoslem and A. Ghaemi, Environmental Science and Pollution Research, 2023, 30, 4166–4186.
180. C. Chen and S. P. Ong, Nat. Comput. Sci., 2022, 2, 718–728.
181. G. Olajide, K. Baral, S. Ezendu, A. Soyemi and T. Szilvasi, J. Catal., 2025, 448, 116202.
182. S. Ma, S.-D. Huang and Z.-P. Liu, Nat. Catal., 2019, 2, 671–677.
183. Y. Li, X. Duan, Z. Liu, C. Li, F. Ye, Z. Zhang, L. Chen, C. Du, Q. Wang and B. Shan, Catalysis Science & Technology, 2024, 14, 6286–6297.
184. H. Wang, Q. Wang, J. Zhao, C. Liu, J. Feng, J. Jin and D. Liu, Mol. Catal., 2025, 584, 115296.
185. G. Grzybek, J. Gryboś, P. Indyka, J. Janas, K. Ciura, B. Leszczyński, F. Zasada, A. Kotarba and Z. Sojka, Appl. Catal., B, 2021, 297, 120435.
186. C. Zhang, Z. Zhang, C. Sui, F. Yuan, X. Niu and Y. Zhu, ChemCatChem, 2016, 8, 2155–2164.
187. H. Yu, X. Wang and X. Wu, Mol. Catal., 2018, 460, 69–73.

Author ORCID ID #s:

| | |
|--------------------|---|
| Han Chau | https://orcid.org/0000-0003-3172-0257 |
| Sarah Stofik | https://orcid.org/0009-0001-5693-8271 |
| Matthew N. Gordon | https://orcid.org/0000-0001-7212-9047 |
| Mark Mueller | https://orcid.org/0009-0008-0977-7517 |
| Rebecca Fushimi | https://orcid.org/0000-0002-7570-0234 |
| Dilpuneet S. Aidhy | https://orcid.org/0000-0002-5254-3862 |
| Matthew Craps | https://orcid.org/0000-0001-5469-8262 |
| Jochen Lauterbach | https://orcid.org/0000-0001-8303-7703 |
| Dylan D. Rodene | https://orcid.org/0000-0002-5235-4260 |

View Article Online
DOI: 10.1039/D5CY01360G



- No primary research results, software or code have been included and no new data were generated or analysed as part of this review.

